NEW MATERIALS FOR INTERMEDIATE-TEMPERATURE SOLID OXIDE FUEL CELLS TO BE POWERED BY CARBON- AND SULFUR-CONTAINING FUELS

A Dissertation
Presented to
The Academic Faculty

by

Lei Yang

In Partial Fulfillment
of the Requirements for the Degree
Doctor of Philosophy in the
School of Materials Science and Engineering

Georgia Institute of Technology

May, 2011

NEW MATERIALS FOR INTERMEDIATE-TEMPERATURE SOLID OXIDE FUEL CELLS TO BE POWERED BY CARBON- AND SULFUR-CONTAINING FUELS

Approved by:

Dr. Meilin Liu, Advisor
School of Materials Science and Engineering
Georgia Institute of Technology

Dr. Z.L. Wang
School of Materials Science and Engineering
Georgia Institute of Technology

Dr. Lawrence A. Bottomley
School of Chemistry and Biochemistry
Georgia Institute of Technology

Dr. C.P. Wong
School of Materials Science and Engineering
Georgia Institute of Technology

Dr. Preet M. Singh
School of Materials Science and Engineering
Georgia Institute of Technology

Date Approved: [March, 2011]

ACKNOWLEDGEMENTS

My sincerest thanks go to my supervisor, Dr. Meilin Liu who has offered his intelligence and vast knowledge while providing enthusiasm, insight and creativity. Without his commitment this thesis would not have had the present quality and consistency.

I would like to convey my appreciation to my thesis committee, Dr. Larry Bottomley, Dr. Preet M. Singh. Dr. Z.L. Wang, Dr. C.P. Wong, for their direction and invaluable advice along this project. I am truly grateful to Dr. C.P. Wong and Dr. Robert Snyder for their constant inspiration and help given to me during the course of my doctoral study.

Special thanks are extended to all collaborators for their active assistance and valuable contributions to my work. In Brook National Laboratory, thanks to Dr. Ping Liu, Dr. Yong-Man Choi. In New Jersey Institute of Technology, thanks to Dr. Trevor A. Tyson and Dr. Haiyan Chen. In Oak Ridge National Laboratory, thanks to Dr. Karren More and Dr. Jianming Bai. In National Energy Technology Laboratory, thanks to Dr. Briggs White and Dr. Wayne Surdoval. In Pacific Northwest National Laboratory, thanks to Dr. Larry Pederson. I am much indebted to all my colleagues of the Liu group for their help, the fruitful discussions and the great ambience.

Words fail me to express my appreciation to my wife Shuang whose dedication, love and persistent confidence in me, has taken the load off my shoulder. I also owe my loving thanks to my son Vincent for the joyful moments during the hard work on this study. Finally, I express my deep gratitude to my parents and my parents-in-law, who have given their endless support throughout my life and education.

Financial support from DOE Energy Frontier Research Center (HeteroFoaM, DE-SC0001061), DOE Catalysis Science Program (DE-FG02-06ER15837) and DOE Solid State Energy Conversion Alliance (DE-FC26-04NT42219) is greatly acknowledged.

TABLE OF CONTENTS

LIST OF TABLES

LIST OF FIGURES

SUMMARY

Unlike polymer electrolyte fuel cells, solid-oxide fuel cells (SOFCs) have the potential to use a wide variety of fuels, including hydrocarbons and gasified coal or different types of ample carbonaceous solids. However, the conventional anode for an SOFC, a composite consisting of nickel and yttria-stabilized-zirconia (YSZ), is highly susceptible to carbon buildup (coking) and deactivation (poisoning) by contaminants commonly encountered in readily available fuels. Further, the low ionic conductivity of the electrolyte and the poor performance of the cathode at lower temperatures require SOFCs to operate at high temperatures (>800 ^{o}C), thereby increasing costs and reduce system operation life. Thus, in order to make SOFCs fully fuel-flexible, cost-effective power systems, the issues of anode tolerance to coking and sulfur poisoning as well as the slow ionic conduction in the electrolyte and the sluggish kinetics at the cathode need to be addressed.

In this thesis, a novel electrolyte was shown to have the highest ionic conductivity below 750^{o}C of all known electrolyte materials for SOFCs applications, which allowed for fabrication of a thin-electrolyte cell with high power output at lower temperatures. The detailed electrochemical analyses of BZCYYb conductor revealed that the conductivities were sensitive to doping and partial pressure of oxygen, hydrogen, and water. When used in combination with Ni as a composite anode (Ni-BZCYYb), it was shown to provide excellent tolerance to coking and sulfur poisoning. Extensive investigations on surfaces of BZCYYb and Ni by Raman Spectroscopy and Scanning Auger Nanoprobe disclosed that its unique ability appears linked to the mixed conductor's enhanced catalytic activity for sulfur oxidation and hydrocarbon cracking/reforming, as well as enhanced multilayer water adsorption capability. In addition, the nanostructured oxide layers on Ni from dispersion of BZCYYb traces during high-temperature calcinations may effectively suppress the formation of carbon from dehydrogenation.

Based on the fundamental understanding on surface properties, a new and simple modification strategy was developed to hinder the carbon-induced deactivation of the state-of-the-art Ni-YSZ anode. Compared to the complex Ni-BZCYYb anode, this modified Ni-YSZ anode could be readily adopted in the latest fuel cell systems based on YSZ electrolyte. The much-improved power output and tolerance to coking of the modified Ni-YSZ anode were attributed to the nanostructured BaO/Ni interfaces observed by synchrotron-based X-ray and advanced electron microscopy, which readily adsorbed water and facilitated water-mediated carbon removal reactions. Density functional theory (DFT) calculations predicted that the dissociated OH from H_2O on BaO reacted with C on Ni near the BaO/Ni interface to produce CO and H species, which were then electrochemically oxidized at the triple-phase boundaries of the anode. Also, some new insights into the sulfur poisoning behavior of the Ni-YSZ anode have been revealed. The so-called "second-stage poisoning" commonly reported in the literatures can be avoided by using a new sealant, indicating that this poisoning is unlikely the inherent electrochemical behavior of a Ni-YSZ anode but associated with other complications.

Furthermore, a new composite cathode with simultaneous transport of proton, oxygen vacancies and electronic defects was developed for low-temperature SOFCs based on oxide proton conductors. Compared to the conventional oxygen ion-electron conducting cathode, this cathode is very active for oxygen reduction, extending the electrochemically active sites and significantly reducing the cathodic polarization resistance.

Towards the end, these findings have great potential to dramatically improve the economical competitiveness and commercial viability of SOFCs that are driven by cost-effective and renewable fuels.

CHAPTER 1

INTRODUCTION

1.1 Motivation statement

Growing the clean alternative energy industry is key to improving the quality of life for individuals and communities[1]. Fossil fuels are not a renewable energy source however advanced and developing countries rely heavily on energy produced from these fuels. The ever-increasing demand and dwindling supply of fossil fuels will inevitably cause problems for all countries in the future. In remote areas of developing countries, transmission and distribution of fossil fuel-generated energy can be difficult and expensive. Additionally, air pollution is an environmental problem which is caused by the use of fossil fuels, and results in the formation of smog.

The critical technical barrier to the widespread application of various alternative energy technologies is the undesirable properties of the key materials. For example, in solar-fuel production, the efficiency is relatively low since the current photocathode materials show sluggish H_2 evolution reaction kinetics and the photoanode materials have insufficient light absorption and carrier collection capabilities[2]. In wind power, the lifetime of turbine blade currently made of polymer-matrix composite materials reinforced with fiberglass or graphite fibers can be further enhanced when a new material with adequate stiffness to prevent failure as well as sufficient long term fatigue in harsh conditions is developed[3]. Therefore, materials science and technology plays a pivotal role in building the world's energy future, from fundamental discovery science, to improving energy production processes. The discovery and optimization of the materials could effectively advance solutions to energy challenges.

The demand for clean, secure, and renewable energy has stimulated great interest in fuel cells. A fuel cell is an electrochemical cell that converts energy from a fuel into electrical energy. Among all types of fuel cells, solid oxide fuel cells (SOFCs) offer great

promise for the most efficient and cost-effective utilization of a wide variety of fuels such as hydrocarbons, coal gas and gasified biomass[4]. The major hurdle to fuel flexibility is the vulnerability of the state-of-the-art Ni-YSZ (yttria-stabilized-zirconia) anode materials to coking and sulfur poisoning[5]. In addition, the high operating temperatures of SOFCs, stemming from the low ionic conductivity of the electrolyte materials[6] and the poor performance of the cathode materials at lower temperatures[7], increase costs and reduce the system operation life. Thus, in order to make SOFCs fully fuel-flexible and cost-effective power systems, the issues of anode tolerance to coking and sulfur poisoning, slow ionic conduction in the electrolyte and sluggish kinetics at the cathode need to be addressed. In a broader scientific context, the chemical and electrochemical mechanisms that lead to both of these issues and the phenomena that could prevent them should be investigated in order to best optimize the materials and microstructure of SOFCs for excellent performance and stability.

1.2 Research objectives

The main objective of the research is to develop novel electrolyte and electrodes with high electrical conductivity and electrocatalytic activity at low temperatures and to gain fundamental understanding of the interrelationships between lattice structure, local atomic environment, bulk transport, surface property and electrocatalytic activity. It is anticipated that this work would enrich our knowledge of conducting rational design of high-performance electrolyte and electrode, as well as greatly improve the economical competitiveness and fuel flexibility of SOFCs that are driven by cost-effective and renewable fuels through accomplishing the following specific aims.

- To discover new electrolytes with high ionic conductivity and minimal electron transport, with the goal of creating an electrolyte material that can be fabricated economically into thin-film form for SOFCs to be operated at intermediate temperatures (600-800 ^{o}C).

- To explore new anode materials that have high tolerance to sulfur poisoning and carbon buildup and could directly utilize sulfur-containing carbonaceous fuels.
- To develop novel cathodes with remarkable oxygen reduction reaction activity as well as good chemical, physical and electrochemical compatibilities with the electrolyte.
- To establish the structure-property relationship in developed electrolyte material system and to acquire a profound knowledge of anodic and cathodic reactions on surface and interface.

1.3 Thesis structure

Chapter 2 provides a broad overview of the most recent progresses on development of electrolyte, anode and cathode materials in Solid Oxide Fuel Cells, with a particular focus on proton conducting SOFCs. The critical issues of the latest electrolytes and electrodes are also discussed.

Chapter 3 demonstrates a new electrolyte with extensive investigation of conductivity in various atmospheres. Synchrotron-based X-ray diffraction and adsorption spectroscopy are employed to establish the structure-property relationships. Furthermore, the mole ratio of Zr to Ce is tailored in order to obtain sufficient chemical stability without sacrificing the electrical conductivity.

Chapter 4 presents a new anode with remarkable sulfur and coking tolerance. The mechanism responsible for the enhanced electrocatalytic activity is unraveled by analyzing the surfaces of BZCYYb and Ni in cermet anode using Scanning Auger Nanoprobe, X-ray Photoelectron Spectroscopy and Raman spectroscopy.

Chapter 5 shows a simple, cheap modification of state-of-the-art Ni-YSZ anode with goal of achieving direct use of hydrocarbons, CO and gasified carbon fuels. Synchrotron-enabled X-ray analysis, advanced electron microscopy and spectroscopy,

Thermal gravimetric analysis, and Raman spectroscopy have been used to characterize the composition, structure, and morphology of the anode surfaces and their electro-catalytic properties under fuel cell operating conditions. Density functional theory (DFT) calculations predict the elementary steps occurring on the oxide/metal interfaces.

Chapter 6 reveals new insights into sulfur poisoning behavior from long-term (~3,000 hours) operation of the-state-of-the-art, high-performance, anode-supported SOFCs. The performance characteristics are extensively examined under various fuel cell operating conditions.

Chapter 7 discloses a new composite cathode with simultaneous transport of proton, oxygen ion and electronic defects for proton conducting SOFCs. The durability of the composite cathode is also evaluated from both gavalostaic discharge and cyclic voltage sweeps.

Chapter 8 gives conclusions for this research and provides insight into future directions in this field.

CHAPTER 2

BACKGROUND

2.1 Development status of electrolyte

Solid oxide fuel cells (SOFCs) have a great potential to be the power of the future because of low emission, high energy efficiency, and excellent fuel flexibility[4]. However, the cost must be reduced substantially for successful commercialization of SOFC technologies. The primary solution is to lower the operating temperature of SOFCs from the traditional 1000 ^{o}C to 600–800^{o}C[8]. Unfortunately, the overall electrochemical performance of the state-of-the-art SOFC system will decrease with a reduced operating temperature due to the decreased electrolyte conductivity. Thus, it is of paramount importance to develop a highly conducting electrolyte for low temperature SOFCs. To date, doped ceria is one of the most promising electrolyte materials, which has a potential to meet the requirements for fuel cell operation below 600 ^{o}C. However, critical issues still remain such as electronic conduction and insufficient mechanical integrity under fuel cell operating conditions. The discovery of a new electrolyte for low-temperature SOFCs represents a grand challenge to the SOFC community.

Doped cerate has been the subject of extensive investigation ever since Iwahara et al. [9]demonstrated the utility of such materials in hydrogen sensors and other solid ionic devices. It has very high ionic conductivity stemming from the low activation energy for proton transport. Cerate compounds when doped, typically on the B-site by a lower-valent cation, become oxygen-deficient. The dopant dissolution mechanism leads to the creation of oxygen vacancies as per Equation 2-1 (written in Kroger-Vink notation).

$$2Ce_{Ce}^{X} + O_{O}^{X} + Y_2O_3 \Leftrightarrow 2Y_{Ce}^{/} + V_{O}^{\bullet\bullet} + 2CeO_2 \quad (2\text{-}1)$$

Subsequent exposure to humid atmospheres is presumed to lead to the incorporation of protons into the lattice according to Equation 2-2.

$$H_2O(g) + V_{O}^{\bullet\bullet} + O_{O}^{X} \Leftrightarrow 2OH_{O}^{\bullet} \quad (2\text{-}2)$$

High proton conductivity has been reported for many perovskite-type oxides upon exposure in a humidified atmosphere, such as $BaZrO_3$, $SrZrO_3$, $SrCeO_3$, and $BaCeO_3$, when doped with aliovalent element in B site. Kreuer [10] proposed an idea of chemical matching in barium cerate system, i.e. the dopant which provides the least effect on basicity of adjacent oxygen best chemically matches; both the ionic radius and electronegativity of the dopant will determine the chemical matching. Based on this criterion, Gd was suggested as a optimum dopant for $BaCeO_3$ [11]. In fact, $BaCe_{0.8}Gd_{0.2}O_{3-\delta}$ has been widely studied in SOFCs because of its high conductivity in O_2-containing atmospheres and under fuel cell conditions[12]. It was recently reported that the ionic radii of the dopants had a trade-off effect on the electrical conductivity and chemical stability of the doped cerate[13]. Among the dopants of Y, Tm, Yb, Lu, In and Sc, Y doped barium cerate exhibited the highest conductivity. The conductivity increases with increasing ionic radius and decreasing electro-negativity (increasing basicity). Such a dependence of the ionic conductivity on the dopant size is also observed in the $BaZrO_3$ system[14].

The combination of high proton conductivity and good chemical stability, which is a prerequisite for the application in SOFCs, is considered to be a primary issue for the development of proton conductors. Generally, doped cerate exhibits a high conductivity but it has poor chemical stability in H_2O or CO_2 containing atmospheres. On the other hand, zirconate based materials show superior chemical and thermal stability but is has low conductivity. Since $BaCeO_3$ and $BaZrO_3$ easily form solid solutions, it is possible to replace a fraction of Ce in $BaCeO_3$ with Zr[15, 16]. This type of solid solution is expected to exhibit both high proton conductivity and excellent chemical and mechanical stability, as well as high ionic transference number over a wide range of conditions. A composition $BaCe_{0.7}Zr_{0.2}Nd_{0.1}O_{3-\delta}$ was reported by Haile et al[17], which appeared to give a good compromise between conductivity and stability for fuel cell applications. Zuo et al [18] developed a new composition $Ba(Zr_{0.1}Ce_{0.7}Y_{0.2})\ O_{3-\delta}$ (BZCY7), in the barium–

zirconium–cerium–yttrium family. At temperatures below 550°C, it displayed the highest ionic conductivity of all known electrolyte materials for SOFC applications ($9x10^{-3}$S/cm in H_2 containing 3% H_2O at 773 K, figure 2-1). Moreover, XRD examination of BZCY7 powder samples indicates that it is stable at 500°C in an atmosphere containing 2% CO_2 and 15% H_2O vapor.

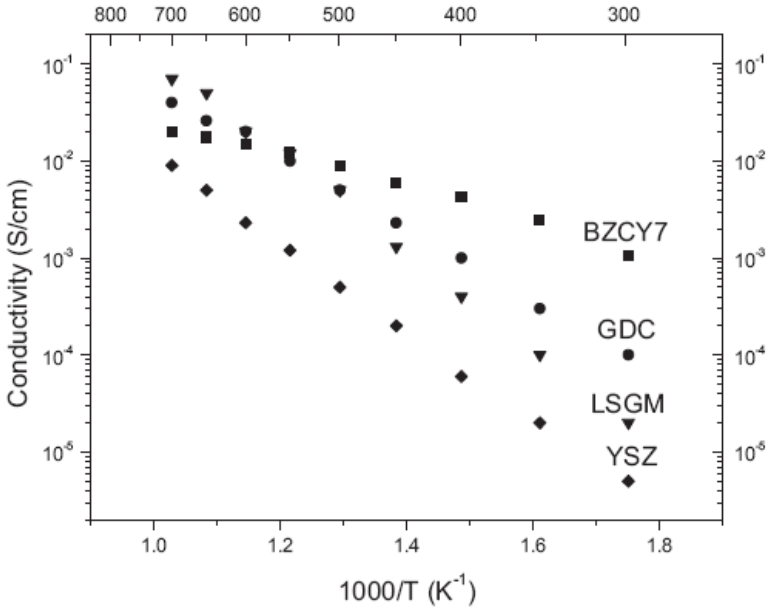

Figure 2-1 Comparison of the ionic conductivities of BZCY7, GDC, LSGM, and YSZ in a humid 4% H_2/Ar atmosphere at 300–700 °C (the temperature scale is given by the upper *x*-axis).

However, $Ba(Zr_{0.1}Ce_{0.7}Y_{0.2})O_{3-\delta}$ material is not stable in pure CO_2, which is very critical when high fuel utilization rate occurs in fuel cell stacks. To obtain the high chemical stability without greatly sacrificing the electrical conductivity in the BZC system, it is necessary to tailor the Zr/Ce ratio. Fabbri[19] synthesized $BaCe_{0.8-x}Zr_xY_{0.2}O_{3-\delta}$ (BCZY, with $0.0 \leqslant x \leqslant 0.8$) by a sol-gel process. It was found that the introduction of Zr into barium cerate resulted in a reduction of the conductivity at all the operating temperatures. For example, at 700 ^oC the conductivity values were measured at

1.47*10^{-2}S/cm for the compound with x=0, decreasing up to 5.68*10^{-3}S/cm for x=0.8 (figure 1-2). The reduction in conductivity was attributed to the larger grain boundary surface with increasing Zr content. However, Zr addition can definitely improve the chemical stability of $BaCe_{0.8-x}Zr_xY_{0.2}O_{3-\delta}$ compounds. An optimal composition of $BaZr_{0.5}Ce_{0.3}Y_{0.2}O_{3-\delta}$ was shown to maintain the good chemical stability of barium zirconate but with improved electrical conductivity and fuel cell performance.

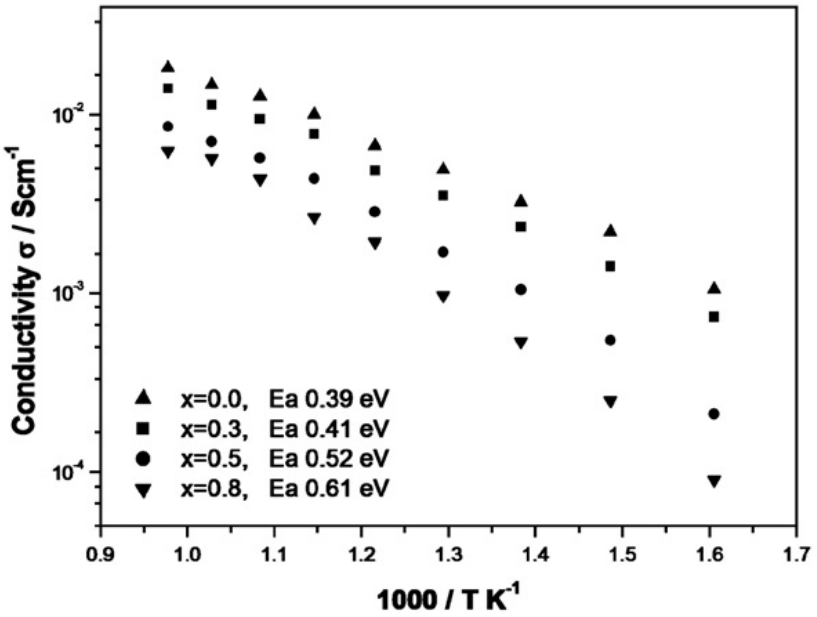

Figure 2-2 Total electrical conductivity in wet H_2 as a function of temperature for different oxide compositions.

2.2 Development status of anode

Unlike polymer electrolyte fuel cells, solid-oxide fuel cells (SOFCs) can use a wide variety hydrocarbon fuels [4]. Because of their high operating temperatures (600 to 800 ºC), metal catalysts added to the ceramic anodes can facilitate reforming reactions that generate H_2 and CO from hydrocarbons. The conventional anode for an SOFC, a composite consisting of nickel and yttria-stabilized-zirconia (YSZ), has excellent catalytic activity for fuel oxidation, good conductivity for current collection, and unmatched compatibility with YSZ electrolyte for easy cell fabrication, but it is highly

susceptible to carbon buildup (coking) and deactivation (poisoning) by contaminants commonly encountered in readily available fuels [5]. Some contaminants (e.g., sulfur impurities) can dramatically degrade its performance even at parts per million (ppm) levels [20]. Sulfur adsorbs strongly on Ni surface and thus blocks the active sites for electrochemical oxidation of fuel, resulting in considerably increased anodic polarization and energy loss.

To overcome these problems, significant efforts have been devoted to the development of new anode materials and novel electrode structures [21-28]. For example, the use of a ceria-based anodes demonstrate the potential for direct utilization of methane in an SOFC [21]. Later, the use of a composite anode consisting of copper and ceria led to successful operation of an SOFC with higher hydrocarbons than methane, which are more prone to coking due to higher content of carbon [22]. Figure 2-3 shows the performance of the cell with Cu-CeO_2 anode when supplied with H_2 or n-butane at 973 or 1073 K. Stable peak power densities of cells in H_2 and n-butane were 0.31 W/cm2 and 0.18/cm^2 at 1073 K, respectively.

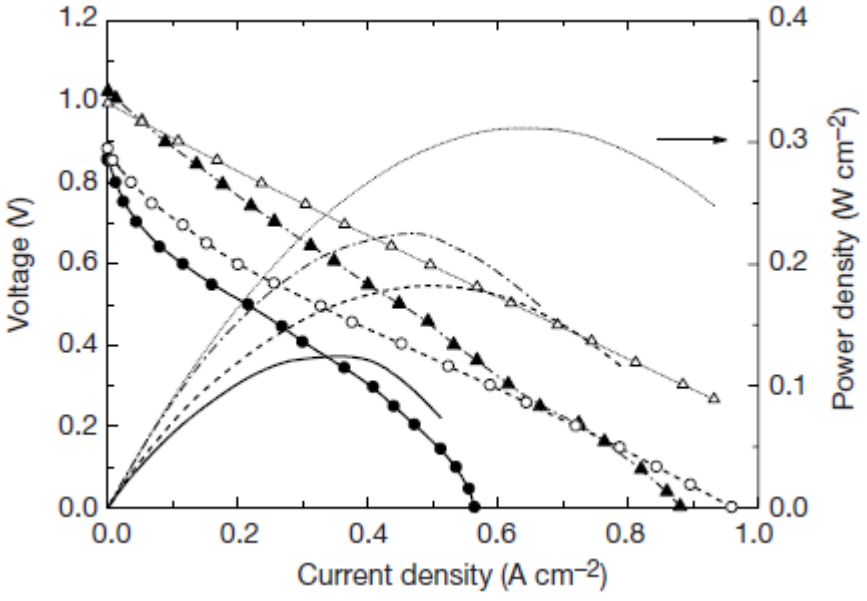

Figure 2-3 Power densities and current density–voltage relationships for an SOFC using the Cu-ceria composite anode. The cell had a 60-mm electrolyte, and data are shown for

the following fuels: filled circles, n-butane at 973 K; open circles, n-butane at 1,073 K; filled triangles, H_2 at 973 K; and open triangles, H_2 at 1,073 K.

More interestingly, it was found that the amount of CO_2 produced in the effluent gas were consistent with the data calculated assuming complete oxidation of methane and n-butane to CO_2 and water according to the reactions (Figure 2-4). The agreement suggests that complete oxidation of fuels is the primary reaction in the anode compartment.

$$CH_4 + 4O^{2-} \rightarrow CO_2 + 2H_2O + 8e^-$$

$$C_4H_{10} + 13O^{2-} \rightarrow 4CO_2 + 5H_2O + 26e^-$$

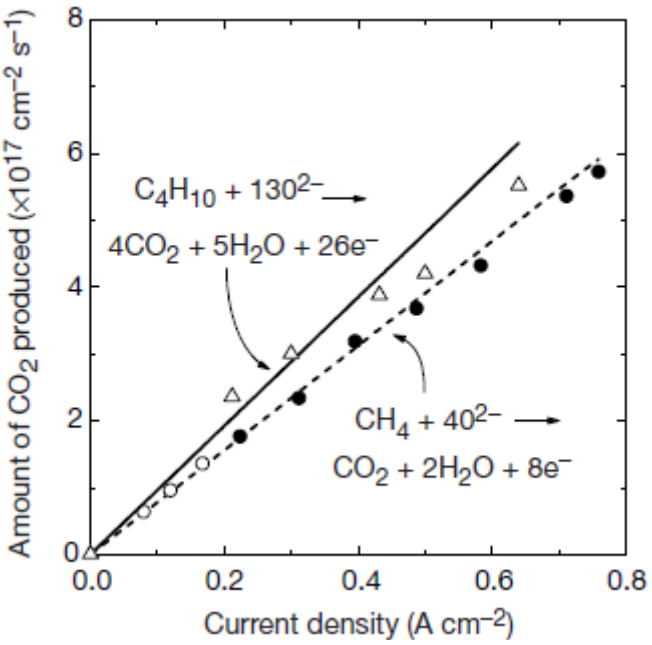

Figure 2-4 CO_2 production for methane and n-butane as a function of current density using the Cu-ceria composite anode. The data were obtained by gas analysis for: n-butane at 973 K (open triangles), methane at 973 K (open circles), and methane at 1,073 K (filled circles). The lines were calculated from the current density, assuming complete oxidation.

However, some practical issues still remain: The low melting point of Cu makes it difficult to fabricate anode-supported cells using conventional co-firing ceramic methods and the poor catalytic activity of Cu for fuel oxidation limits cell power output.

In another approach, a catalyst layer (e.g., Ru-ceria) was applied to a conventional Ni-YSZ anode to allow internal reforming of hydrocarbons. The effectiveness of this cell structure was confirmed for direct use of iso-octane without coking in an SOFC with power densities of 0.3 to 0.6 W cm^{-2} at 670 to 770ºC [24]. Figure 2-5 shows the comparison of the cell voltages as a function of time in mixed air-CO_2-octane fuels. It was found that stable operation can be achieved through two modifications including Ru-CeO_2 catalyst layers and pre-reforming/oxidation of the octane fuels. However, the introduction of these oxidizing agents in the fuel definitely decreases the system efficiency and may raise the safety concerns. In addition, this cell design has several critical drawbacks such as decreased power density, difficulty in current collection, and the high cost of Ru.

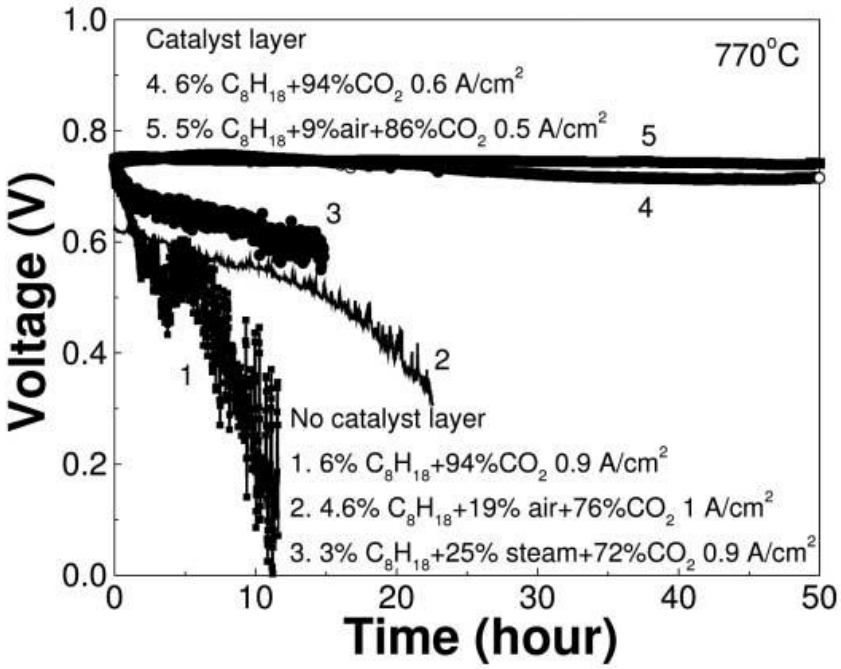

Figure 2-5 Life tests of anode-supported SOFCs (Ni-YSZ|YSZ|LSM-YSZ, LSM) operated on various iso-octane/CO_2/steam/air mixtures with or without a catalyst layer at 770^{o}C.

Nickel-free conducting metal oxides have also been developed as anode materials, including $La_{0.75}Sr_{0.25}Cr_{0.5}Mn_{0.5}O_{3-\delta}$ [23], $Sr_2Mg_{1-x}Mn_xMoO_{6-\delta}$ (x = 0-1) [26], and doped (La,Sr)(Ti)O_3 [25, 28]. These anode materials showed different degrees of improved tolerance to coking, re-oxidation, and/or sulfur poisoning under various SOFC operating conditions. Goodenough and co-works discovered a double pervosckite $Sr_2Mg_{1-x}Mn_xMoO_{6-\delta}$ (x = 0-1) with high electrical conductivity and electrocatalytic activity. It was shown that the cell with $Sr_2MgMoO_{6-\delta}$ anode was stable in methane or 5ppm H_2S/H_2 fuels at 800 ^{o}C, indicating a good potential to be used in direct hydrocarbon fuel cells (Figure 2-6).

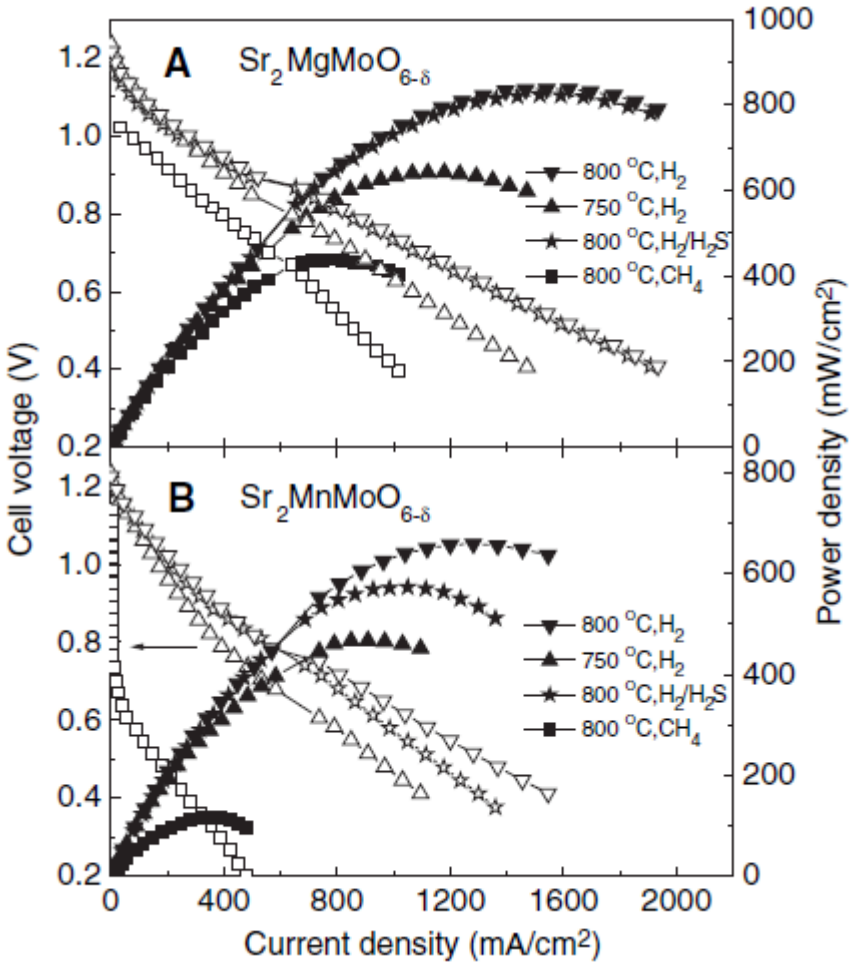

Figure 2-6 Cell voltage and power density as a function of current density for the single fuel cells with anodes of (A) Sr_2MgMoO_{6-d} and (B) Sr_2MnMoO_{6-d} in H_2, H_2/H_2S, and CH_4 fuels. Cell voltages are represented by open symbols, and power densities by closed symbols.

In many cases, however, the power densities of the SOFCs using Ni-free oxide anodes are less than those demonstrated by conventional Ni-YSZ supported SOFCs with thin electrolytes. It has been difficult for the alternative anode materials to be adopted in the state-of-the-art fuel cell systems based on YSZ electrolyte, which have evolved progressively in the past few decades. The difficulties originate largely from alternative anodes' limited physical, chemical, and thermal compatibility with YSZ electrolyte

during fabrication at high temperatures. Furthermore, buffer layers are commonly required between anode and electrolyte because of their limited physical, chemical, and thermal compatibility with YSZ electrolyte during fabrication and operation at high temperatures, thereby increasing the system complexity and cost. For example, $La_{0.4}Ce_{0.6}O_{2-\delta}$ and $Ce_{0.8}Gd_{0.2}O_{2-\delta}$ interlayers were used for SMMO and LSCM anodes, respectively. Moreover, in some cases, inadequate lateral conductivity (or substantial sheet resistance) of oxide anodes contributes to low power density, especially for SOFC designs with long current collection paths as in fuel cell stacks. To alleviate these problems, some types of metal (usually Pt) are usually necessary as current collectors that caused uncertainties of investigating the intrinsic catalytic activity of the oxide anodes. In some cases, inadequate lateral conductivity (or substantial sheet resistance) of Ni-free oxide anodes also contributes to low power density, especially for SOFC designs with long current collection paths as in fuel cell stacks.

To overcome these problems, conducting oxides (e.g., $Sr_{0.8}La_{0.2}TiO_3$) have been used as anode-side supports together with an interlayer (e.g., a ceramic-metal composite, or cermet, of Ni and doped ceria) to allow fabrication of an anode-supported thin-electrolyte SOFC via conventional ceramic processing methods [29]. This cell design leads to high power densities, much-improved stability against coking in natural gas, and enhanced tolerance to H_2S poisoning. However, the modified cell experienced similar initial voltage drop to that for blank cell but indeed prevented the long-term degradation in 100 ppm H_2S/H_2. In contrast, there was an additional continuous decrease over 70 h for a Ni-YSZ cell (Figure 2-7). The similar initial degradation represents that the SLT anode support does not eliminate the sulfur adsorption on Ni and can not remove the sulfur in the fuel as an outer catalyst. Furthermore, the subsequent slow degradation in performance might be not associated with the intrinsic properties of Ni-YSZ. It is thus likely that the SLT support prevents the adverse reactions between sealant and Ni-YSZ anode under sulfur-containing fuels instead of affecting the sulfur-anode interactions.

Towards the end, alternative anode materials and innovative anode structures have improved the tolerance to coking and poisoning by contaminants. To date, however, an initial drop of substantial magnitude in power output upon exposure to H_2S-contaminated fuels still appears unavoidable for any known anode materials.

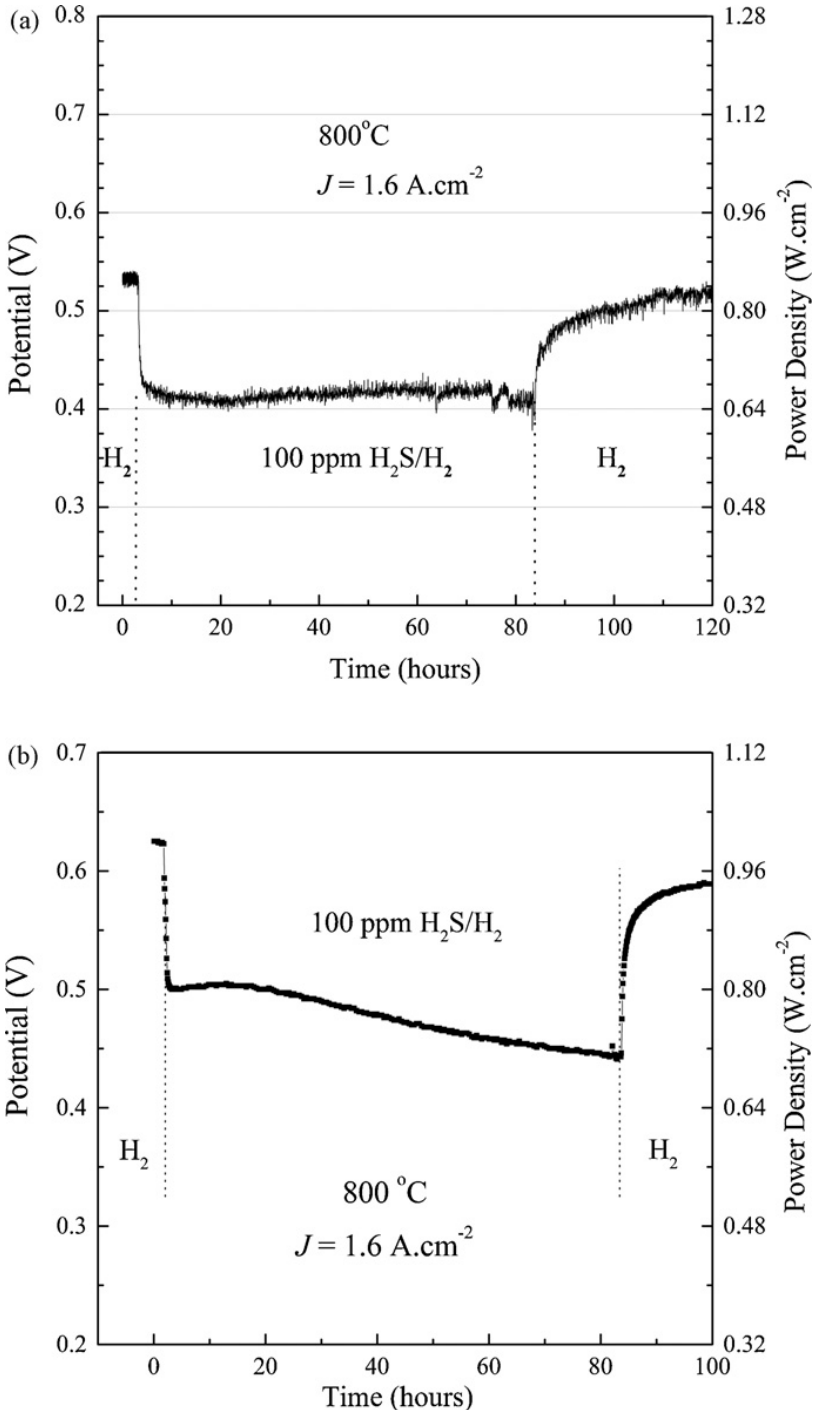

Figure 2-7 Voltage versus time for (a) SLT-supported and (b) Ni–YSZ-supported SOFCs tested at 1.6Acm^{-2} and 800 ^{o}C in dry H_2 and H_2 with 100ppm H_2S.

2.3 Development status of cathode

Cathode is the dominant factor influencing the power output at lower operating temperatures. However, the development of compatible cathodes based on oxide proton conductors is still in its infancy.[30] To date, only a few studies have been reported on oxide cathodes for proton conductors.[31] Conventional mixed ionic (oxygen ion)-electronic conducting cathodes have been used for oxide proton-conducting electrolytes, including $Sm_{0.5}Sr_{0.5}CoO_3$ (SSC), $Ba_{0.5}Pr_{0.5}CoO_3$ (BPC), $La_{0.5}Sr_{0.5}CoO_3$, $La_{0.6}Ba_{0.4}CoO_3$ (LBC) and $La_{0.7}Sr_{0.3}FeO_3$.[17] Yet, the electrode performances are inadequate for practical applications, due most likely to limited active sites for oxygen reduction at the interface between the proton-conducting electrolyte and the oxygen ion conducting cathodes. For example, $Sm_{0.5}Sr_{0.5}CoO_3$ (SSC) was used as the cathode for Y-doped barium cerate, yielding an overpotential of ~350 mV at a current density of 100 mA/cm^2 at 600 ^{o}C [32], far exceeding the overpotential of an SSC cathode on an SDC electrolyte, ~35 mV under the same conditions [33]. While layered perovskite $SmBaCo_2O_{5+x}$ is a superior cathode for cells based on oxygen ion conductors[34, 35], it showed relatively high cathodic polarization resistances when applied to BZCY electrolyte [36]. Hibino et al compared the overpotential of various electrodes measured at 600 ^{o}C including Au, Pt, SSC, LSC, LBC and BPC (Figure 2-8). It was found that Pt showed higher cathodic potential than the oxide cathodes. Among them, the BPC cathode exhibited an overpotential of ~50mV at 100 mA/cm^2 at 600 ^{o}C. However, it is still larger with respect to the optimal cathode for oxygen ion conducting electrolyte. To make better use of the new proton conductors such as BZCY, efficient cathode materials must be developed.

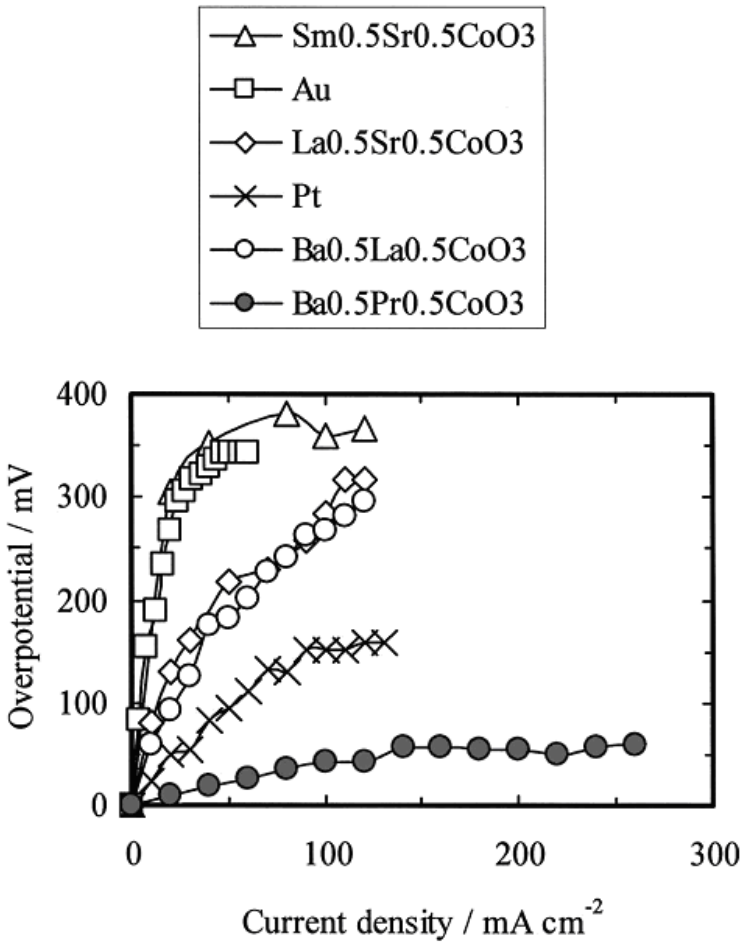

Figure 2-8 Polarization losses during discharge of SOFCs using BCY25 electrolyte with different cathodes at 600°C.

It has been reported that a composite cathode with mixed proton, oxygen ion, and electron conductivity could extend reaction zone beyond the electrolyte-electrode interface and hence reduce the charge transfer resistance [37-41]. Ideally, it is more desirable to dope transition metal ions into barium cerate phase to introduce these mixed conductivities, especially considering its superior compatibility with the electrolyte[42].

Recently, Bi-doped $BaCeO_3$ and Pr-doped $BaCe_{0.8}Y_{0.2}O_{3-\delta}$ and $BaCe_{0.8}Gd_{0.2}O_{3-\delta}$ were developed as cathodes for $Ba(Zr_{0.1}Ce_{0.7}Y_{0.2})O_{3-\delta}$ and $BaCe_{0.8}Gd_{0.2}O_{3-\delta}$ electrolytes, respectively [16, 43, 44]. All these mixed conducting cathodes exhibited relatively

sluggish reaction kinetics, for example, yielding a cathodic polarization resistance of 0.35 $\Omega \cdot cm^2$ at 800 ^oC for $Ba(Pr_{0.8}Gd_{0.2})O_{3-\delta}$. This is attributed primarily to the low electronic conductivity of these cathodes. Often, materials with high proton conductivity do not have sufficient electron conductivity to be useful as mixed protonic and electronic conductors (<0.1 S/cm at 800 ^oC)[45]. Shimura et al. [46]studied the effect of transition metal (Mn, Fe and Co) doping into $BaCe_{0.9}Y_{0.1}O_{3-\delta}$ proton conductors (Figure 2-9). Among the doped samples, Co-doped samples showed the highest conductivity and the lowest activation energy of conduction. However, no information about cathode performance was provided.

Electrochemical stability of cathode is another issue which impedes the development of SOFCs based on oxide proton conductors. Little information is available on the durability of cells based on the BZCY electrolyte. For an electrolyte with complicated components such as BZCY, it is difficult to develop a compatible cathode. It was found that a secondary phase $La_2Zr_2O_7$ was formed during processing at 1100^oC between $LaMnO_3$ (La_2NiO_4) and $BaZrO_3$[47]. Undesirable reactions between the components of a composite cathode may degrade the strength, electrical, catalytic, and electrochemical performance.

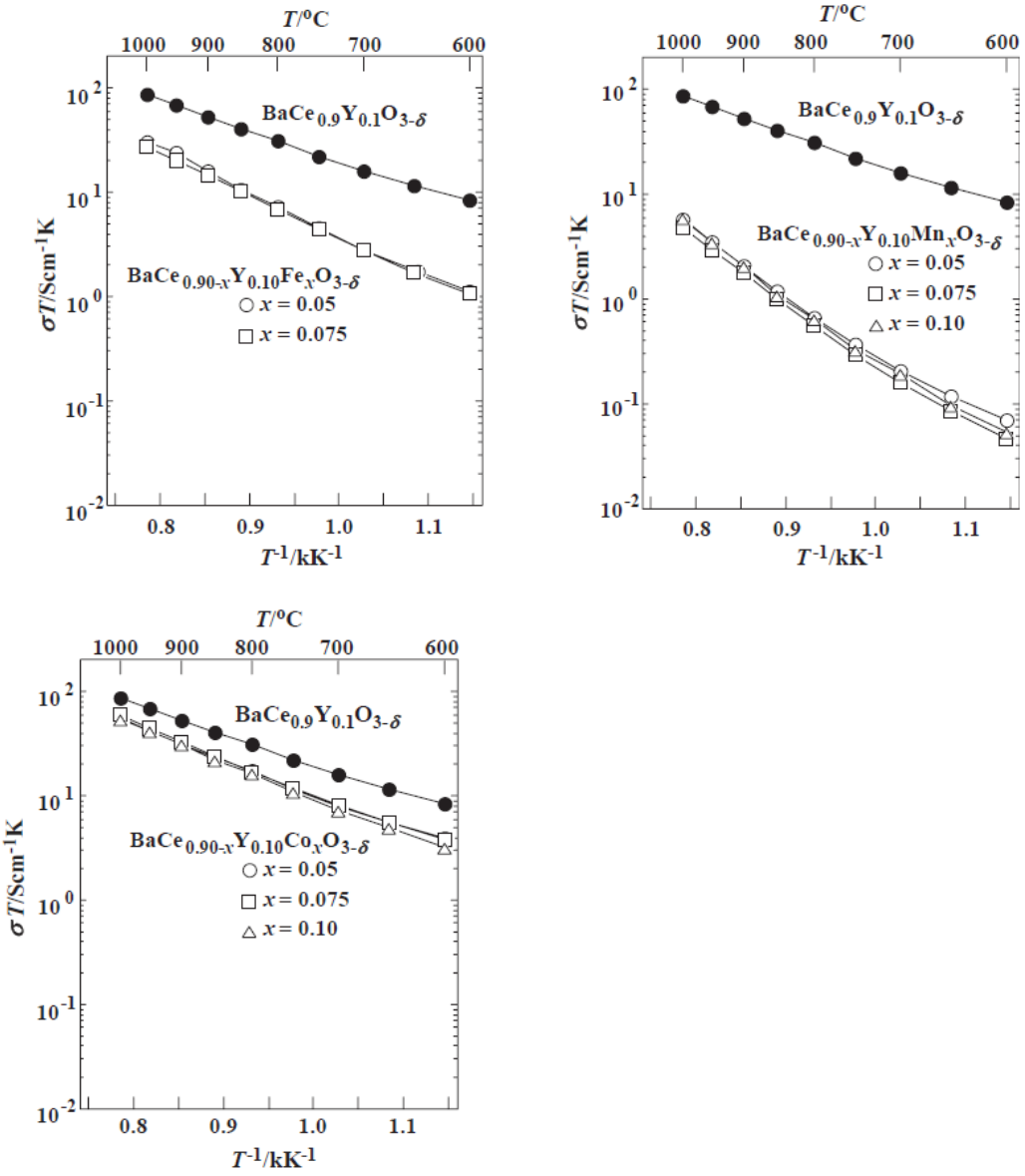

Figure 2-9 The conductivity of $BaCe_{0.90-x}Y_{0.10}Fe_xO_{3-\delta}$ (x =0, 0.05 and 0.075) in air. The conductivity of $BaCe_{0.90-x}Y_{0.10}Mn_xO_{3-\delta}$ (x =0, 0.05, 0.075 and 0.10) in air. The conductivity of $BaCe_{0.90-x}Y_{0.10}Co_xO_{3-\delta}$ (x =0, 0.05, 0.075 and 0.10) in air.

CHAPTER 3

A NEW ELECTROLYTE WITH HIGH ELECTRICAL CONDUCTIVITY

3.1 Experimental

The compositions of the materials were $BaZr_{0.1}Ce_{0.7}Y_{0.2-x}Yb_xO_{3-\delta}$ (x=0, 0.05, 0.1, 0.15, 0.2). All powders were synthesized by a conventional solid state reaction method. Stoichiometric amounts of high-purity barium carbonate, zirconium oxide, cerium oxide, ytterbium oxide, and yttrium oxide powders (all from Aldrich Chemicals) were mixed by ball milling in ethanol for 48 h, followed by drying in an oven and calcination at 1100 ^oC in air for 10 h. The calcined powder was ball milled again, followed by another calcination at 1100^oC in air for 10 h. For the conductivity measurement, the pre-calcined powders were then isostatically pressed into a disk at 274.6 MPa. The green disks had a diameter of 10 mm, with a typical thickness of 1 mm. The disks were then sintered at 1550 ^oC for 10 h in air (to achieve relative density > 96%).

For conductivity studies**,** platinum paste was applied to both sides of electrolyte disks and fired at 900^oC for 30 min to form porous platinum electrodes. Two platinum wires were attached to each of the electrodes. The electrical conductivities were studied in dry and wet oxygen, H_2, argon, and 4% H_2 (balanced with argon) at different temperatures. The wet gases were prepared by passing the corresponding gases though a water bubbler at 25ºC to bring in ~ 3 v% of water vapor.

3.2 Electrical conductivity of $BaZr_{0.1}Ce_{0.7}Y_{0.2-x}Yb_xO_{3-\delta}$

Doped zirconate-cerate compounds have been reported to exhibit both proton and oxide ion conductivity as well as a strong tendency for water absorption (or hydration) [10, 48-51]. For example, Y-doped zirconate-cerate, $Ba(Zr_{0.1}Ce_{0.7}Y_{0.2})O_{3-\delta}$ (BZCY), has high ionic conductivity and excellent chemical stability in atmospheres containing CO_2

and H_2O under SOFC operating conditions [16]. In this study, we have explored co-doping barium zirconate-cerate with Y and Yb using compositions of $BaZr_{0.1}Ce_{0.7}Y_{0.2-x}Yb_xO_{3-\delta}$ (x=0 to 0.2). We believe that the two dopants on the B-site function in a cooperative fashion to improve the ionic conductivity. Figure 3-1 shows XRD patterns of various Yb-doped $BaZr_{0.1}Ce_{0.7}Y_{0.2}O_{3-\delta}$. A pattern for a pure perovskite resembling that of $BaCeO_3$ can be observed. It is clear that Yb has replaced Y and has been doped into the lattice of $BaZr_{0.1}Ce_{0.7}Y_{0.2}O_{3-\delta}$ properly. Furthermore, XRD patterns of the materials did not change after conductivity measurements in dry and wet argon, oxygen, and hydrogen, suggesting that the samples are quite stable over a wide range of oxygen partial pressures.

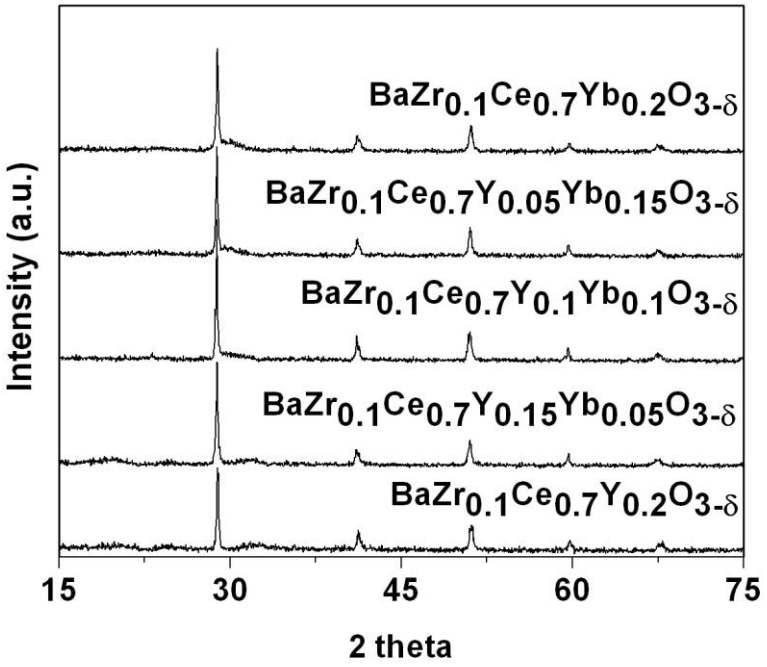

Figure 3-1 XRD patterns of $BaZr_{0.1}Ce_{0.7}Y_{0.2-x}Yb_xO_{3-\delta}$(x=0-0.2) powders.

When we compared the conductivities of BZCYYb with those of several other SOFC electrolyte materials, namely YSZ, GDC, and BZCY (Figure 3-2), $BaZr_{0.1}Ce_{0.7}Y_{0.1}Yb_{0.1}O_{3-\delta}$ displayed the highest conductivity below 750^{o}C. Operation of SOFCs at lower temperatures makes it possible to use much less expensive materials for

cell components, thus reducing the cost while prolonging the operational life. As expected, the conductivities are sensitive to doping and partial pressure of oxygen, hydrogen, and water.

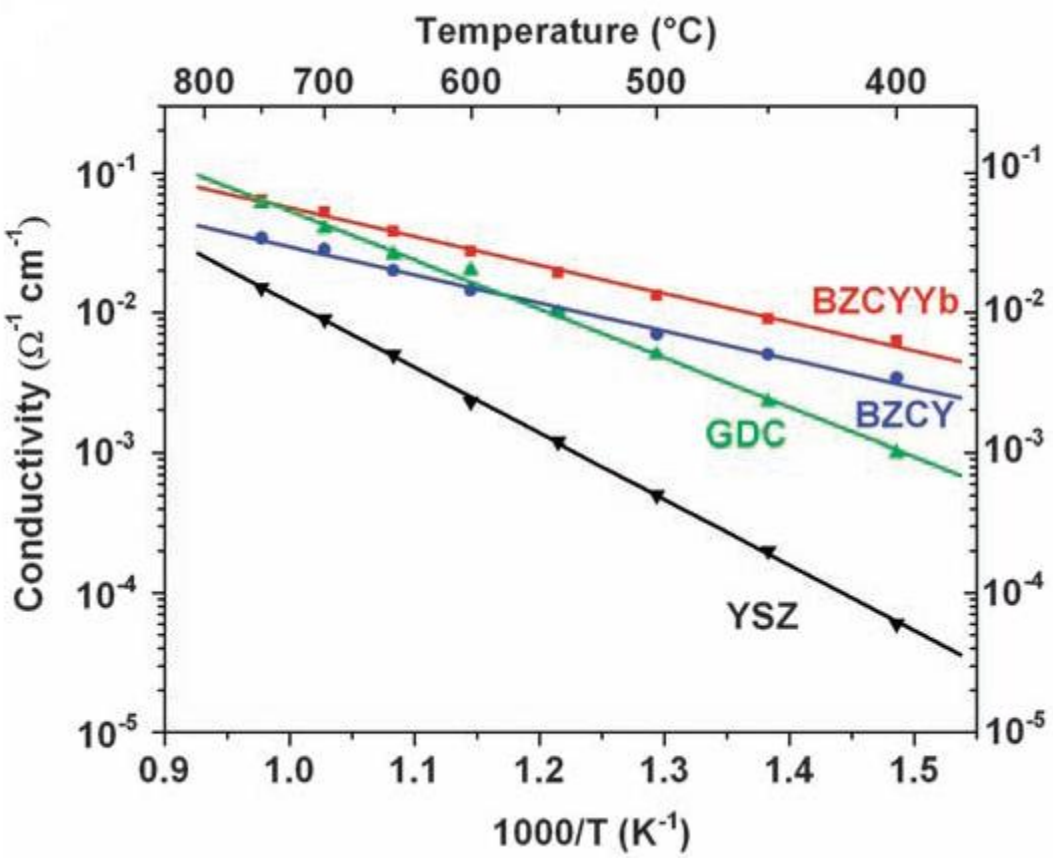

Figure3-2 Ionic conductivities of BZCYYb, BZCY, GDC, and YSZ as measured at 400° to 750°C in wet oxygen (with ~3 vol%H_2O).

Figure 3-3 shows the conductivities of $BaZr_{0.1}Ce_{0.7}Y_{0.2-x}Yb_xO_{3-\delta}$ (x=0-0.2) in dry and wet oxygen at different temperatures. The conductivities in dry oxygen are close to those in wet oxygen at high temperatures for all the samples studied. In this case, the dominant conductivity is electron hole and oxygen ion conductivity. The protonic defects generation process should be negligible. With the decrease in temperature, the conductivities in wet oxygen become higher than those in dry oxygen, which is due to the generation of protonic defects. The conductivities under various temperatures seem to

have the same Yb concentration dependency in both wet and dry oxygen. The conductivities increase quickly with increasing concentration of Yb, and reach the maximum at a Yb concentration about 10%. With the further increase in the concentration of Yb dopant, the conductivities decrease slightly. However, the conductivities in $BaZr_{0.1}Ce_{0.7}Yb_{0.2}O_{3-\delta}$ are still higher than those in $BaZr_{0.1}Ce_{0.7}Y_{0.2}O_{3-\delta}$. It is interesting to see that the barium cerate and zirconate solid solution containing multi-dopants has a higher conductivity than that containing single dopant, which could create a new method for the design of high conductivity proton conductors.

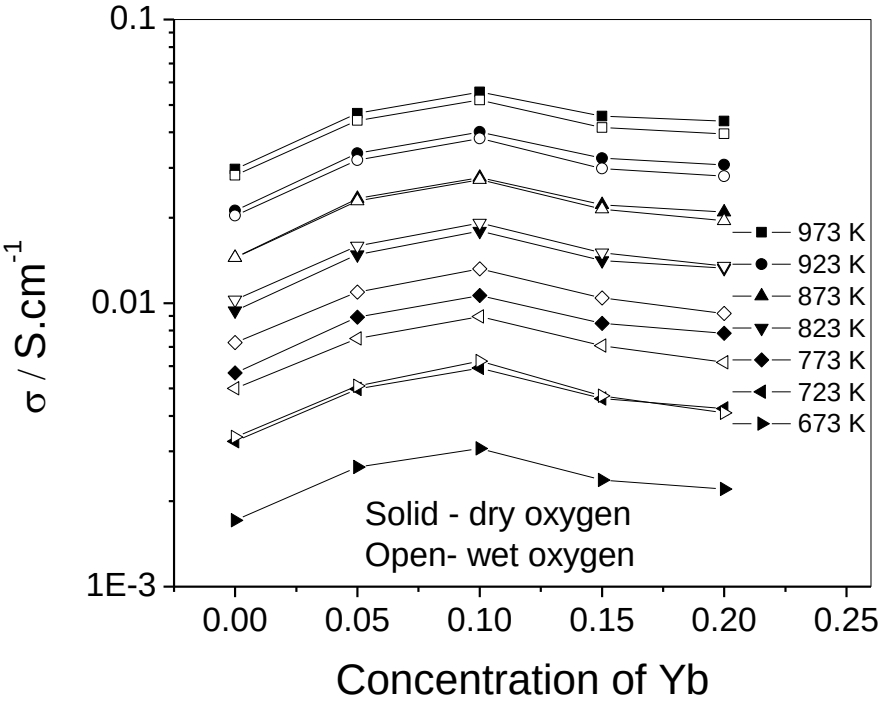

Figure 3-3 The conductivities of Yb doped $BaZr_{0.1}Ce_{0.7}Y_{0.2}O_{3-\delta}$ in dry and wet oxygen at various temperatures as a function of the concentration of Yb

The conductivities of $BaZr_{0.1}Ce_{0.7}Y_{0.2-x}Yb_xO_{3-\delta}$(x=0-0.2) in dry and wet argon are shown in Figures 3-4 and 3-5. In both cases, the conductivities increase quickly with increasing concentration of Yb, and reach the maximum at a Yb concentration about 10%. With the further increase in the concentration of Yb dopant, the conductivities decrease

slightly. $BaZr_{0.1}Ce_{0.7}Y_{0.1}Yb_{0.1}O_{3-\delta}$ exhibits a proton conductivity as high as 0.01 $S.cm^{-1}$ at around 773-723 K, suggesting that there is a great potential to develop proton conducting SOFCs working at around 673-773 K. This is the most promising type of proton conductors reported so far. A fuel cell operating in this temperature range offers the potential of long stability, quick start, and high efficiency.

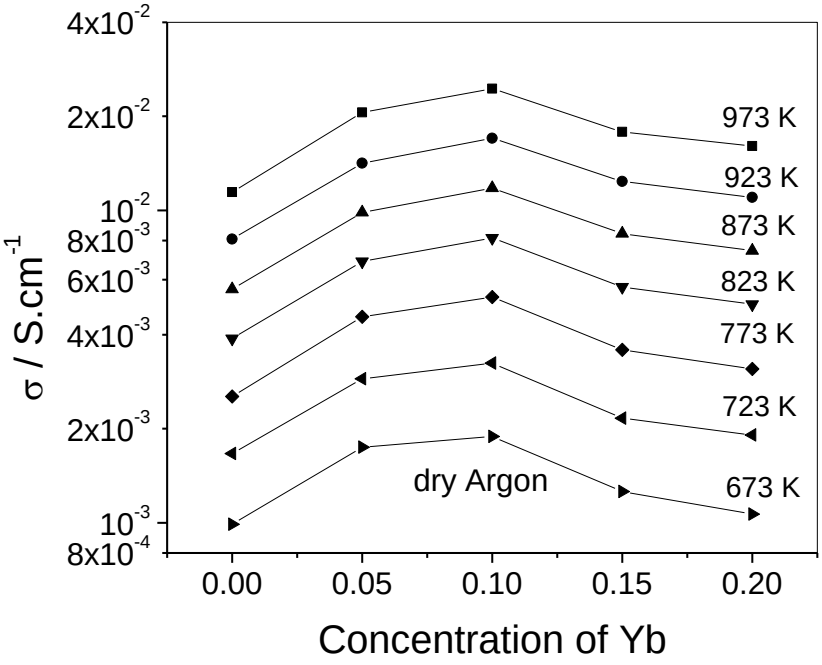

Figure 3-4 The conductivities of Yb doped $BaZr_{0.1}Ce_{0.7}Y_{0.2}O_{3-\delta}$ in dry argon at various temperatures as a function of the concentration of Yb

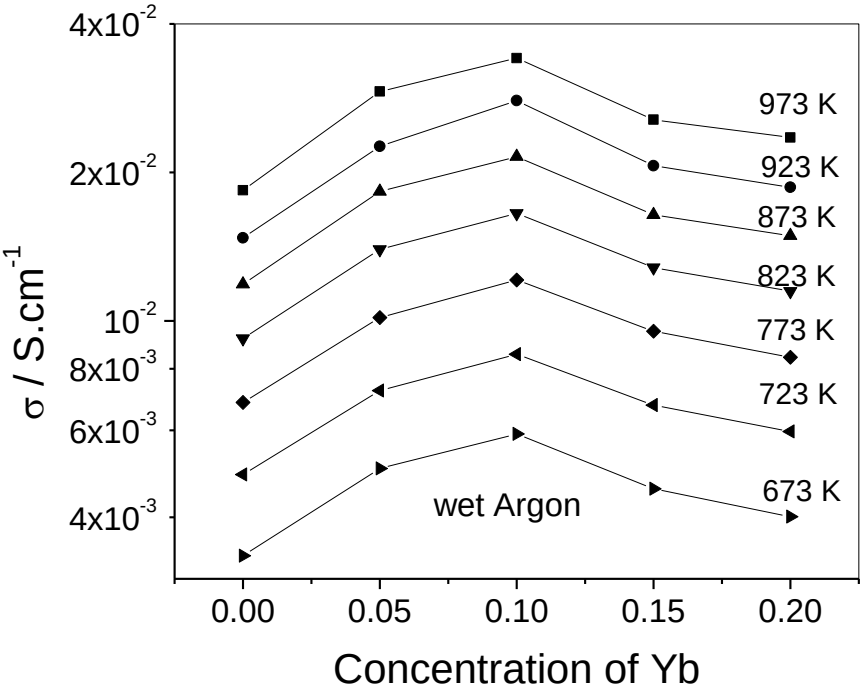

Figure 3-5 The conductivities of Yb doped $BaZr_{0.1}Ce_{0.7}Y_{0.2}O_{3-\delta}$ in wet argon at various temperatures as a function of the concentration of Yb

As discussed above, the dominant conductivity is oxygen ion conductivity in dry argon, and proton conductivity in wet argon. It is clear that the substitute of Y with Yb has similar effect on the generation and migration of the oxygen vacancies and protonic defects. Since the concentration of oxygen vacancy is generally determined by the concentration of alio-valance dopant, further, the electronic conductivity is negligible small, therefore, the concentration of oxygen vacancy should remain the same after replacing Y with Yb. The increase in oxygen ion conductivity could be due to an increased mobility of oxygen vacancies. However, there could be the possibility that there is some oxygen vacancy clusters in $BaZr_{0.1}Ce_{0.7}Y_{0.2}O_{3-\delta}$, and the introduction of Yb alleviate the clustering of oxygen vacancies.

3.3 Characterization of lattice structure and local disorder

A synchrotron light source is a source of electromagnetic radiation produced by a synchrotron, which is artificially produced for scientific and technical purposes by specialized particle accelerators, typically accelerating electrons. The Synchrotron-based X-ray has short wavelength photons which can penetrate matter and interact with atoms as well as high concentration, tunability and polarization thus ensuring focusing accuracy for even the smallest of targets. We have already initiated collaboration with Brookhaven National Laboratory to use beamline X14A for X-ray diffraction and beamline X18A for the X-ray absorption. As it has been already demonstrated in the research on BZCYYb, X-ray diffraction will be continuously employed to check phase formation, reveal structure information and phase/structure evolution with doping level, temperature and hydration when an in-situ measurement is established.

Extended X-Ray Absorption Fine Structure (EXAFS) analysis provides an accurate snapshot of the correlations around a particular atomic species. Therefore, it allows to discriminate different sites that would otherwise average out using diffraction, and constitutes one of the most powerful experimental techniques for the structural investigation of doped crystals. The A and B cation sites in $BaZr_xCe_{1-x}O_3$ perovskites exhibit different coordination numbers, with the A-site being 12-fold coordinated and the B-site being 6-fold coordinated (Figure 3-6)[52]. Consequently, the EXAFS spectra from dopants on one or the other of these two sites will differ, enabling the establishment of the dopant location in the structure. For example, in the BaCeO3 system, Giannici et al [53]employed EXAFS to compare the influences of In, Y and Gd on local structures. It was found that the high solubility of In dopant yielded the incorporation of high concentration of protons but effectively biased the proton diffusivity. To date, no similar fundamental investigation on $BaZr_xCe_{1-x}O_3$ perovskites, it is thus expected that we could establishe the structure-property relationships by the analyses of the local structure and lattice dynamics.

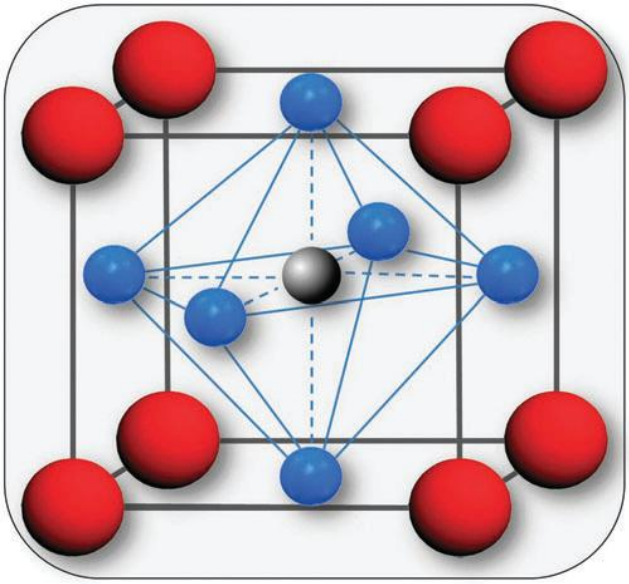

Figure 3-6 Perovskite crystal structure (ABO_3), where the red spheres are the A cations, the grey sphere the B cation, and the blue spheres are the oxygen ions.

Rietveld refinement is conducted on X-ray patterns obtained by synchrotron irradiation. It appears that the co-doping induced negligible distortion of the lattice (Table 1-1), which might be beneficial for maintaining high mobility of oxygen ion and proton.

Table 3-1 lattice parameters of BZCYYb and $BaCeO_3$

Phase	BZCYYb	BaCeO3
Space group (No.)	P n m a (62)	P n m a (62)
a/ Å	8.785	8.779
b/ Å	6.237	6.239
c/ Å	6.221	6.214

Figure 3-7 shows FT EXAFS data of BZCYYb and BZCY on the Ba K- edge. It is commonly believed that the local environment of A-site is not subject to doping. It is

clearly observed that introduction of Yb dopant induced some local reorganization in the Ba-Ce correlations. The main peaks for BZCYYb experienced shift towards left side. Also, introduction of Yb dopant in B-site sharpens the peaks for BZCY. These two features represent that BZCYYb has less local disorder than BZCY, thereby improving oxygen ion and proton mobility.

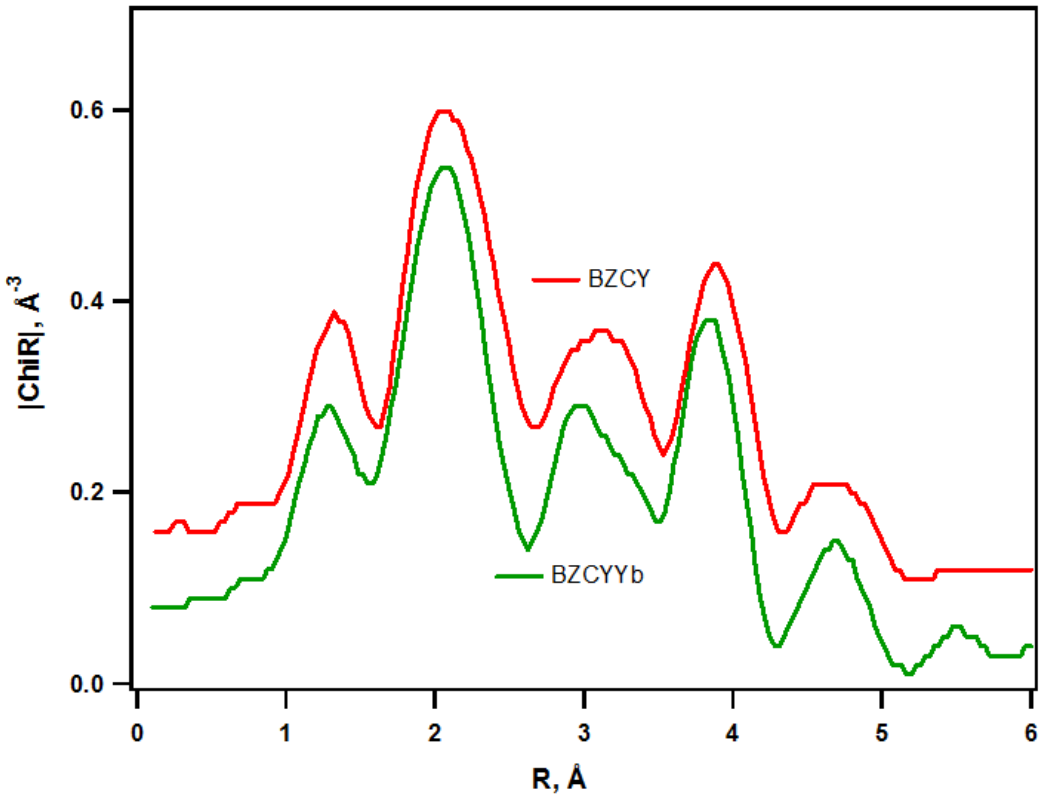

Figure 3-7 FT EXAFS data of BZCYYb and BZCY samples on the Ba K- edge

3.4 $BaZr_{0.1}Ce_{0.7}Y_{0.2-x}Yb_xO_{3-\delta}$ electrolyte under fuel cell operating conditions

When used as the electrolyte in an SOFC, the electronic conductivity of BZCYYb is relatively small, more so at lower temperatures. Figure 3-8 shows the open circuit voltages, together with the Nernst potentials, for a cell based on a BZCYYb electrolyte membrane at different temperatures with wet H_2 (~ 3 v% H_2O) as fuel and air as oxidant. The electronic transference number varies from ~0.02 at 500^oC to ~0.1 at 750^oC, suggesting that the electronic conduction is relatively insignificant at low temperatures.

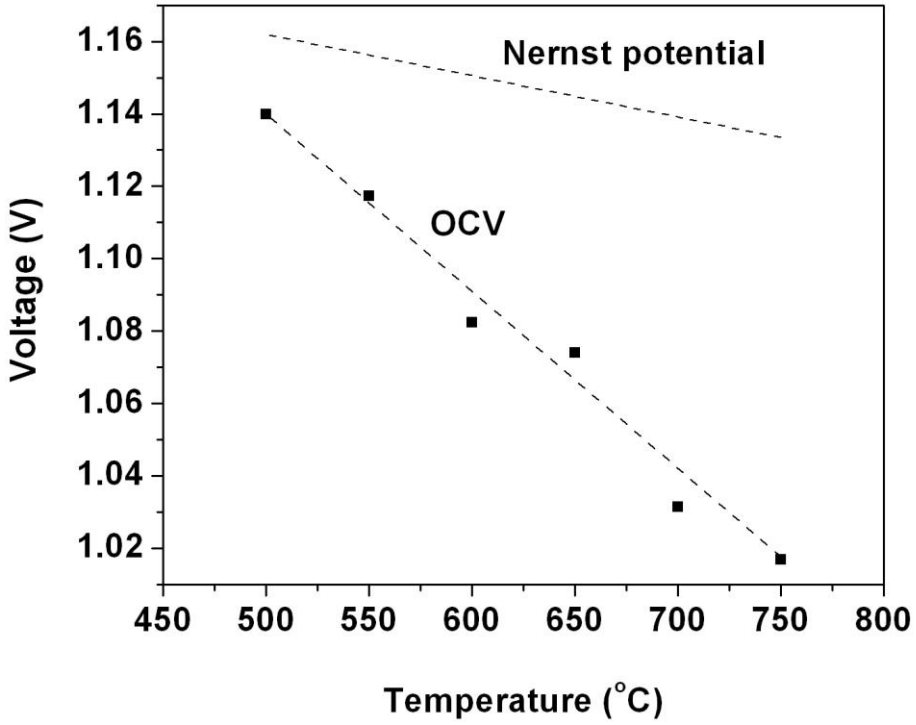

Figure 3-8 Open circuit voltages (OCV) for a cell with a configuration of Pt | BZCYYb | Pt with wet H_2 (~ 3 v% H_2O) as fuel and air as oxidant.

Shown in Figure 3-9 are the current-voltage characteristics and the corresponding power densities at different temperatures for a fuel cell based on BZCYYb electrolyte membrane and $PrBaCo_2O_{5+\delta}$-$Ba(Ce_{0.4}Pr_{0.4}Yb_{0.2})O_{3-\delta}$ composite cathode fired at 1000°C. The open circuit voltages (OCV) at 750, 700 and 650°C were 0.99, 1.03 and 1.08V, respectively, indicating that the BZCYYb electrolyte was sufficiently dense and exhibited negligible electronic conduction. The peak power densities are about 1.34, 1.12 and 0.94 W/cm^2 at 750, 700, and 650°C, respectively. The observed current and power densities represent the highest performance ever reported in the literature for SOFCs based on an oxide proton conductor. The observed fuel cell performances are very encouraging, especially for operation at low temperatures to dramatically reduce the cost of SOFC systems.

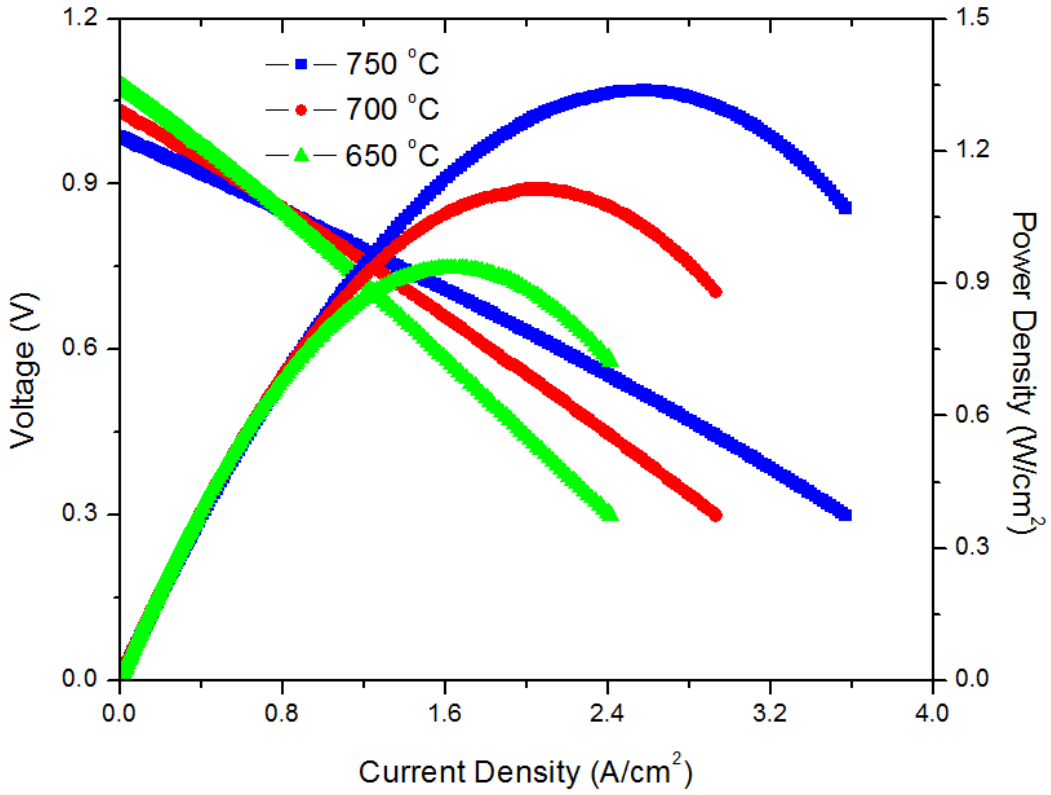

Figure 3-9 Cell voltages and power densities as a function of current density for fuel cells consisting of Ni-BZCYYb anode, 20 µm-thick BZCYYb electrolyte, and $PrBaCo_2O_{5+\delta}$-$Ba(Ce_{0.4}Pr_{0.4}Yb_{0.2})O_{3-\delta}$ cathode.

Shown in Figure 3-10 are the polarization resistances of Ni-BZCYYb/BZCYYb/PBC-BCPY cells. These polarization resistances were determined from impedance spectroscopy under open circuit conditions. The polarization resistances of cells with PBC-BCPY are estimated to be only 0.003, 0.008, and 0.029 Ω cm^2 at 750, 700, and 650°C, respectively.

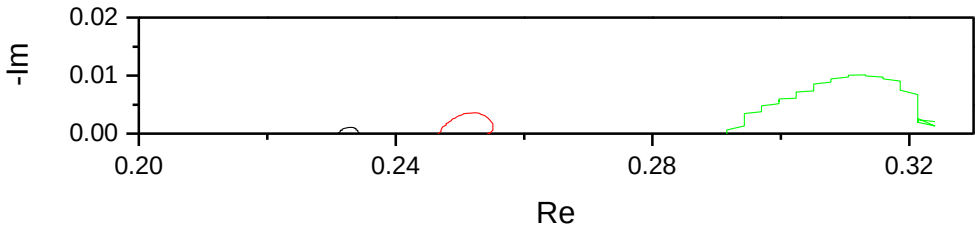

Figure 3-10 Impedance spectra of cells measured at 750, 700 and 650 ^{o}C under OCV conditions

It is critical to evaluate durability of the cells with BZCYYb electrolyte and PBC-BCPY cathode. Any instability of BZCYYb at high water activities and deterioration of electrode may lead to degradation in fuel cell performance. Figure 3-11 shows the performance of cells with thicker electrolyte (60 um) operated at 700 mA/cm^2 at 650^{o}C. The cell voltage was relatively stable up to 180 h, implying superior chemical stability of BZCYYb, steady electric characteristics of electrode, and strong bonding between electrolyte and electrode.

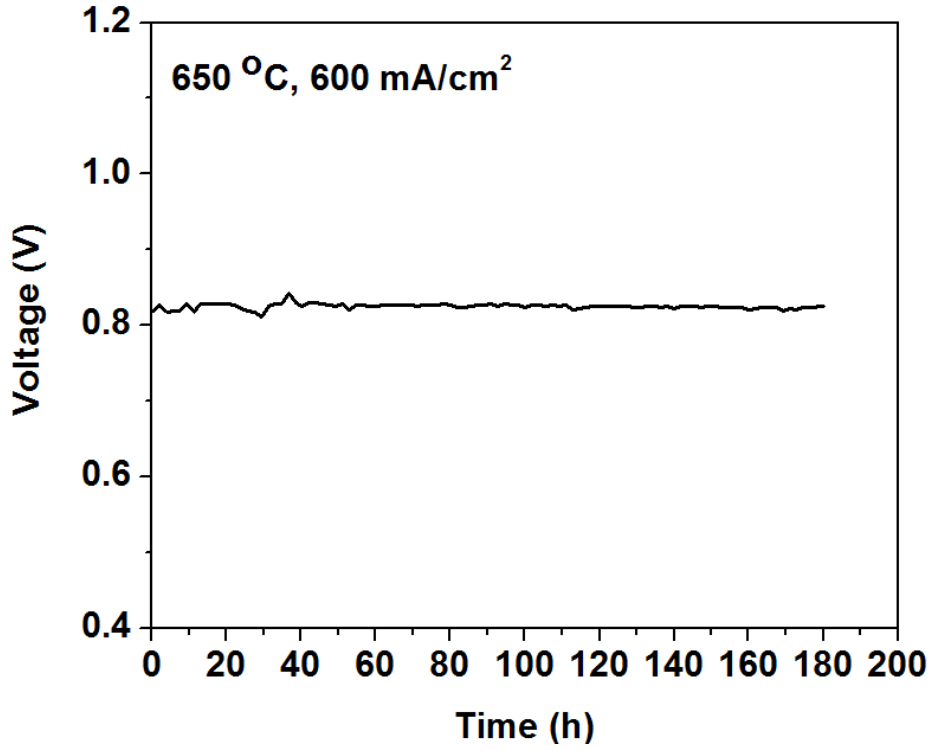

Figure 3-11 Terminal voltage of a typical cell with PBC-BCPY cathode as a function of operation time

3.5 Tailoring the mole ratio of Zr to Ce

With the increasing fuel utilization, $BaZr_xCe_yM_{1-x-y}O_{3-\delta}$ based materials tend to react with the fuel products such as H_2O and CO_2 especially at low temperature. Thus, for the purpose of using the BZC based cell at 650 ^oC, it is essential to explore a BZC conductor with higher stability while maintaining the good conductivity. It is well established that barium zirconate based materials are much more stable in atmospheres containing H_2O and CO_2 in spite of the lower conductivity comparing with barium cerate. However, the electrical conductivity decreases with increasing the Zr/Ce ratio. The objective of this work is to improve the chemical and electrochemical stability of $BaZr_{0.1}Ce_{0.7}M_{0.2}O_{3-\delta}$ without sacrificing the electrical conductivity through tailoring the Zr/Ce ratio as well as selecting optimal co-dopants in B-site.

Figure 3-12 presents the conductivities of $BaZr_{0.4}Ce_{0.4}Gd_{0.05}Yb_{0.15}O_{3-\delta}$ and $BaZr_{0.1}Ce_{0.7}Y_{0.1}Yb_{0.1}O_{3-\delta}$ measured at different temperatures. Obviously, introduction of more Zr content in Ce site reduced the electrical conductivity throughout all the testing temperatures. For example, the conductivity of BZCYYb at 750 oC is 0.056 S/cm while the conductivity of BZCGYb is only 0.026 S/cm, indicating that the high basicity of components in proton conductor is of paramount importance. Also, it has been reported that increasing Zr content may lower grain size and thus lead to large grain boundary surface. It is noted that the activation energies of these two conductors are similar, which reflects that the change of Zr/Ce ratio exerts negligible effect on conduction mechanism. While the conductivity of BZCGdYb is decreased with respect to BZCYYb, it is much higher than those in the recent reports for BZC systems with high Zr/Ce ratio. Table 1 summarizes the conductivity of BZC materials with Zr/Ce raio of 1. The much-improved conductivity represents that the co-doping strategy is still applicable in the Zr-rich materials system.

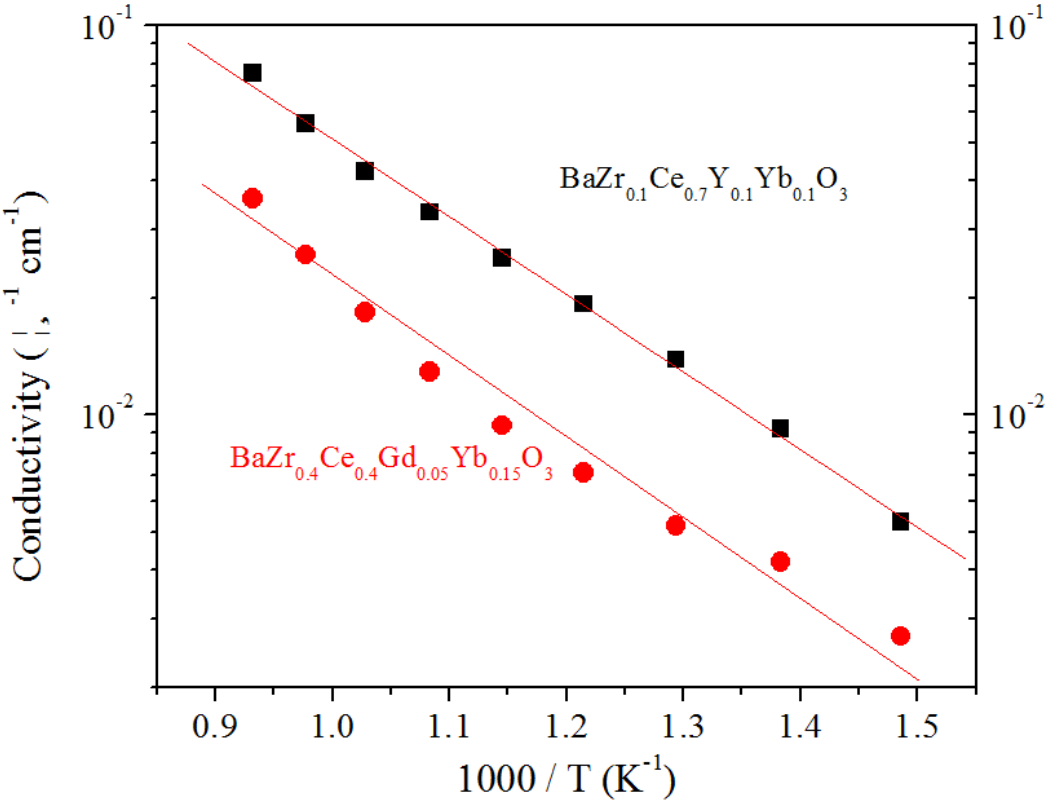

Figure 3-12 conductivity of $BaZr_{0.4}Ce_{0.4}Gd_{0.05}Yb_{0.15}O_{3-\delta}$ as a function of operating temperature

Table 3-2 conductivity comparison between various $BaZr_xCe_yM_{1-x-y}O_{3-\delta}$ materials

Composition	Conductivity at 600 ^oC (S/cm)	Reference
$BaZr_{0.4}Ce_{0.4}Gd_{0.05}Yb_{0.15}O_{3-\delta}$	0.01	This work
$BaZr_{0.5}Ce_{0.3}Y_{0.2}O_{3-\delta}$	0.004	Traversa group, SSI, 2008,179
$BaZr_{0.4}Ce_{0.5}Y_{0.1}O_{3-\delta}$	0.005	Iwahara group, SSI, 2000, 138
$BaZr_{0.4}Ce_{0.4}Sc_{0.2}O_{3-\delta}$	0.001	Irvine group, SSI, 2007,178

3.6 Summary

Yb and Y co-doped BZC conductor demonstrated the highest electrical conductivity below 750 oC ever reported among the electrolyte materials in SOFCs. The conductivities were sensitive to doping and partial pressure of oxygen, hydrogen, and water; it can transport both proton and oxygen ion under the SOFCs operating conditions. It was concluded that the two dopants on the B-site function in a cooperative fashion to significantly improve the ionic conductivity. The enhanced ion transport could be reasonably attributed to the slight distortion of the lattice structure and less disturb of the local atomic environment upon introduction of the two dopants in B-site.

When used as electrolyte in anode-supported structure, the open circuit voltages are close to the theoretical Nernst potential, indicating the negligible electron conduction under fuel cell operating conditions. With the thin and dense BZCYYb electrolyte membrane, the SOFCs yielded much-improved power density at lower temperatures, for example, 0.94 W/cm2 at 650 ^oC.

While increasing the mole ratio of Zr to Ce reduced the electrical conductivity, the Gd and Yb co-doped BaCe0.4Zr0.4M0.2O3 showed higher conductivity relative to

that for conductors with similar Zr/Ce ratio. The improved ion transport may be also ascribed to the synergetic effect of the two dopants.

CHAPTER 4

A NOVEL ANODE WITH ENHANCED COKING AND SULFUR TOLERANCE

4.1 Experimental

4.1.1 Fabrication of test cells

The button cells with a configuration of Ni-BZCYYb|BZCYYb|cathode were fabricated as follows. First, a mixture of NiO and BZCYYb powder (weight ratio of 65:35) was pressed into pellets (~0.6 mm thick and 13 mm in diameter), followed by pre-firing at 800 ^{o}C for 2 h. Second, a thin layer of BZCYYb (~10 μm) was deposited on the anode support by a solution coating process followed by co-firing at 1400 ^{o}C for 5 h. Third, a BZCY-LSCF slurry was screen printed onto the top of the BZCYYb electrolyte and fired at 1000 ^{o}C for 2 h to form a porous cathode (~30 μm thick). The Ni-BZCYYb|SDC|LSCF cells were prepared by the same method. The LSCF cathode was fired at 1050 ^{o}C for 2 h. The SDC and LSCF layer thicknesses are about 20 and 30 μm, respectively. For the Ni-BZCYYb|YSZ|cathode cells, a YSZ disk (150 μm thick and 20 mm in diameter) was fabricated by tape casting and firing at 1450 ^{o}C for 5 h. Next, a GDC buffer layer (5 μm) was screen-painted on both sides of the YSZ and fired at 1200 ^{o}C for 2 h. Finally, NiO-BZCYYb (analogous to NiO-GDC and NiO-YSZ) anodes and LSCF cathodes were screen-painted on the GDC buffer layers, followed by firing at 1050 ^{o}C for 2 h. For the cells with a BZCYYb infiltrated Ni-YSZ anode, solution infiltration was used to deposit a thin layer of BZCYYb on the porous Ni-YSZ, followed by calcination at 850 ^{o}C for 2 h to obtain a pure phase. The active electrode areas for all cells are 0.21 cm^{2}.

4.1.2 Electrochemical testing

For H_2S tests, each button cell was sealed on an alumina tube and heated up to 750^oC in ambient air. Since H_2S can dissolve in water, a separate flow of N_2 was passed through a water bubbler to bring water vapor into the system. H_2S concentration was adjusted by mixing H_2 and a certified mixture gas containing 100 ppm H_2S in H_2 using two mass flow controllers. The flow rate was 30 mL/min. All fuel cells were first conditioned at a constant current density in clean H_2 to obtain steady state performance before switching to H_2S-contaminated H_2 .

For hydrocarbon testing, following reduction of anode in H_2, the cell was conditioned in H_2 as was just described, and then dry or wet C_3H_8 with a flow rate of 2 mL/min (passing through a water bubbler at room temperature) was fed into the cell at 750 ^oC.

4.1.3 Other Characterization

X-ray diffraction with CuKα radiation (Philips, PW-1800) and Raman spectroscopy with a 514 nm excitation source (Renishaw, Raman System 2000) were used to analyze crystal structure and phase composition. Raman was also used to probe water adsorbed on sample surfaces. The microstructures of fuel cells before and after testing were revealed using a scanning electron microscope (SEM; LEO 1530) equipped with energy dispersive x-ray spectroscopy (EDS). The stability of BZCYYb powders was tested by exposing materials to H_2 containing 50 v% H_2O (passed through a water bubbler at 85^oC) and 50 v% CO_2. The composition of the inlet and outlet gas mixture was monitored online by mass spectrometer (MS, Hiden HPR 20) at room temperature. All standard electrochemical experiments were performed using a Solartron 1286 electrochemical interface and a Solartron 1255 HF frequency response analyzer.

4.2 Electrochemical behaviors of Ni-BZCYYb anode in H_2S/H_2

The sensitivity of the Ni-BZCYYb anode to sulfur poisoning was investigated by gradually increasing the concentration of H_2S in hydrogen. The terminal voltages of the same cells (with BZCYYb and SDC as the electrolyte) at 750^{o}C were recorded as a function of time when the fuel was contaminated with different concentrations of H_2S (Figure 4-1). The Ni-BZCYYb anodes for both cells showed no observable change in power output as the fuel was switched from clean hydrogen to hydrogen contaminated with 10, 20, or 30 ppm H_2S.

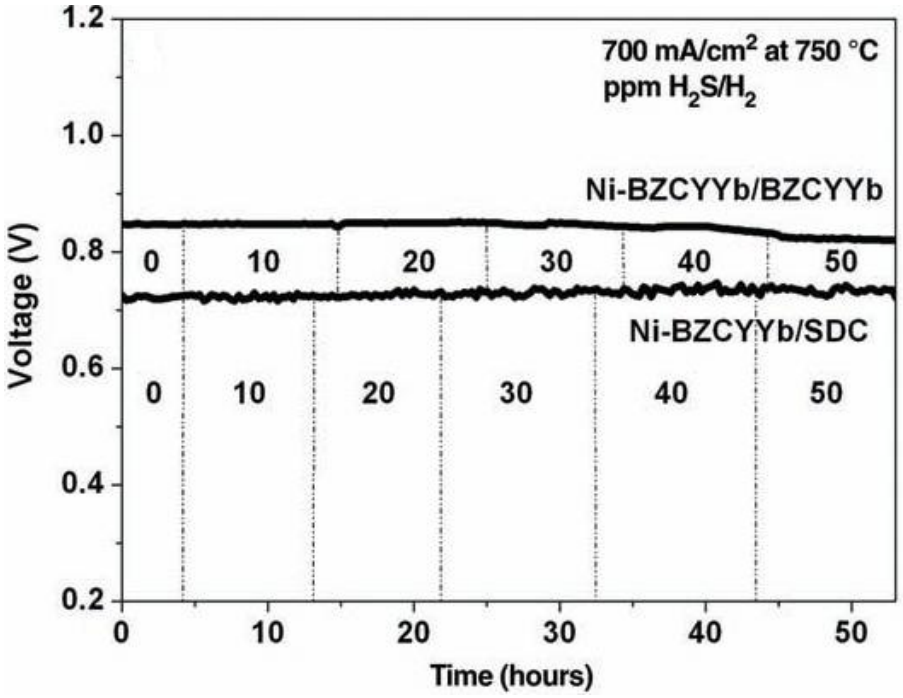

Figure 4-1 Terminal voltages measured at 750°C as a function of time for two cells with a configuration of Ni-BZCYYb | BZCYYb | BZCY-LSCF and Ni-BZCYYb | SDC | LSCF operated at a constant current density of 700 mA/cm^2 as the fuel was switched from clean H_2 to H_2 contaminated with different concentrations of H2S (the number in each time interval represents the concentration of H_2S in wet hydrogen in ppm)

This sulfur tolerance was also evident from our impedance data (Figure 4-2 (a) and (b)). When water was absent from the fuel, the electrode polarization resistance increased about 80% upon exposure to 20 ppm H_2S, from ~0.06 ohm cm^2 in H_2 to ~0.11

ohm cm^2 in H_2 containing 20 ppm H_2S, as commonly observed in previous studies [54]. When a small amount of water (only ~3 v%) was introduced with the fuel, the electrode polarization resistance in hydrogen with 20 ppm H_2S was reduced to that in clean hydrogen, as can be interpreted from the collected impedance spectra (Figure 4-2(b)). It is believed that sulfur poisoning is caused by the strong adsorption of the elemental sulfur on Ni surface and the three-phase boundaries (TPB) between Ni, electrolyte, and the fuel. Sulfur would then block the active site for fuel oxidation in a traditional Ni-YSZ anode and increase the polarization resistance [55, 56]. We hypothesized that water might adsorb on the surface of BZCYYb to facilitate the oxidation of H_2S or elemental sulfur to SO_2 at or near the active sites. Unlike H_2S or elemental sulfur, SO_2 readily desorbs from electrode surface [57]. We note that when the fuel was switched to hydrogen containing 40 and 50 ppm H_2S, the cell with a BZCYYb electrolyte (a mixed proton and oxide ion conductor) suffered some drop in power output whereas the cell with an SDC electrolyte (an oxide ion conductor) displayed no observable change in performance. One possible explanation is that more water was produced at the active sites on the anode of the cell with an SDC electrolyte under active operation because of increased hydrogen oxidation; the water produced at the active sites is beneficial to sulfur removal.

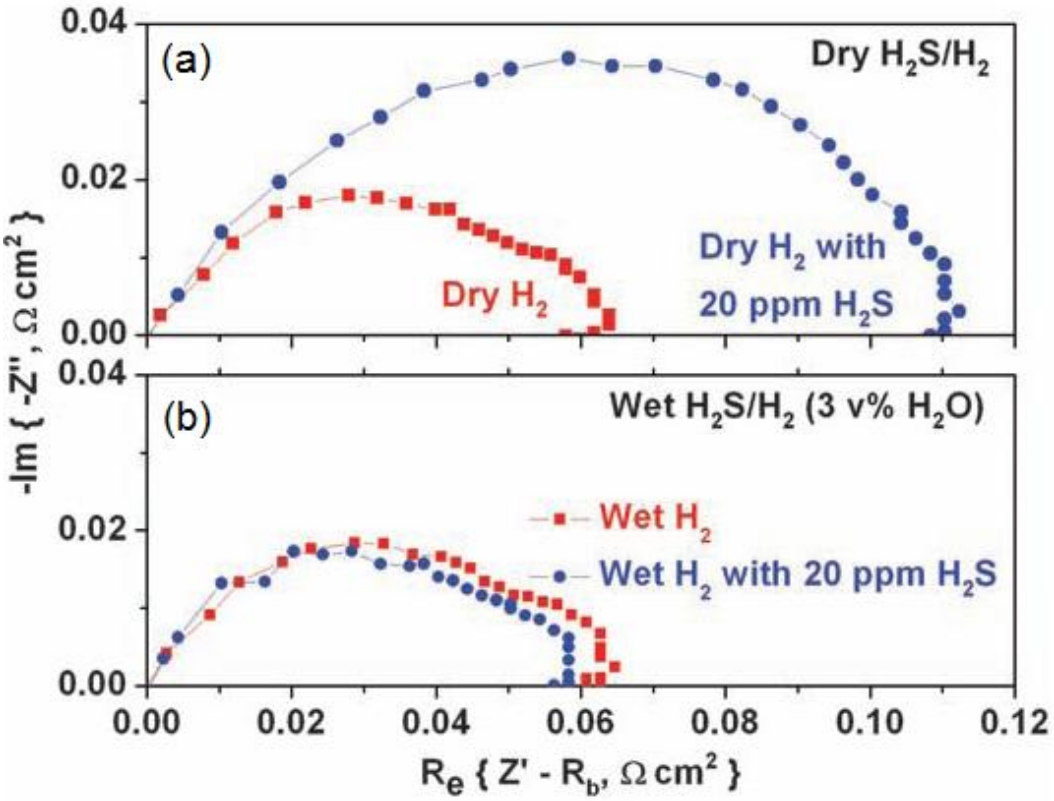

Figure 4-2 Impedance spectra measured under OCV conditions at 750°C for a cell with a configuration of Ni-BZCYYb | SDC | LSCF in clean H_2 and in H_2 contaminated with 20 ppm H_2S for dry H_2S/H_2 gases (a) and wet H_2S/H_2 gases (with ~3 vol % H_2O) (b).

Continuous operation in H_2S-contaminated fuel for a longer period of time (200 to 1000 hours) further confirmed that sulfur poisoning can be fully suppressed in the presence of a small amount of steam. Figure 4-3 shows the performance of a cell with a configuration of BZCYYb/Ni-YSZ | YSZ | LSCF operated in wet hydrogen contaminated with 10 ppm H_2S. The Ni-YSZ anode was coated with a thin layer of BZCYYb using a solution infiltration process. This cell demonstrated that the state-of-the-art fuel cells based on YSZ, Ni-YSZ|YSZ|LSCF, can be readily modified by a thin film coating of BZCYYb to enhance the tolerance to sulfur poisoning. Further, the cell showed a stable power output for 1000 h, implying that BZCYYb exhibits considerable stability for long-term sulfur tolerance.

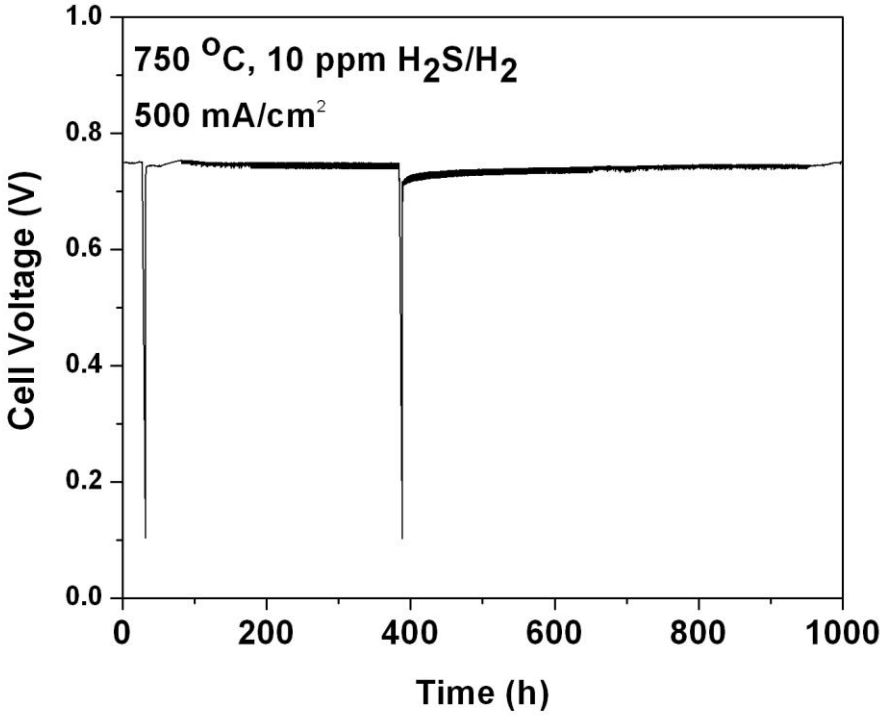

Figure 4-3 Terminal voltage for a cell with a configuration of BZCYYb/Ni-YSZ | YSZ | LSCF operated at 500 mA/cm^2 in wet hydrogen containing 10 ppm H_2S at 750 ^oC. The Ni-YSZ anode was infiltrated with a BZCYYb solution to introduce a thin coating of BZCYYb on the surface of the Ni-YSZ anode.

Figure 4-4 shows the performance of a Ni-BZCYYb | SDC | LSCF cell operated at a constant current density of 700 mA/cm^2 at 700 ºC when the fuel was switched from wet hydrogen to wet hydrogen contaminated with 30 ppm H_2S, indicating that sulfur poisoning can be fully suppressed in the presence of a small amount of water. After the 200 h operation, the Ni-BZCYYb anode surface was examined by EDS under SEM, but there was no sulfur detected.

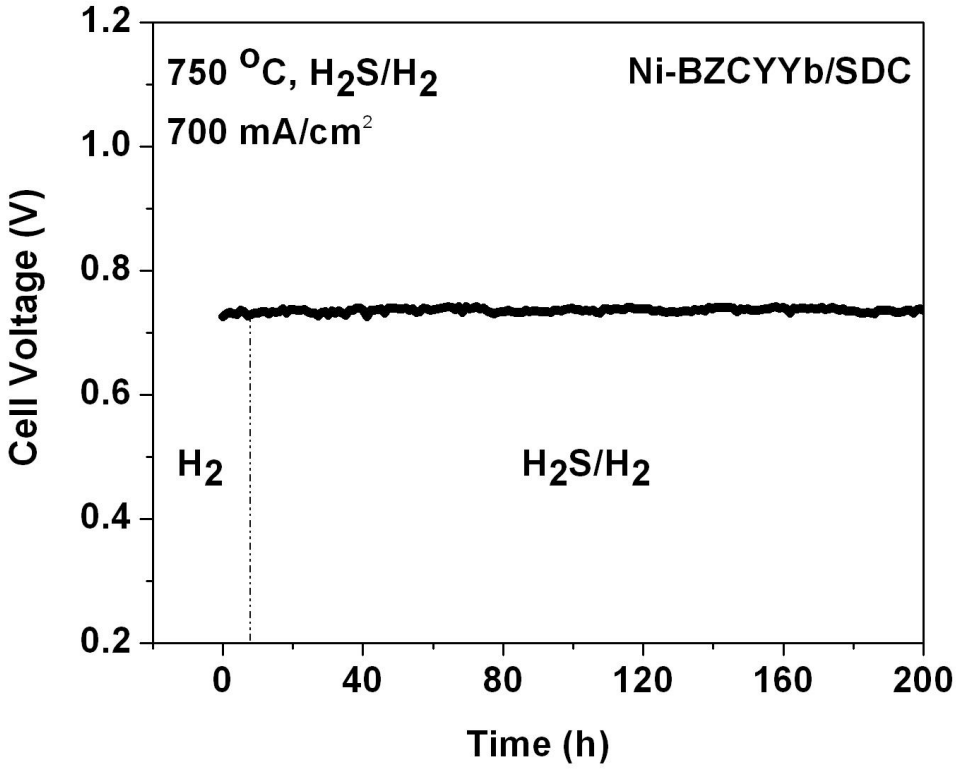

Figure 4-4 Terminal voltage for a Ni-BZCYYb | SDC | LSCF cell operated at a constant current density of 700 mA/cm^2 in wet H_2 and wet H_2 containing 30 ppm H_2S at 750 ^{o}C. The fuel was switched to wet H_2 containing 30 ppm H_2S after a few hours operation in wet H_2.

4.3 Electrochemical behaviors of Ni-BZCYYb anode in C_3H_8

The coking resistance of this material was demonstrated in a cell with a Ni-BZCYYb cermet anode, YSZ electrolyte, and LSCF cathode. When dry propane was used as fuel, the open circuit voltage (OCV) dropped quickly within minutes (Figure 4-5), an indication of rapid carbon deposition as expected for a conventional Ni-based anode. In contrast, when wet (~3 v% steam) propane was used as fuel, the OCV was very stable

(Figure 4-5), suggesting that the observed tolerance to coking is also attributed to the presence of a small amount of steam.

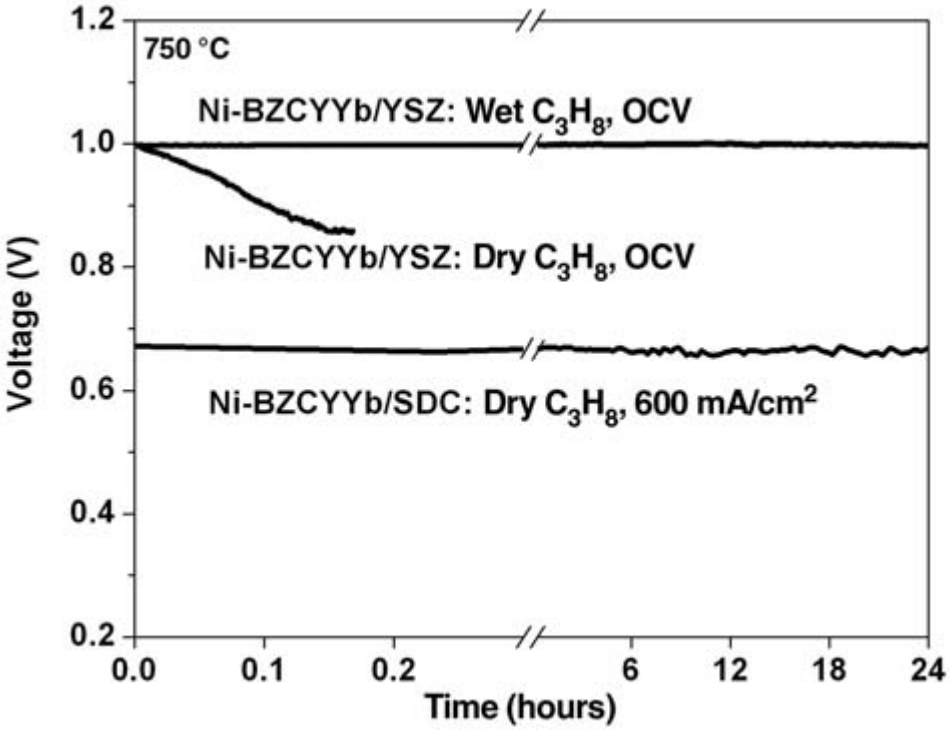

Figure 4-5 Open cell voltages measured at 750°C as a function of time for a cell with a configuration of Ni-BZCYYb | YSZ | LSCF with dry and wet propane as the fuel, and the terminal voltages for another cell with a configuration of Ni-BZCYYb | SDC | LSCF operated at 600 mA/cm^2 using dry propane as fuel. Stationary air was used as oxidant in all cases.

The whole surface of the Ni-BZCYYb anode exposed to wet (~3v% H2O) propane appeared clean and free of carbon deposition, as revealed using Raman spectroscopy. Figure 4-6 shows some typical Raman spectra collected from Ni-BZCYYb anodes after exposure to wet and dry propane under open circuit conditions. While the disordered and graphitic carbon peaks (near 1340 cm^{-1} and 1580 cm^{-1}, respectively) were readily observable from the anode exposed to dry propane (Figure 4-6a), they were largely absent from the spectra collected from the same anode surface after exposure to

wet (~3 v% H_2O) propane (Figure 4-6b). Out of 100 spectra collected from 100 points uniformly distributed in a rectangular mesh covering an area of 80 μm x 60 μm, only 42 spectra show a trace amount of carbon, and are comparable to Figure 4-6c, an indication of minimal carbon deposition.

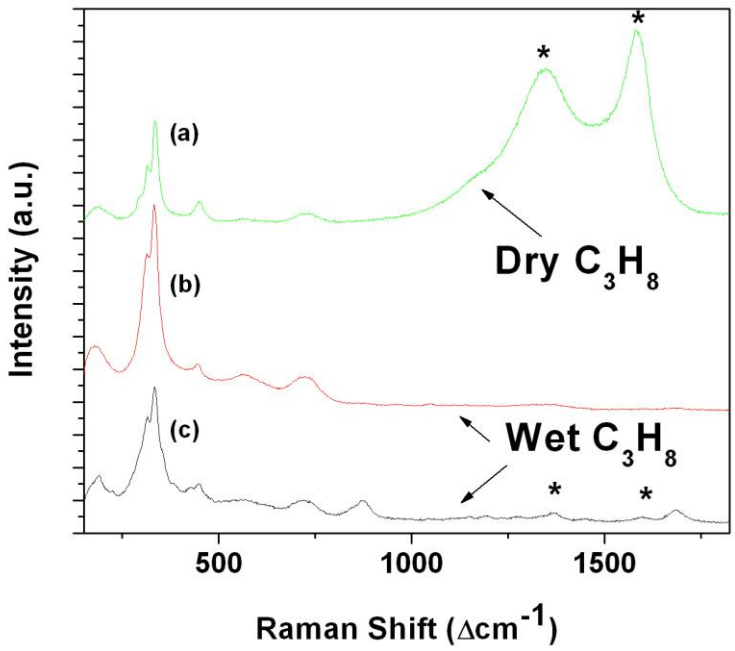

Figure 4-6 Raman spectra collected from Ni-BZCYYb anode in a cell with a configuration of Ni-BZCYYb | YSZ | LSCF after exposure to (a) dry and (b), (c) wet propane at 750^{o}C for 3 hours under OCV condition.

The OCVs of the cell are greater than those observed for other alternative anode materials, [22, 23, 26, 58] and approach 1.00 V for wet propane. Coking may be inhibited by water reforming propane on the surface of BZCYYb and the reforming products (H_2 and CO) adsorb on the active sites of the anode surface, leading to a stable OCV output. We note that conventional Ni-YSZ and Ni-GDC anodes suffered severe carbon deposition under the same conditions.

This catalytic activity of Ni-BZCYYb for in situ reforming of hydrocarbons is further demonstrated in operating cells powered by propane. Figure 4-7 shows open circuit voltages and power output at a constant current density of 300 mA/cm^2 for a cell with a configuration of Ni-BZCYYb |YSZ | LSCF when wet (~3 v% steam) propane was used as fuel and air as oxidant. It demonstrated stable OCV and sustained power output for over 100 h when wet propane was used as fuel.

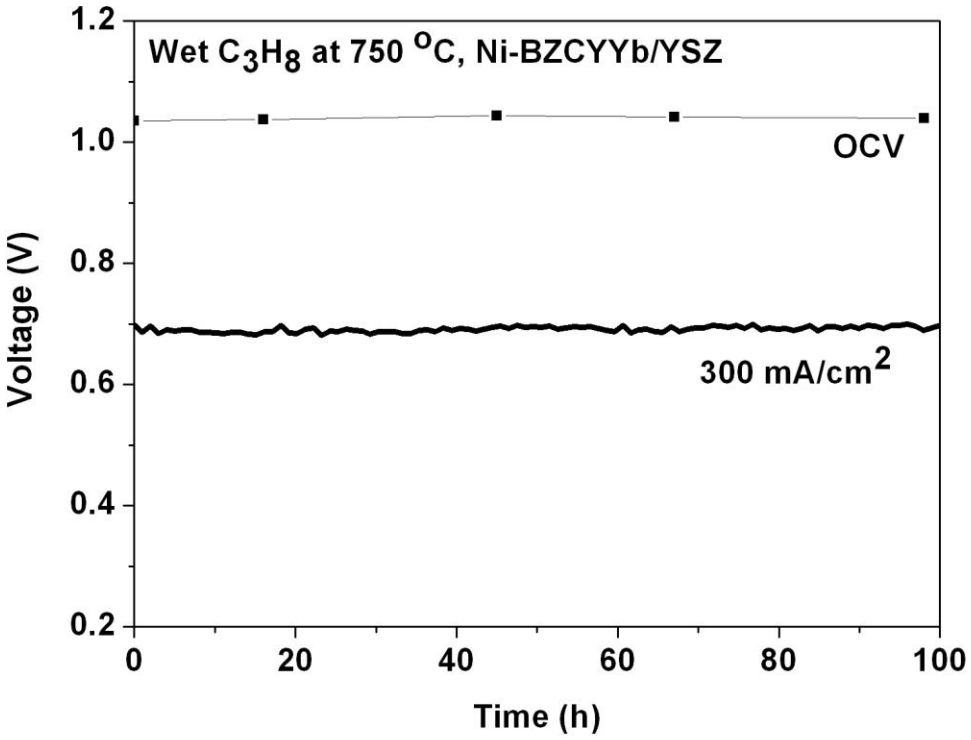

Figure 4-7 Terminal voltages measured at a current density of 300 mA/cm^2 and OCVs (intermittently monitored) at 750^{o}C for a cell with a configuration of Ni-BZCYYb |YSZ| LSCF with wet (with ~3 v% H_2O) propane as fuel and stationary air as oxidant.

The outlet gas from this cell under steady state operation was analyzed using mass spectrometry, as shown in Figure 4-8. Due to the instrumental limitations, it is not possible to determine the relative contributions of the fragments $[CO]^+$ and $[C_2H_4]^+$ to the

mass signal at *m/z* = 28. However, our analysis of oxygen mass balance suggests that the ratio of CO to C_2H_4 is relative small. At an operating current of 63 mA (= 0.21 cm^2 ×300 mA/cm^2), the oxygen flux going through the electrolyte to the anode was ~3.21×10^{-7} mol/s or 0.431 mL/min. Since the concentrations of H_2O and CO_2 in the outlet gas mixture were 3.58 v% and 2.34 v%, respectively, the concentration of CO in the outlet gas should be ~ 2.65 v%, considering that ~3 v% of water was fed with propane in the inlet gas. Analysis of carbon mass balance suggests that the mass of carbon for the inlet gas is slightly larger than that for the outlet gas. This is reasonable since small amount of carbon deposits were observed on the gas feeding tube walls after operation. It appears that a large fraction of C_3H_8 was converted to C_2H_4 and CH_4, but the details about cracking, reformation, and electrochemical oxidation during fuel cell operation are still unknown. However, it is certain that the *in situ* reforming and electrochemical oxidation are sufficiently fast to avoid carbon buildup at the anode.

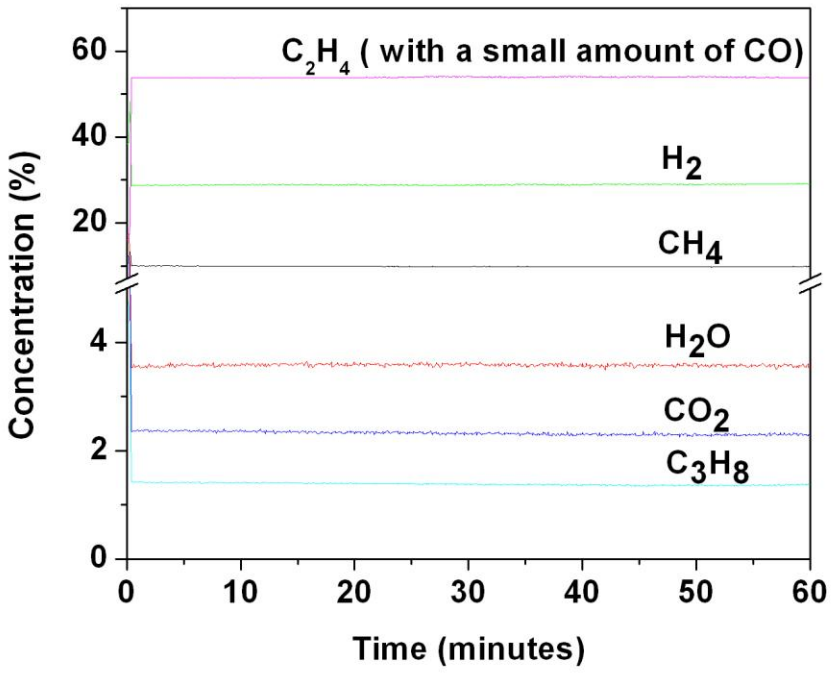

Figure 4-8 A typical concentration profile of the outlet gas mixture monitored by mass spectrometer during operation of a Ni-BZCYYb | YSZ | LSCF cell (electrode area 0.21 cm^2) at a constant current density of 300 mA/cm^2 in wet C_3H_8 (~ 3 v% H_2O). The flow rates for the inlet and outlet gas are 2.0 and 4.5 mL/min, respectively.

Because steam is produced on the anode surface of an operating cell when an oxygen anion conductor (e.g., SDC) is used as the electrolyte, tolerance to coking of BZCYYb-based anodes may be further enhanced by an operating current of such a fuel cell. Indeed, when the operating current density is sufficiently high, cells based on an SDC electrolyte (Figure 4-5) can even operate in dry propane, producing stable power output without observable degradation. Microanalysis of the anode before and after operation in dry propane for 24 hours indicates that there was no visible change in microstructure and no observable carbon deposition (Figure 4-9). It appears that in situ reformation of hydrocarbons has prevented carbon deposition on the anode when an adequate amount of water is produced at the active sites under the operating conditions.

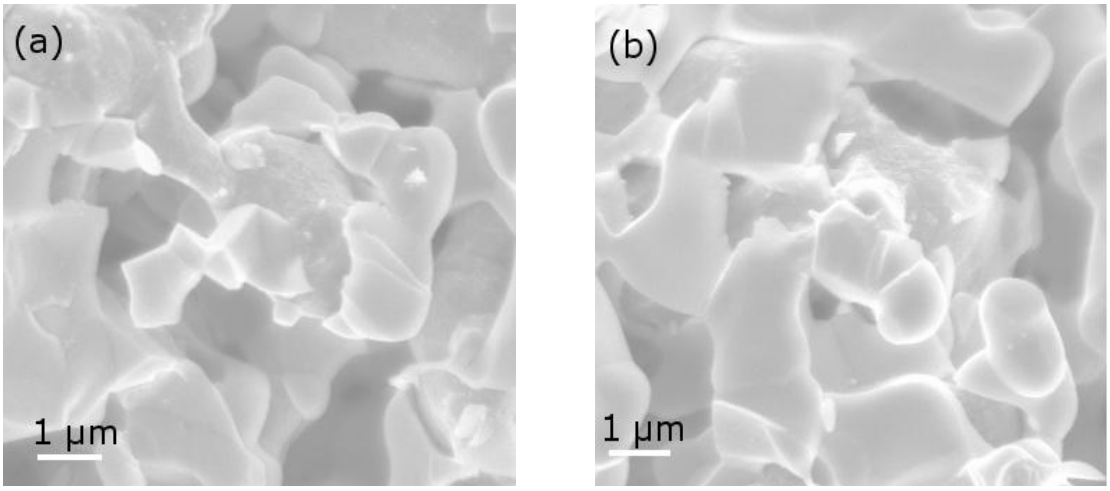

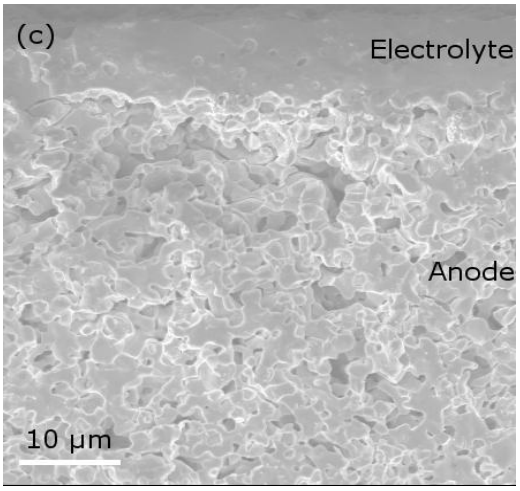

Figure 4-9 Morphologies of the Ni-BZCYYb anode of a Ni-BZCYYb |SDC| LSCF cell (a) before and (b) after operation in dry propane at a constant current density of 600 mA/cm^2 for 24 hours. (c) a cross-sectional view of the cell after operation showing the anode/electrolyte interface.

4.4 Probing water on the surface of BZCYYb

We used Raman spectroscopy to probe for the presence of water on the surface of BZCYYb. Previous studies suggest that the characteristic OH-bond vibration modes for water appear in the 3100-3700 cm^{-1} regime [18, 59]. We collected Raman spectra from BZCYYb at different times of exposure to wet argon (~3 v% water) at room temperature, where incorporation of water into the bulk phase of BZCYYb is unlikely or insignificant because of limited bulk diffusion. The BZCYYb powder sample was first dried at 400°C under evacuation for 10 hours to remove water from the sample. Upon exposure to wet (3 v% H_2O) argon at room temperature, the mode centered near 3310 cm^{-1} appeared quickly, while the mode near 3580 cm^{-1} emerged more slowly over time. The presence of the modes in the 3100-3700 cm^{-1} range, particularly the mode that peaks near 3580 cm^{-1} (Figure 4-10), is strongly indicative of multi-layered surface water molecules, as modes at higher wave-numbers correspond to subsequent layers of water with weaker hydrogen

bonds [60]. Thus, one possible explanation for this behavior is that a strongly bonded layer of water accumulates at the surface quickly in a wet atmosphere, while subsequent layers of water build up more slowly. These features are notably absent for the sample exposed to dry gas.

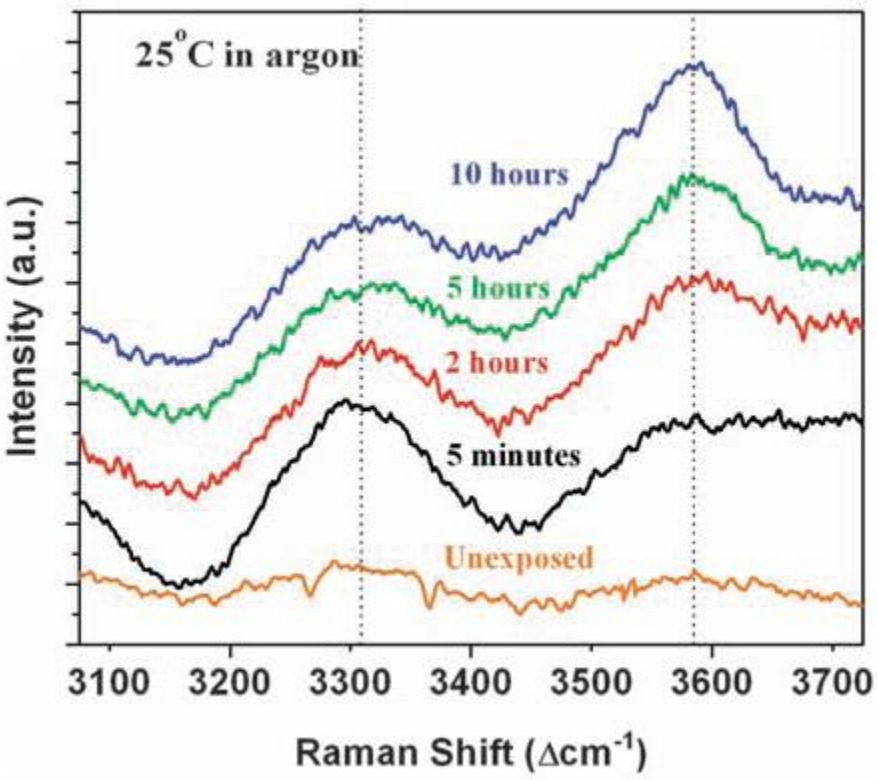

Figure 4-10 In situ Raman spectra collected from BZCYYb samples at room temperature under wet argon gas at various exposure times after a drying treatment at 400°C under evacuation for 10 hours.

Spectra collected in situ from samples held under the same gas conditions at 500ºC display similar features and contrast (Figure 4-11). Because most fuels (including H_2) are humidified at room temperature (yielding ~3 v% H_2O in gas) for typical operation of SOFCs, no excess water is needed to achieve the desired tolerance to H_2S contaminants.

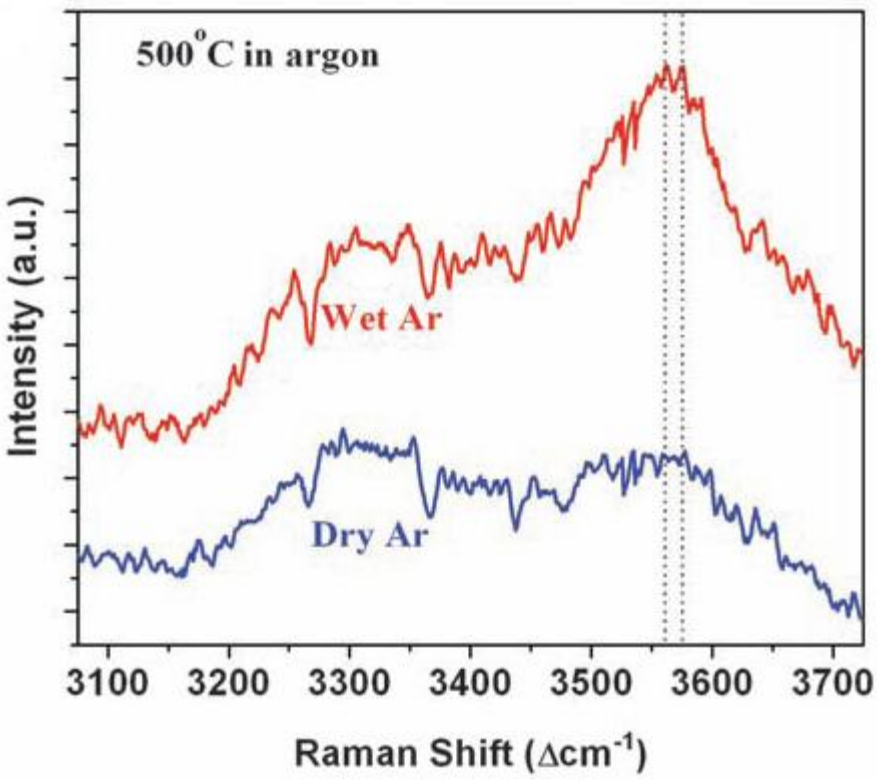

Figure 4-11 In situ Raman spectra collected from BZCYYb samples at 500 ^{o}C in dry and wet argon.

4.5 Modification of Ni surface by BZCYYb traces

It is previously hypothesized that the sulfur and coking tolerance capabilities of the Ni-BZCYYb anode lied in its affinity for water. One would expect that the presence of water on BZCYYb could readily remove the carbon at the three-phase boundaries (TPB) between Ni, BZCYYb, and the fuel; however, the Ni surfaces away from TPB might not be protected by the water layers on BZCYYb. In fact, minimal carbon deposition was observed on the whole Ni surfaces after operation of Ni-BZCYYb anode in C_3H_8. Thus, to unravel the complete mechanisms responsible for the tolerance capabilities of Ni-BZCYYb anode, it is essential to investigate the compositions and electrocatalytic activity of Ni surfaces in this cermet anode.

A detailed study was carried out on Ni surfaces in Ni-BZCYYb anode. It was identified that co-firing of BZCYYb and NiO mixture at 1400 ^{o}C during fabrication of anode/electrolyte bilayers resulted in spreading of elements from BZCYYb to the surface of NiO grains. After reduction in humidified H_2, the Ni electrocatalyst in the cermet anode was modified by nanostructured layers which effectively minimize the tendency of coking. Figure 4-12 shows a typical morphology of Ni-BZCYYb anode and EDS spectrum collected from a Ni area, suggesting that Ba is present in the Ni area. Apparently, the Ni grains had been contaminated by BZCYYb. The contamination of Ni surface by BZCYYb most likely happened during the co-firing of BZCYYb and NiO (at 1400ºC for 5 hours). In all likelihood, the spreading of elements from BZCYYb to the surface of NiO grains during co-firing resulted in a surface that has enhanced resistance to coking.

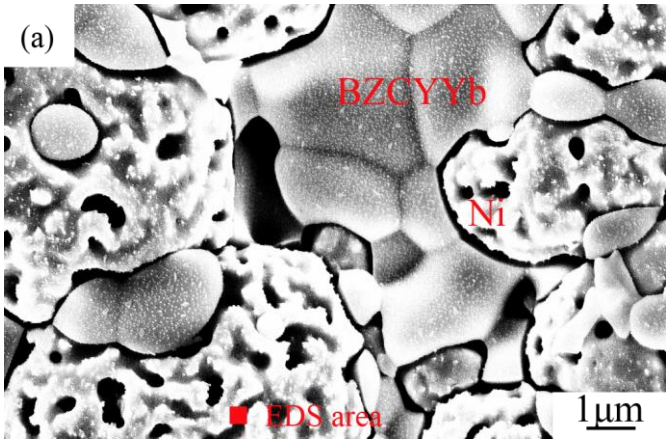

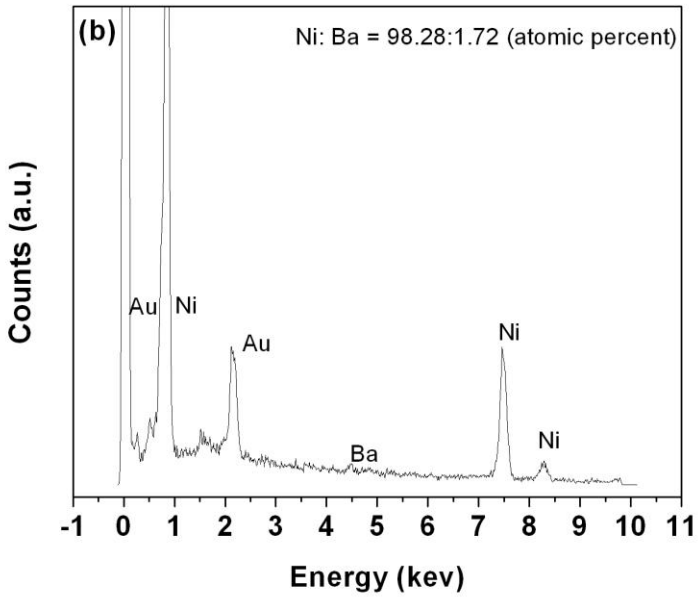

Figure 4-12 (a) Surface morphology of Ni-BZCYYb anode in a cell with a configuration of Ni-BZCYYb | YSZ | LSCF (b) A typical EDS spectrum collected from the Ni grain area in a Ni-BZCYYb composite anode. (The spectrum also shows Au, which is from the Au coating on the sample surface to minimize charging during SEM analysis).

Figure 4-13 shows the X-ray photoelectron spectrum (XPS) of the Ni surface after reduction of NiO which was co-fired with BZCYYb at 1400 oC for 5h. It is clearly seen that Ba was predominantly present on the Ni surface with a small amount of Ce. No other elements such as Zr, Y and Yb from BZCYYb were found on the Ni surface. The spreading of elements is attributed primarily to the evaporation of barium and cerium from the BZCYYb phase during sintering at high temperature. The barium evaporation in BZCYYb is consistent with the common observations in barium cerate and zirconate based materials that invariably experienced deficiency in barium site after high-temperature calcinations because of the volatility of barium [61]. The modification of NiO can be also intuitively observed by the black color of NiO-BZCYYb anode support

since the traditional NiO-YSZ and NiO-SDC anode supports are normally green. From the phase diagram of BaO-NiO system, a new compound BaNiO2 that appears black instead of the green color for NiO forms when the temperature is increased over 1100 ^{o}C [62]. Upon the treatment in humidified H_2, NiO was reduced into Ni while barium and cerium still existed as oxide forms. The Ni particles adjacent to BZCYYb were then modified by barium oxide and ceria.

To identify the distribution of these oxides on the modified Ni surface, a scanning auger nanoprobe (SAN) was used. The mole ratios of Ni, Ba and Ce in a typical oxide island and in a blank area between two islands are 11.5: 16.3: 1.0 and 29.5: 3.7: 1.0, respectively, indicating that barium oxide was predominant in the islands and oxides only partially covered the Ni surface. Thus, barium oxide and ceria were distributed in the form of islands on the Ni surface with the average size of several hundred nanometers. In the catalytic reforming of hydrocarbons, BaO or other alkaline earth oxides have been commonly used as promoters[63]. The retardation of carbon deposition in the presence of these additives is ascribed to either promotion of dissociation of H_2O or repulsion effect between the cracked hydrocarbon fragments resulting from the electron donor characteristic of the alkali [64]. There are several analogies between heterogeneous catalysis at Ni and our study [65]. In the presence of oxygen ions from the cathode under fuel cell operating conditions, the carbon deposition might be also mitigated when the BaO is deposited on the Ni anode. Considering the slight barium loss in the A-site of BZCYYb perovskite and resultant low BaO vapor pressure, the thickness of island should be extremely thin. Therefore, while barium oxide and ceria are electronic insulators, the distribution of these thin oxide islands shown in figure 1b might not adversely affect the electronic properties of Ni and thus the modified Ni could display high electro-catalytic activity as well as excellent tolerance to coking.

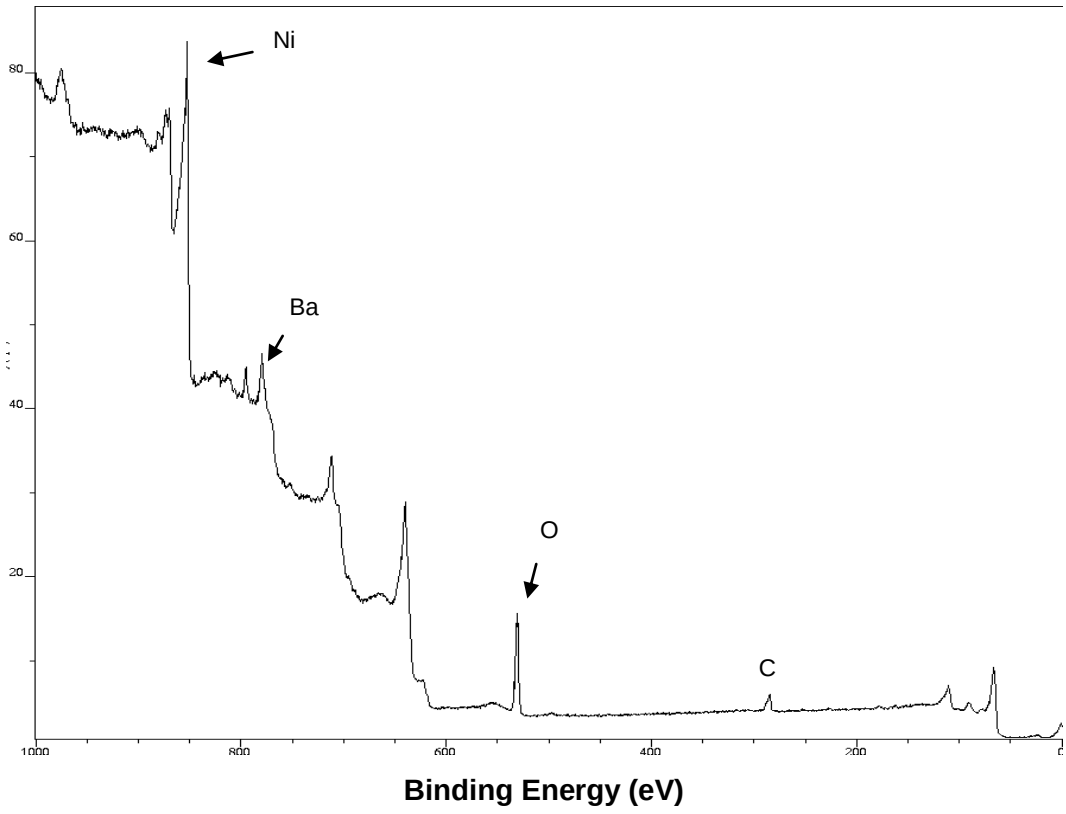

Figure 4-13 A typical XPS spectrum collected from a modified Ni grain surface. The spectrum also shows oxygen (due to rapid oxidation of Ni in air) and trace amounts of carbon (due to surface adsorption of CO_2 from the air) on the surface because the sample was exposed to air as it was transferred from the furnace to the XPS chamber (but was never exposed to hydrocarbon).

In-situ Raman spectroscopy, which is very sensitive to trace amounts of carbon (it may not be observable under SEM examination), was employed to probe and map the presence of any carbon on a large area of a Ni surface during exposure to C_3H_8 at high temperatures. Shown in figure 4-14 are some typical *in-situ* Raman spectra acquired from Ni pellets with and without contamination by BZCYYb in dry and humidified (~3 v% H_2O) C_3H_8 at 600 ^oC using a custom-made environmental chamber. Obviously, the

spectra for unmodified Ni display two features associated with the formation of graphitic carbon. The vibrational band near 1580 cm^{-1} arises from extended domains of highly ordered graphite while the band near 1340 cm^{-1} is broader and corresponds to tetrahedral carbon defects within a graphite lattice[66]. Furthermore, it was observed that the introduction of ~3% steam to C_3H_8 reduced the band intensity of ordered graphite on unmodified Ni; in this case, the 1580 cm^{-1} mode is more susceptible to the reaction with water. However, these features for carbon deposits are still very strong. In contrast, exposure of modified Ni in humidified C_3H_8 led to no measurable Raman signal, suggesting a lack of detectable carbon deposits on the surfaces. The enhanced coking tolerance of modified Ni reveals that carbon chemistry was dramatically changed by the nanostructured layers, which might readily adsorb water and facilitate water-mediated carbon removal reactions. We previously proposed that the distinct ability of BZCYYb to supply as well as take up water greatly facilitates *in-situ* reforming of carbon-containing fuels in the Ni-BZCYYb anode. It is easily expected that the adsorbed water on BZCYYb could remove the carbon around the three-phase boundary. The presence of these oxide islands would further prevent carbon formation on the Ni sites away from TPB. The high tolerance of the modified Ni electrocatalyst well explained the observed steady electrochemical performances of the Ni-BZCYYb anodes in C_3H_8 fuel.

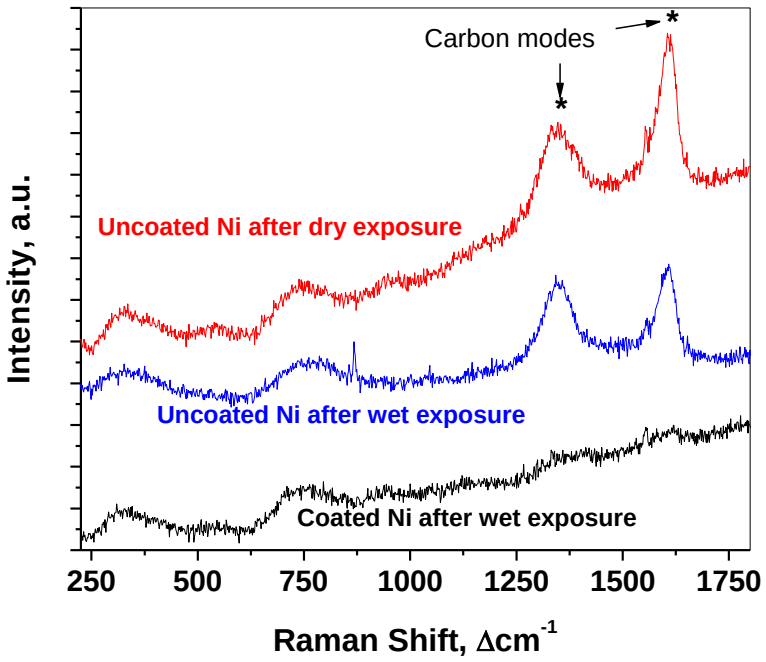

Figure 4-14 Raman spectra collected from Ni pellets with and without "contamination" by BZCYYb after exposure to dry and wet C_3H_8 at 600°C for 3 hours under open circuit voltage (OCV) condition.

4.6 Summary

A properly doped zirconate-cerate exhibits the highest ionic conductivity at low temperatures and is strikingly effective in direct utilization of H_2S-contaminated fuels and hydrocarbons in the absence of excess steam. The desirable catalytic properties are attributed to its distinctive ability to adsorb water on the surface that greatly facilitates the removal of H_2S and *in situ* reforming of carbon-containing fuels. Furthermore, the nanostructured oxide islands on Ni from dispersion of BZCYYb phase during high-temperature calcinations effectively suppress the formation of coking from dehydrogenation of C_3H_8. Thus, Ni-BZCYYb has great potential to dramatically improve the economical competitiveness and commercial viability of SOFCs that are driven by cost-effective and renewable fuels. In addition, the material may also be used as catalysts

for reforming of hydrocarbon fuels and for removal of fuel gas contaminants such as sulfur.

CHAPTER 5

SIMPLE SURFACE MODIFICATION OF NI-YSZ ANODE

5.1 Experimental

5.1.1 Fabrication of fuel cells

The button-type cells with a configuration of Ni-YSZ |YSZ| SDC/LSCF were fabricated in steps described as follows. First, an anode support with mixed NiO (Sigma-Aldrich) and YSZ powders (TOSOH Co.) (weight ratio of 55:45) was fabricated by tape casting (~0.6 mm thick and 13 mm in diameter), followed by pre-firing at 800^{o}C for 2 h. Second, a thin layer of YSZ (~15 μm) was deposited on the anode support by a solution coating process followed by co-firing at 1400^{o}C for 5 h. Third, a $Sm_{0.1}Ce_{0.9}O_{2-\delta}$ (SDC, synthesized by a chemical co-precipitation process) buffer layer (~2 μm) was screen-painted on YSZ surface and fired at 1200^{o}C for 2 h. Fourth, an LSCF (Fuel Cell Materials) slurry was screen printed onto the top of the SDC layer and fired at 1050^{o}C for 2 h to form a porous cathode (~30 μm thick) with an active area of 0.28/cm^{2}. BaO was introduced into the NiO-YSZ structure by evaporation deposition during the firing of the SDC buffer layer. To accomplish this, ~30 mg BaO powder (Sigma-Aldrich) was placed underneath a co-fired NiO-YSZ|YSZ bilayer with the anode facing the BaO powder (but without physical contact) and the top surface of YSZ covered by a green SDC buffer layer; they were then fired at 1200^{o}C for 2 h. During this process, BaO vapor reacts with NiO, producing a thin layer of NiO-BaO compounds on the NiO surface. Upon exposure to a fuel, the thin film of NiO-BaO compounds is reduced to BaO nano-islands distributed on the Ni surface, creating nanostructured BaO/Ni interfaces.

5.1.2 Electrochemical measurements

First, Ag/Pt paste and Ag/Pt wire were applied to both the anode and cathode sides for current collection. Then, each button cell was sealed on an alumina tube and

heated to 750^{o}C in ambient air, followed by reduction of anode in H_2. For evaluation of performance based on wet CO or dry C_3H_8 fuels, the cells were conditioned in H_2 to enter steady state before the fuel was switched to wet CO or dry C_3H_8. Both flow rates were 10 mL/min and the fuel utilization was about ~5%. The wet CO was passed through a water bubbler at room temperature, yielding ~3 v% water vapor. For carbon fuel, we integrated a fluidized bed gasifier with a fuel cell. K_2CO_3 was used as a catalyst to enhance the gasification rate and reduce the reaction temperature. The catalyst loading was ~0.0024 mol K^+ per gram of activated C. First, 0.884 g K_2CO_3 (Sigma-Aldrich) was dissolved into 50 ml de-ionized water. Second, 5 g activated carbon (Norit DLC Supra 30) was added to the solution under stirring for 24 h, followed by drying in an oven at 80ºC. Third, 0.4 g carbon mixture was put into the testing fixtures such that intimate contact with the anode surface was achieved. When the operating temperature was reached, wet CO_2 (~3 v% H_2O) was fed into the system after reduction of the anode in H_2. All standard electrochemical experiments were performed using a Solartron 1286 electrochemical interface and a Solartron 1255 HF frequency response analyzer. The long-term electrochemical performances of test cells were acquired using an Arbin fuel cell testing system (MSTAT).

5.1.3 Other characterizations

To characterize the structure, composition, and morphology of the BaO islands and BaO/Ni interfaces, we employed synchrotron-enabled X-ray diffraction and absorption spectroscopy, as well as advanced electron microscopy and spectroscopy (STEM, HRTEM, SEM and EDS). First, dense NiO pellets were fabricated by dry pressing and sintering at 1450 ºC for 5 h. Then, the surface of the NiO pellet were exposed to BaO vapor at 1200 ºC for 2 h, as described earlier for fabrication of full cell anodes. The BaO/NiO sample was then reduced in dry H_2 at 750 ºC for 1h, again, similar to the procedures used for fuel cell preparation and testing. The surface of BaO/NiO

pellets after reduction was first analyzed with a LEO 1530 field emission SEM/EDS operated at 15 kV. The TEM samples were prepared with the method of Focused Ion Beam (FIB) in-situ lift-out. A thin layer contained tungsten was applied on the BaO/Ni surface before FIB lift-out and thus would form a strong mass-contrast with the BaO island. The FIB was carried out with a Hitachi NB5000 FIB-SEM operated at 40 kV. The cut sample was examined in an HF3300 TEM/STEM/EDS equipped with a field emission gun and operated at 300 kV. STEM and EDS were conducted with an electron probe of a size of about 3Å. The grazing incidence angle thin film X-ray diffraction analysis was carried out at beamline X14A of the National Synchrotron Light Source (NSLS) at Brookhaven National Laboratory using a six circle Huber diffractometer and a Si strip detector. Barium L_{III}-edge XANES data were collected at beamline X18A of the NSLS using the fluorescence detection mode, and the data were processed using the Athena and Artemis software packages. Thermogravimetric analysis was performed using a TA Q600 DSC-TGA system. Before comparing the water uptake ability, powders of Ni, BaO and YSZ were first heated to 1000 ^{o}C and held for 4 hours under dry argon with 4 v% H_2 to remove water and possible surface carbon dioxide. As for the Raman measurements, the BaO/NiO and pure NiO samples were reduced in dry H_2 gas at 500°C for 2 hours using a custom-made environmental chamber. Raman spectra were then obtained in dry/wet H_2 using a Renishaw 1000 Raman spectromicroscopy system with a 514 nm excitation wavelength. The spot size was ~5 μm in diameter.

5.1.4 Computational methods

Density functional theory (DFT) calculations with the projector-augmented wave (PAW) method were carried out using the Vienna *ab initio* simulation package (VASP). The spin-polarization calculation was applied due to the magnetic properties of Ni. While the generalized gradient approximation (GGA) with the Perdew-Wang exchange-correlation functional was used, the kinetic energy cutoff for a plane wave basis set was

400 eV. In order to allow convergence to 0.01 eV of the total electronic energy, the Brillouin zone was sampled with the (3 × 3 × 3) and (3 × 3 × 1) Monkhorst-Pack mesh **k**-points for bulk and surface calculations. For the 2-D slab model calculations, surfaces were separated by a vacuum space of 15 Å in the direction perpendicular to the surface. The climbing image nudged elastic band (CI-NEB) method was applied to locate transition states, and potential energy surfaces (PESs) were constructed accordingly. The adsorption energy (E_{ad}) reported in the study was calculated as follows.

E_{ads} = E[adsorbate-surface] – E[surface] – E[adsorbate]

where E[adsorbate-surface], E[surface], and E[adsorbate] are the predicted electronic energies for an adsorbed species on a surface, a bare surface, and a gas-phase species such as H_2O.

5.2 Microanalysis of BaO nanoislands and BaO/Ni interfaces

To characterize the detailed structure and composition of the surfaces in this new anode, we used synchrotron-based X-ray analyses because the nanostructured surface layers were very thin and undetectable using conventional X-ray analysis. Since carbon forms much more readily on Ni than on YSZ [63], BaO/Ni interfaces are more important than BaO/YSZ interfaces for carbon removal. Figure 5-1 shows typical grazing incidence angle X-ray diffraction patterns collected from the surface of BaO/NiO samples before and after reduction in H_2. Before reduction, the main phase was cubic polycrystalline NiO, but extremely weak diffraction peaks related to $BaNiO_2$ and $BaNiO_3$ on the NiO surface were also observable, indicating the presence of these two phases in very low quantity. This is consistent with the known phases in the BaO-NiO system. After reduction in H_2, however, only metallic Ni was detected. No diffraction peaks related to any compounds in the Ba-Ni-O system could be detected even with extended X-ray exposure, suggesting that any Ba-containing phases were lacking long-range order.

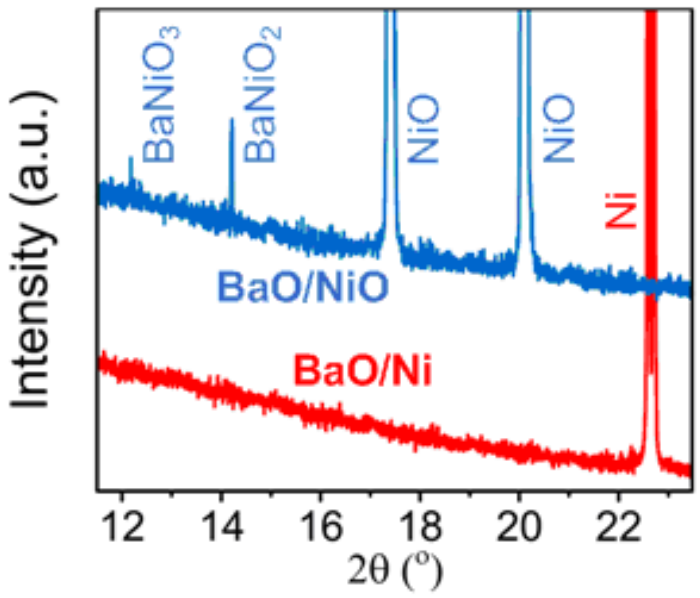

Figure 5-1 Grazing incidence angle XRD patterns of BaO/NiO samples before and after reduction in hydrogen. These patterns were collected at X14A beamline of National Synchrotron Light Source (NSLS). The incident angle was 0.1° and the wavelength λ was 0.72838 Å.

The Ba L_{III} edge X-ray absorption near-edge structure (XANES) analysis (Figure 5-2) showed that Ba was indeed still present on the Ni surface in compound form, not as Ba metal, suggesting presence of BaO clusters or islands on the Ni surface.

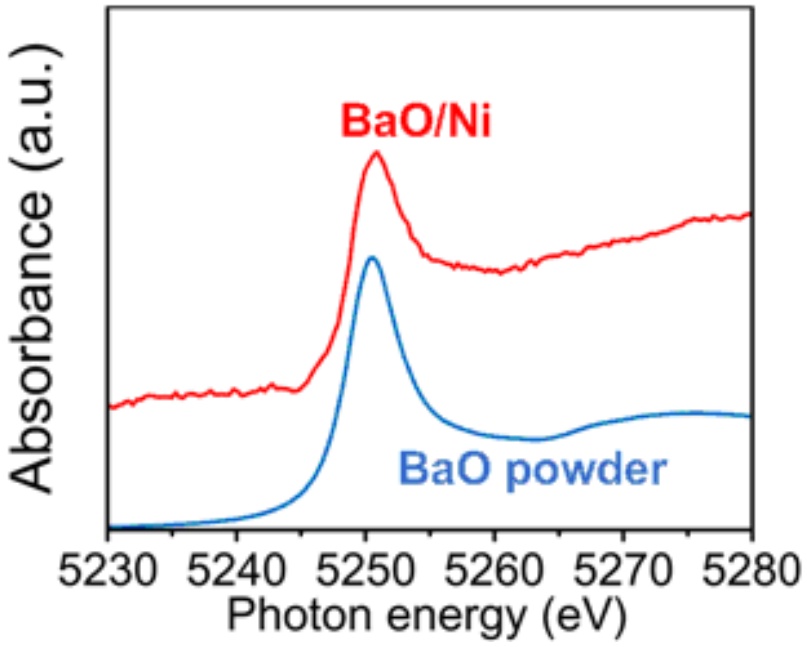

Figure 5-2 Ba L_{III} edge XANES spectra of BaO powder and BaO/Ni sample. The XANES spectra were collected at X18A beamline of NSLS using reflective detection mode. The Ba L_{III} edge XANES spectrum of BaO/Ni was an average of 13 spectra.

To reveal the local microstructures and morphologies of the nano-sized BaO islands and the BaO/Ni interfaces, we used electron microscopy and spectroscopy. An SEM examination revealed that BaO nano-islands were uniformly distributed on the Ni surface (Fig.5-3b); the presence of Ba and O in the islands was confirmed by energy dispersive spectroscopy (EDS). The island sizes varied from a few nm to over 100 nm, and the distances between two neighboring BaO islands were on the order of 10 to 100 nm. A cross-sectional view (Figure 5-3a) and a Z-contrast image (Figure 5-4a) of a BaO/Ni interface indicated that the thickness of the BaO island was up to ~30 nm. Also, Z-contrast imaging coupled with simultaneous EDS (Figure 5-4b) was performed to confirm the presence of Ba and O in the island with a nano-probe (FWHM ~3Å).

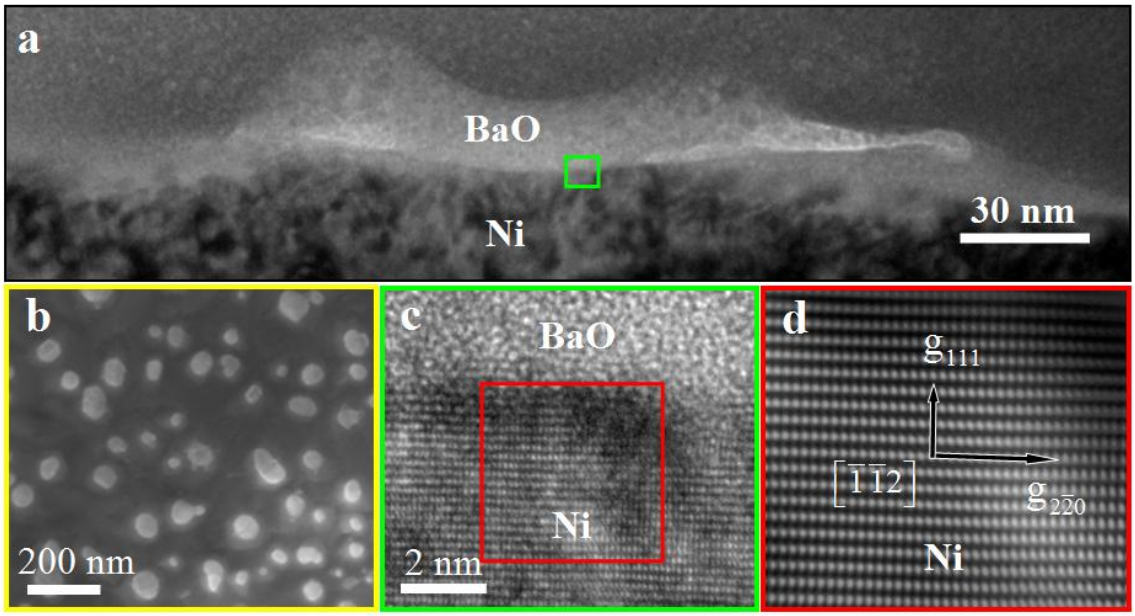

Figure 5-3 (a) Cross-sectional view (bright-field TEM image) of a BaO/Ni interface. (b) Top view (SEM image) of a BaO/Ni sample. (c) HRTEM image of the BaO/Ni interface. The $[\bar{1}\bar{1}2]$ zone axis of the Ni under the BaO island is along the viewing direction. (d) Fourier-filtered $[\bar{1}\bar{1}2]$ zone axis image of the Ni under the BaO island.

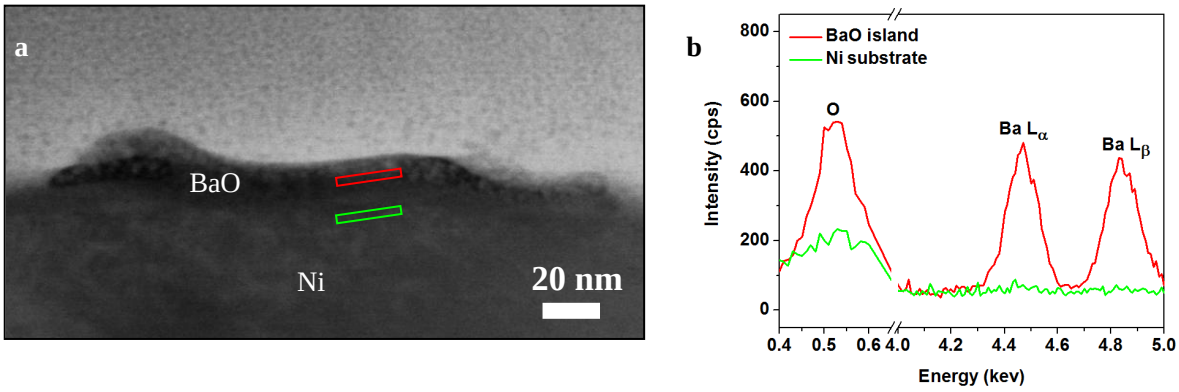

Figure 5-4 Z-contrast image (a) of a BaO/Ni interface and EDS spectra (b) acquired from the BaO island and the underlying Ni. The EDS spectra were acquired from the rectangular areas marked in (a).

A selected area electron diffraction (SAED) pattern, taken from the BaO island on the Ni surface (Figure 5-5), consisted of characteristic Ni spots and a diffuse ring, which again suggests that the BaO island lacks long-range order. This is also consistent with the XRD spectrum acquired from the same sample (Fig. 5-2). A high-resolution TEM (HRTEM) image of the interface (Fig. 5-3c) clearly resolved the (111) and $(2\,\bar{2}\,0)$ lattice fringes along the $[\,\bar{1}\,\bar{1}\,2]$ zone axis of the Ni under the BaO island. It also revealed the amorphous appearance of the BaO island on the Ni surface. The Ni $[\,\bar{1}\,\bar{1}\,2]$ zone-axis image and amorphous appearance of the BaO island are consistent with the selected area electron diffraction (SAED) pattern (Figure 5-5). To highlight the zone-axis fringes of the underlying Ni grain, a Fourier-filtered image of the rectangular area marked in the image (Figure 5-3c) is presented in Figure 5-3d. A solid sphere model of the fcc lattice structure of Ni viewed along the $[\,\bar{1}\,\bar{1}\,2]$ direction is shown in Figure 5-6**,** where correlation between the model and HRTEM imaging is illustrated.

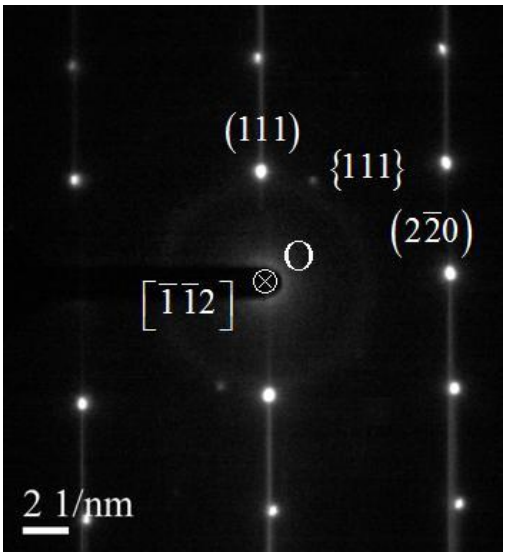

Figure 5-5 Selected area electron diffraction (SAED) pattern of the stack of Ni/BaO island/part of the tungsten coating. The Miller indices and crystallographic direction labeled are those of Ni.

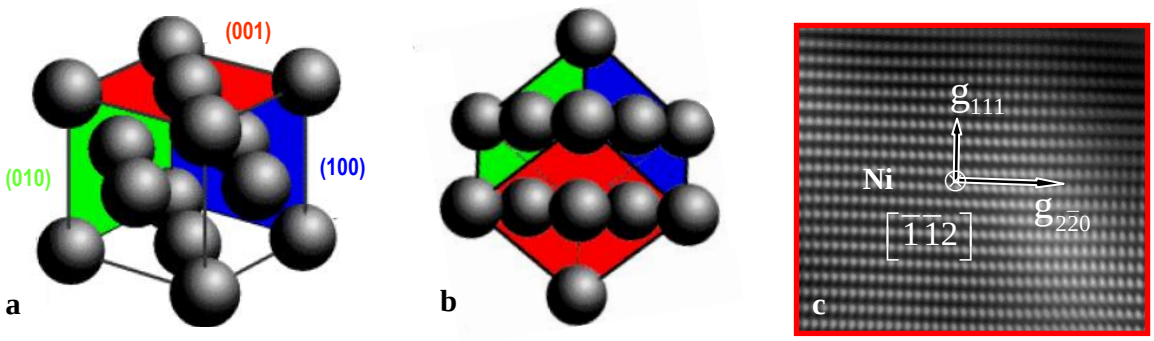

Figure 5-6 Ball models of an fcc lattice in perspective view (a) and seen along the $[\bar{1}\bar{1}2]$ zone axis (b), and the Fourier-filtered image of the Ni immediately under the BaO island (c). The Miller indices in (a) denote the lattice planes, with each pair of indices and plane assigned the same color.

These analyses have shown that BaO nano-islands were formed on Ni by vapor deposition and subsequent reduction, creating a thin, nanostructured surface layer consisting of numerous BaO/Ni interfaces. Unlike the carbon-tolerant Sn-Ni catalyst [67] that requires full coverage of Ni by surface alloy to be effective, alkaline oxides [68] were reported to effectively diminish the tendency of carbon buildup by partial coverage of Ni surfaces. Also, our DFT calculations predict that the electronic properties (e.g, the d-band center) of Ni are not adversely affected by the deposition of the BaO in the model with a small BaO chain (3 Ba and 3 O atoms) over a three-layer p(3 × 5) Ni substrate

(Figure 5-7).

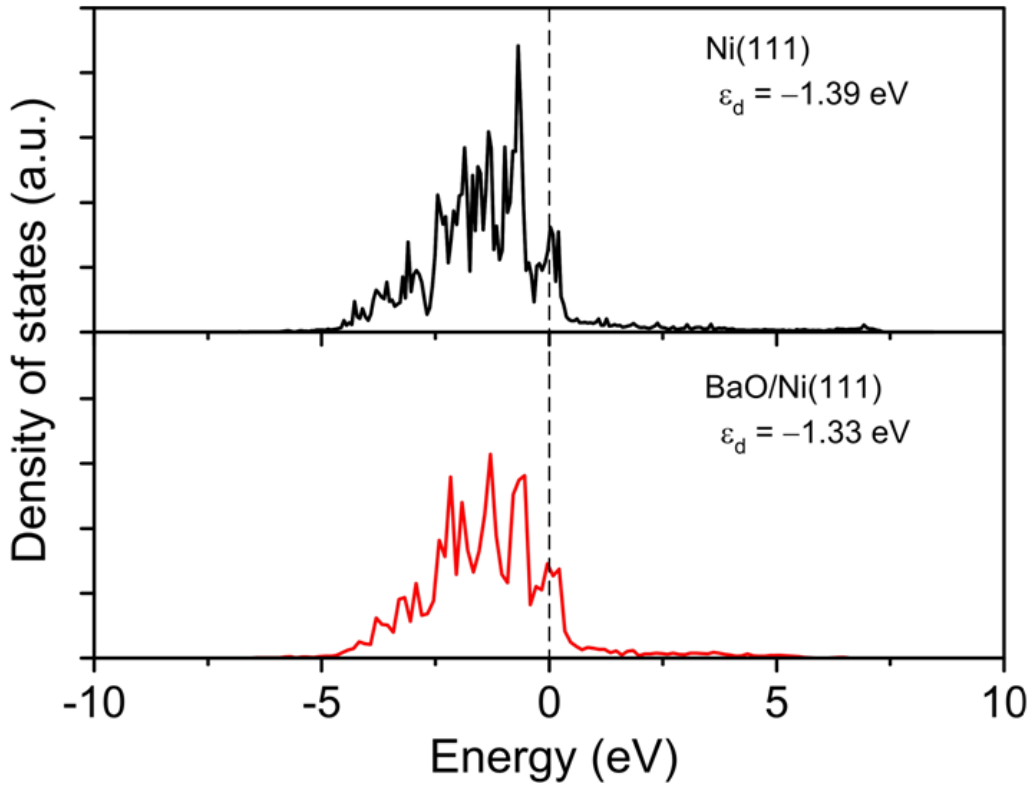

Figure 5-7 Projected density of states of Ni(111) and BaO/Ni(111) using DFT. The vertical dashed line is the Fermi level. The values in the figure are predicted d-band centers based on only the seven bare Ni atoms on the top most Ni layer.

This is further corroborated by experimental results; the power output of a cell with this new anode in H_2 is similar to those of a cell with a conventional Ni-YSZ anode (Figure 5-8) under the same testing conditions, suggesting that the nano-islands of BaO on the Ni surface do not hinder the charge transfer on the anode. When the fuel was switched from H_2 to C_3H_8, CO or gasified carbon, however, the cell with this new anode displayed much higher and more stable power density than that with a conventional Ni-YSZ anode.

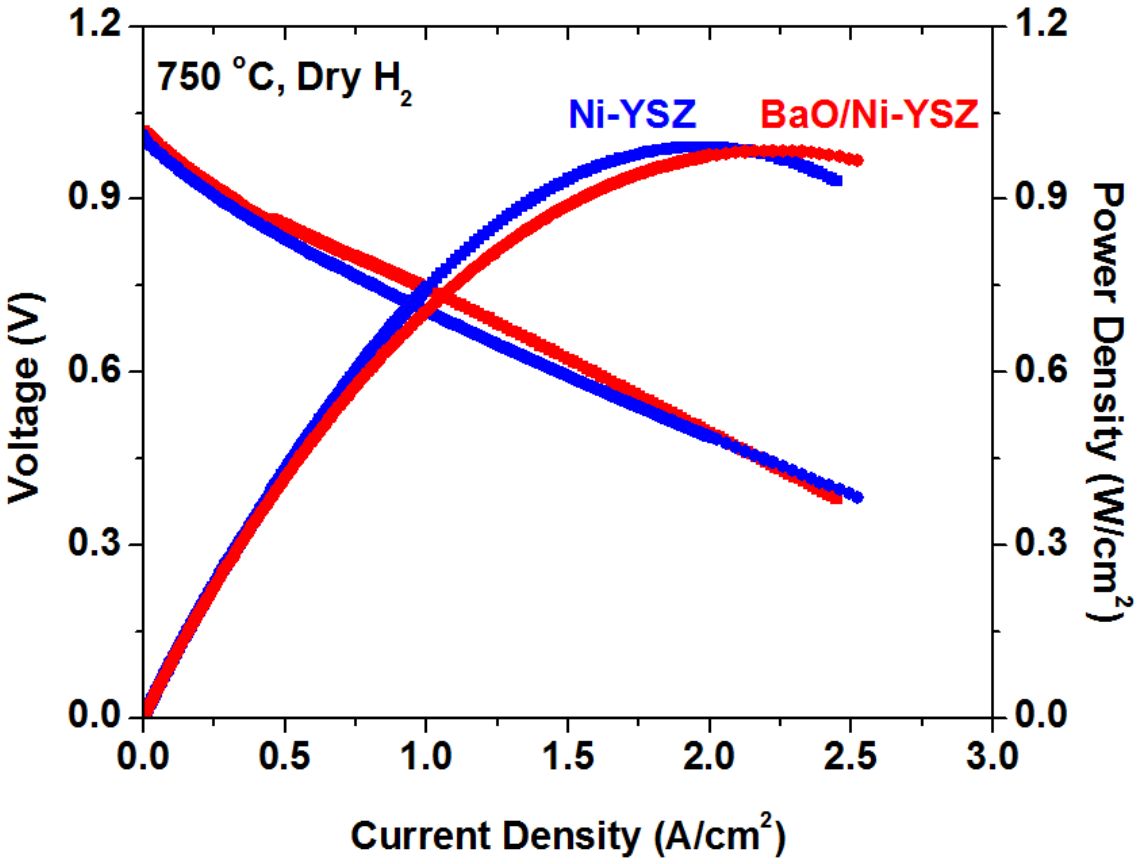

Figure 5-8 Typical current-voltage characteristics and the corresponding power densities measured at 750°C for cells with configurations of BaO/Ni-YSZ |YSZ| SDC/LSCF and Ni-YSZ |YSZ| SDC/LSCF when dry hydrogen was used as fuel and ambient air as oxidant.

5.3 Performance of modified cells in C_3H_8

To examine the electro-catalytic activity of the anode with nanostructured BaO/Ni interfaces toward hydrocarbon fuels, we investigated the current-voltage characteristics and measured the corresponding power densities of cells consisting of such an anode, a YSZ electrolyte, an $Sm_{0.1}Ce_{0.9}O_{2-\delta}$ (SDC) buffer layer and an $La_{0.6}Sr_{0.4}Co_{0.2}Fe_{0.8}O_{3-\delta}$ (LSCF) cathode operated with dry C_3H_8. Figure 5-9 shows a typical peak power density of ~0.88 W/cm^2 at 750 °C when dry C_3H_8 was used as the fuel, much higher than ~0.5 W/cm^2 at 750°C reported for the latest SOFCs operated under similar conditions[69]. The

power output is also higher than those in the recent literatures related to the alkaline oxide-modified anodes [24-26], namely ~0.30 W/cm^2 at 750ºC in CH_4 (While the performances for these cells in C_3H_8 were not reported, they should be lower than the power densities in CH_4 because of more carbon atoms [69]).

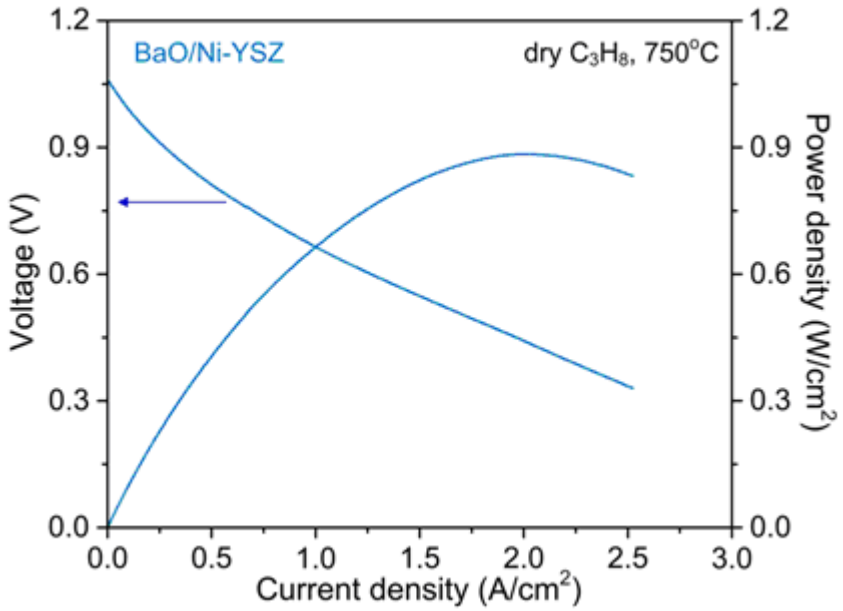

Figure 5-9 Typical current-voltage characteristics and the corresponding power densities measured at 750ºC for cells with a configuration of BaO/Ni-YSZ |YSZ| SDC/LSCF when dry C_3H_8 was used as the fuel and ambient air as the oxidant.

Further, the cell displayed stable power output for more than 100 hours at a constant current density of 500 mA/cm^2, suggesting that the carbon deposit was largely absent on the anode although the carbon deposition on the cell mounting tube walls can not be avoided. In contrast, the performance of the cell with a conventional Ni-YSZ anode, tested under identical operating conditions, dropped rapidly in dry C_3H_8, due primarily to carbon buildup and deactivation of the anode (Figure 5-10).

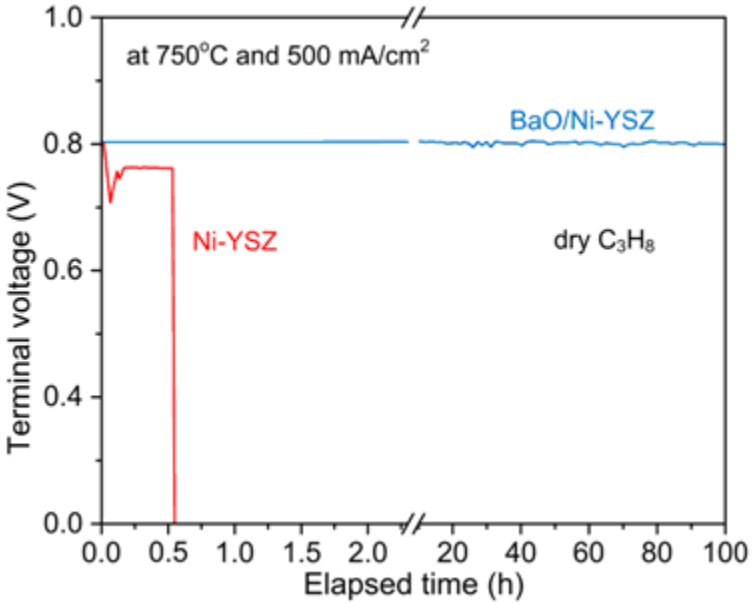

Figure 5-10 Terminal voltages measured at 750ºC as a function of time for the cells with and without BaO/Ni interfaces operated at a constant current density of 500 mA/cm^2 with dry C_3H_8 as the fuel. Water was formed on the anode by electrochemical oxidation of dry C_3H_8.

Subsequent SEM inspection of the Ni-YSZ anodes with and without BaO/Ni interfaces showed that minimal carbon deposition occurred on the modified anode while the heavy disintegration of Ni-YSZ anode induced by carbon deposits was developed during the course of fuel cell operation (Figure 5-11). Figure 5-11a shows a cross-sectional view of a typical fuel cell (as fabricated) with a BaO/Ni-YSZ anode, a YSZ electrolyte, an SDC buffer layer and an LSCF cathode. The YSZ electrolyte is ~15 µm thick. To avoid formation of insulating phases between the YSZ and LSCF cathode, an SDC buffer layer (~2 µm thick) was applied to the YSZ before application of the LSCF cathode. SEM images of the BaO/Ni-YSZ anode before and after operation (Figures 5-11c and 5-11d) at 750ºC in C_3H_8 and gasified C show no observable carbon deposits blocking the pores.

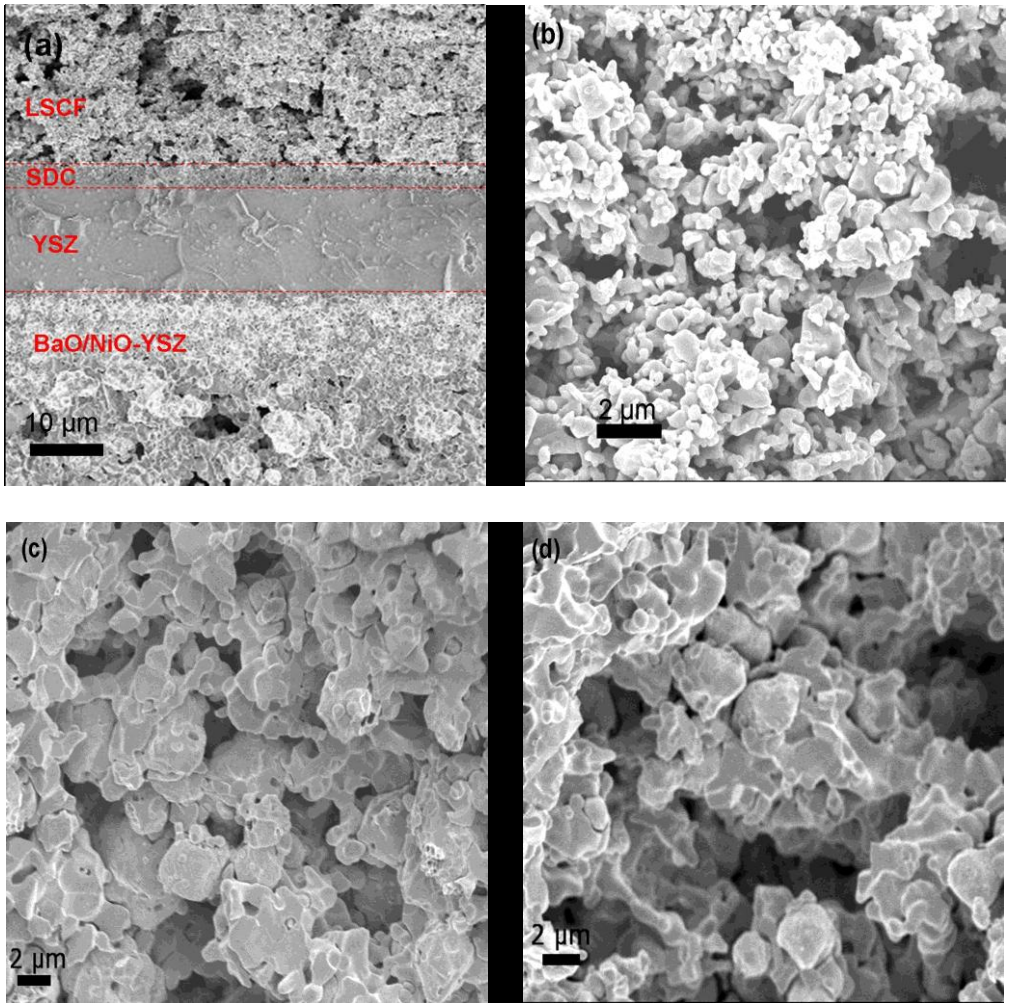

Figure 5-11 (a) A cross-sectional view (SEM image) of a cell with a configuration of BaO/Ni-YSZ |YSZ| SDC/LSCF (before NiO was reduced to Ni); (b) LSCF cathode; the BaO/Ni-YSZ anode before operation (c) and after operation (d) in C_3H_8 and gasified carbon at 750ºC.

It is noted that water was produced on the anode from fuel cell operation although dry C_3H_8 was fed into the cell. The observed stable power outputs of the cell with this new anode in dry C_3H_8 at a current density of 500 mA/cm^2 is attributed primarily to the formed water on the anode which promoted carbon removal near the BaO/Ni interfaces.

5.4 Performance of modified cells in CO and gasified carbon fuels

To inspect the behavior of this new anode in CO and its tolerance to coking due to the CO disproportionation reaction, we fed CO fuel to test cells. Figure 5-12 shows the terminal voltage of a cell with such an anode operated at a constant current density of 500 mA/cm^2 at 750ºC as a function of time when wet CO was used as fuel, demonstrating a steady performance up to more than 100 hours. This cell also displayed very stable OCV, indicating again that the presence of ~3v% water is sufficient to avoid carbon buildup on the anode under OCV conditions.

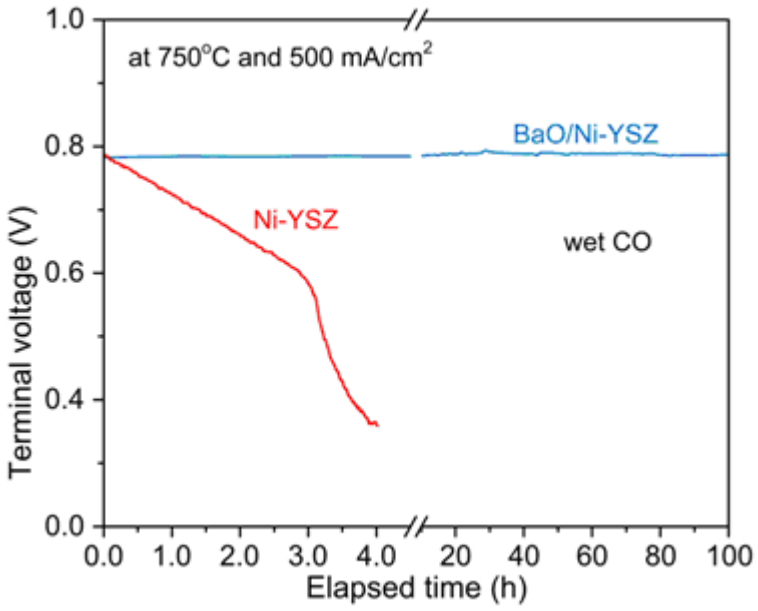

Figure 5-12 Terminal voltages measured at 750ºC as a function of time for the cells with and without BaO/Ni interfaces operated at a constant current density of 500 mA/cm^2 with wet CO (with ~3 v% H_2O) as the fuel.

Furthermore, this cell displayed a peak power density of ~0.70 W/cm^2 at 750 ^{o}C in CO (Figure 5-13), representing the highest ever reported under the testing conditions and demonstrating much-improved tolerance to coking at low temperatures (a more

severe condition for carbon buildup on Ni due to the CO disproportionation reaction). In contrast, a conventional Ni-YSZ anode was deactivated quickly in wet CO at 750 ºC and the peak power density was only ~0.2 W/cm^2 after 4 h operation (Figure 5-13), although it can indeed be operated at the temperatures higher than 850^{o}C. As the operating temperature is lowered, however, much less expensive materials may be used for cell components to considerably reduce the cost while improving the reliability and operational life of fuel cells, making them more commercially viable. The demonstrated coking tolerance and high performance in CO at lower temperatures therefore advance the possibility for efficient conversion of gasified coal or other carbonaceous solid fuels to electricity.

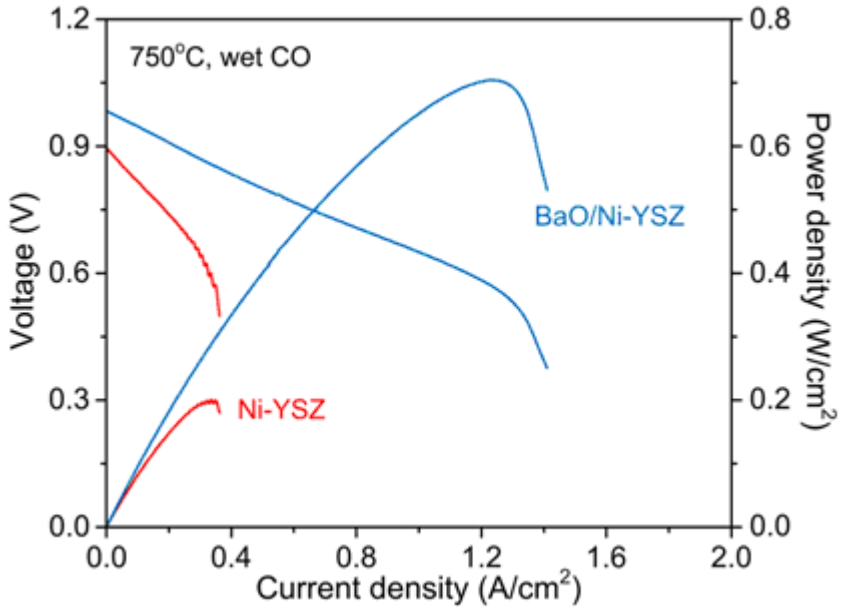

Figure 5-13 Typical current-voltage characteristics and the corresponding power densities measured at 750ºC for cells with and without BaO/Ni interfaces (after 4 h operation) when wet CO was used as the fuel and ambient air as the oxidant.

To evaluate the feasibility of using gasified solid carbonaceous fuels, we used a fluidized carbon bed-SOFC arrangement (Figure 5-14). Figure 5-14a shows

schematically the configuration of a SOFC using gasified carbon in this study. It consists of an integrated fluidized bed gasifier and a single cell. Also, we investigated a design with an external gasifier coupled with a fuel cell to understand the fundamental issues (similar to a previous study by Gür et al[31]), as shown in Figure 5-14b. In these systems, carbon was gasified in a fluidized bed by CO_2 to CO, which was then electrochemically oxidized to CO_2 on the BaO/Ni-YSZ anode. Recycling 50% of the exhaust CO_2 back to the fluidized bed allows more efficient recovery of the waste heat of the product stream and enhances system efficiency. With the configuration in Figure S6*B*, a fuel cell also produced a similar power output at 750^{o}C (without any carbon deposition) and the fuel utilization was about ~5%. This low fuel utilization represents a very severe condition for carbon deposition since the tendency for carbon deposition decreases with the increase in fuel utilization. If the anode displays sufficient tolerance to coking under this condition, it should not experience carbon buildup at higher fuel utilization when more oxidation products (CO_2 and H_2O) are produced in the anodic compartment.

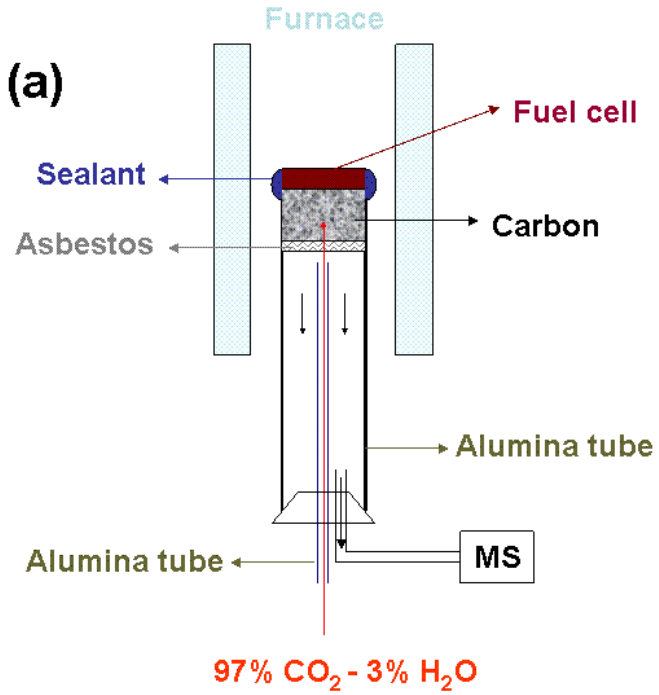

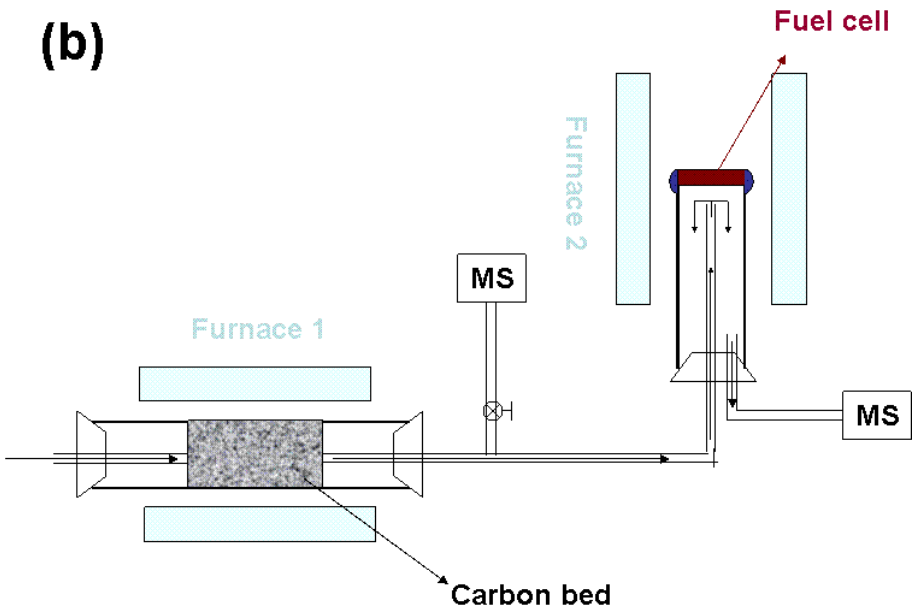

Figure 5-14 Schematic depictions of our testing systems with an integrated fluidized-bed gasifier (a) and an external fluidized-bed coupled to a fuel cell (b).

Analysis of the effluent gas using mass spectrometry indicated that carbon was converted primarily to CO (~96%), with small amounts of H_2, H_2O, CO_2, and CH_4 through wet (~3 v% water vapor) CO_2 gasification (Figure 5-15).

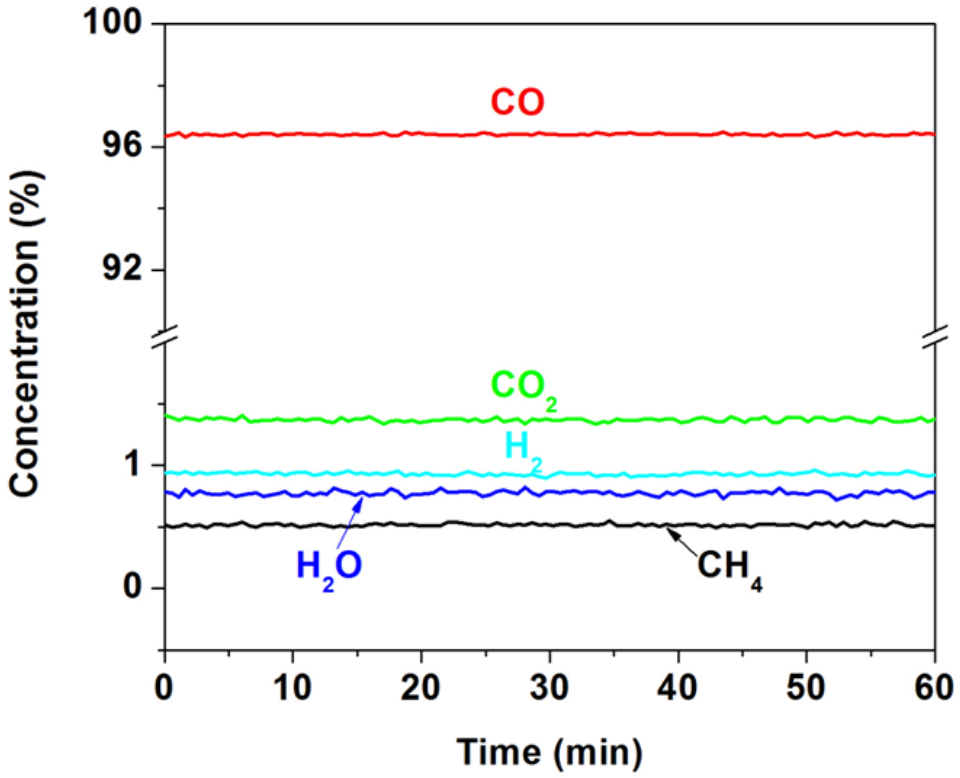

Figure 5-15 A typical concentration profile of the outlet gas mixture from the gasifier monitored using a mass spectrometer.

The fuel cell with the new anode and gasified carbon as fuel in this configuration demonstrated a peak power density of ~1.08 W/cm^2 at 850ºC (Figure 5-16), about twice that of a cell with a conventional Ni-YSZ anode under the same conditions (~0.52 W/cm^2) and the latest cell using gasified coal with CO_2 gasification (~0.45 W/cm^2 at 850ºC) [70].

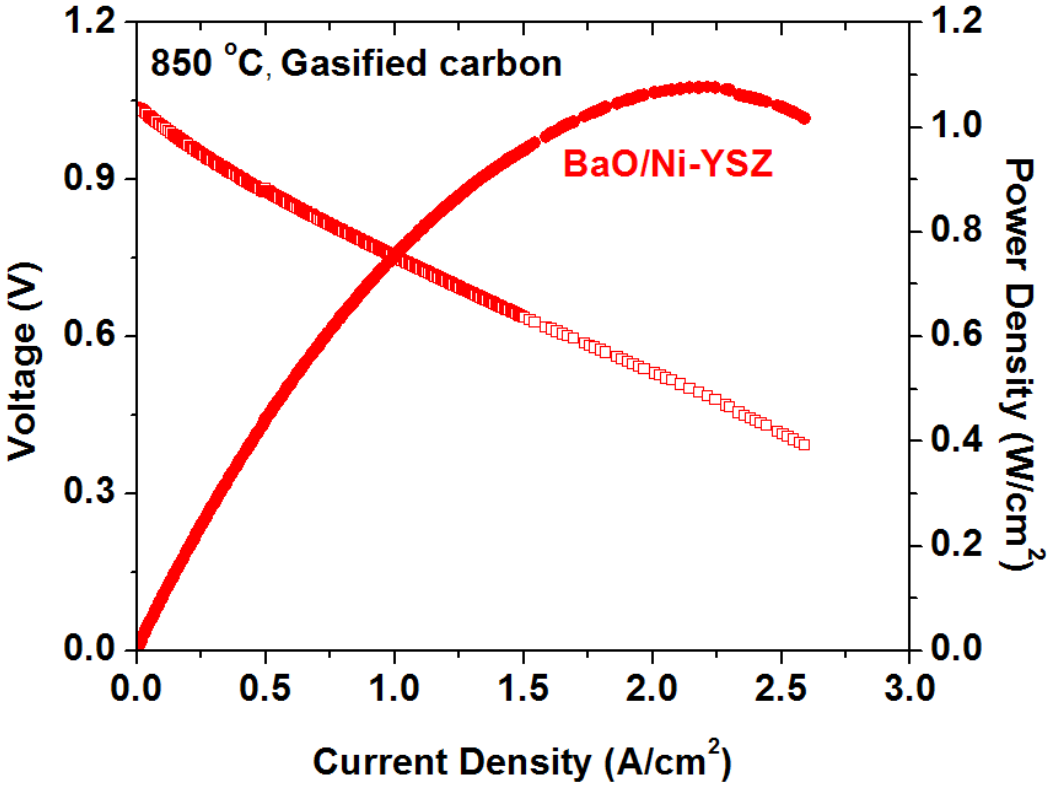

Figure 5-16 Typical current-voltage characteristics and the corresponding power densities measured at 850°C for a cell with a configuration of BaO/Ni-YSZ |YSZ| SDC/LSCF when gasified carbon was used as fuel and ambient air as oxidant.

More importantly, when the operating temperature was reduced to 750°C, the fuel cell with the new anode still displayed a stable power output and reached a peak power density of ~0.65 W/cm^2 (Figure 5-17). In contrast, a conventional Ni-YSZ anode cannot be stably operated in gasified carbon at this temperature, which is consistent with the observed behavior of the same cell when CO was used as the fuel. While it is possible to avoid coking on conventional Ni-YSZ anodes by gasification with sufficient H_2O and CO_2 (to produce H_2-rich syngas or CO_2-rich gas), the amounts of H_2O and CO_2 required are often excessive, greatly diluting the fuel and lowering energy efficiency in addition to increasing system complexity and cost due to the need for H_2O/CO_2 management [71].

The demonstrated high power output and coking tolerance in gasified carbon at intermediate temperatures represents a critical step toward an economically feasible fuel cell for utilization of gasified coal or carbonaceous solid fuels.

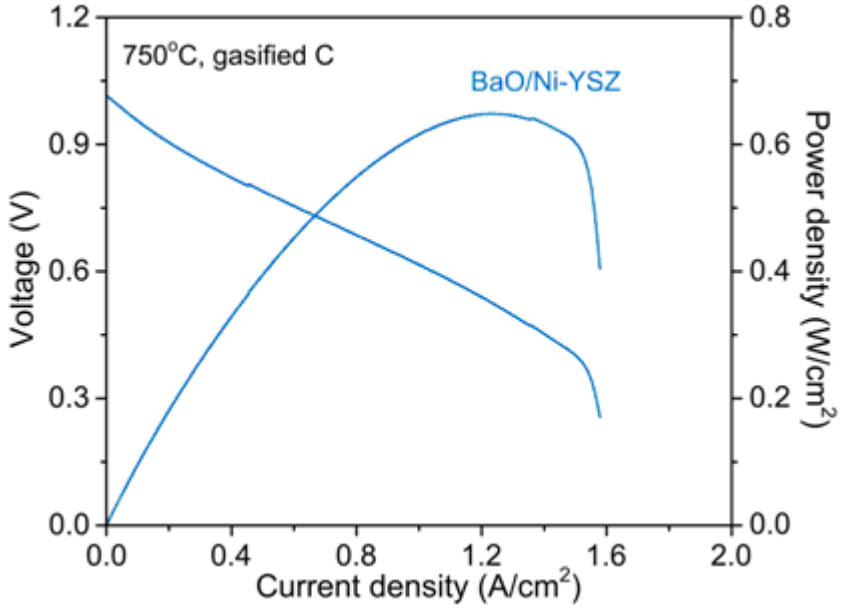

Figure 5-17 Typical current-voltage characteristics and the corresponding power densities measured at 750ºC for cells with BaO/Ni interfaces when gasified carbon was used as the fuel and ambient air as the oxidant in a fluidized carbon bed-SOFC arrangement.

Although wet (~3 v% water vapor) CO_2 was used for gasification, the high performance of the new anode with the fuel gas containing ~96% CO and ~1% H_2 cannot be attributed to the oxidation of H_2, since the cells with a conventional Ni-YSZ anode showed much lower power output under the same conditions. This is further corroborated by the findings of other studies on button-type cells with a Ni-YSZ anode (for low fuel utilization like ours) in a fuel mixture of H2 and CO [72]: the anodic polarization was much larger when the CO content was considerably higher (>55%) in the fuel mixture due primarily to sluggish CO oxidation and a slow shift reaction [72, 73], whereas the difference in performance was relatively small as the H_2 content was increased from

~45% to 100% H_2. Microanalyses of the BaO/Ni-YSZ anodes before and after operation in gasified carbon showed no observable microstructural change or carbon buildup. Furthermore, a cell with a BaO/Ni-YSZ anode displayed stable operation in H_2 for ~1000 h (Figure 5-18), implying good stability of the anode under the operating conditions.

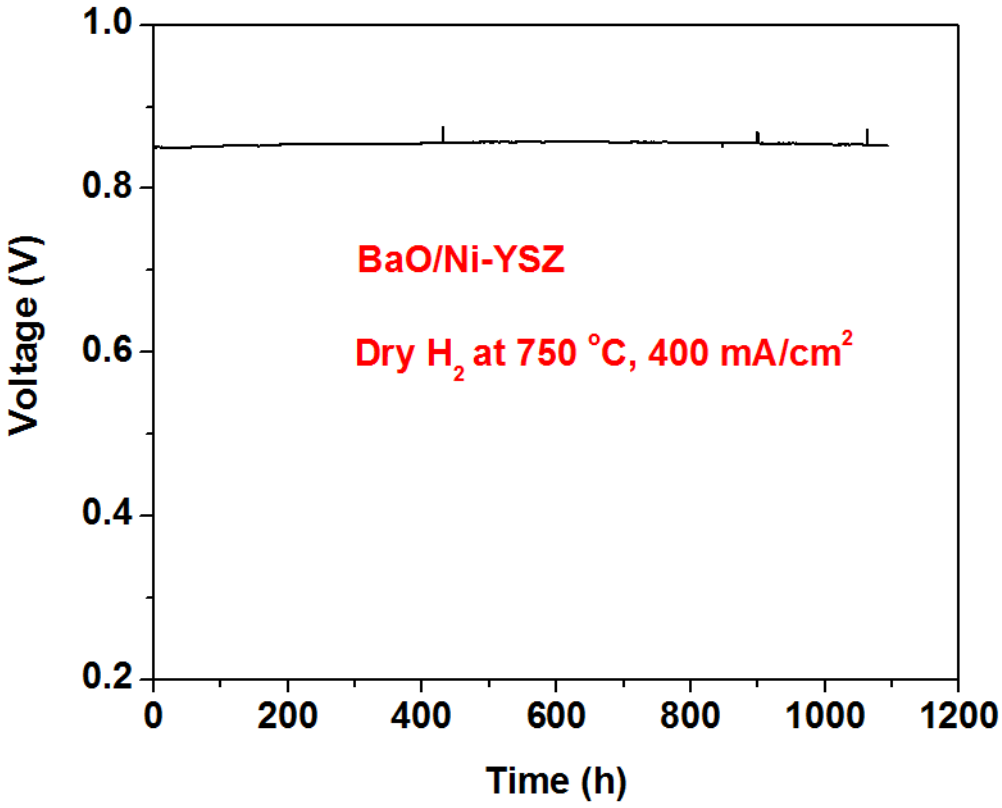

Figure 5-18 Terminal voltage for a cell with a configuration of BaO/Ni-YSZ |YSZ| SDC/LSCF and operated at 400 mA/cm^2 in dry hydrogen at 750^{o}C.

The high performance and tolerance to coking of the electrode at lower temperatures is attributed to the nanostructured BaO/Ni interfaces that do not block the electrochemical processes on the anode while promoting carbon removal in the presence of a small amount of water, which was introduced either by electrochemical oxidation of C_3H_8 when dry C_3H_8 was used as the fuel or by humidification when CO was used as the fuel. It is thus hypothesized that the observed electro-catalytic properties of the new

anode are associated with their unique capability to adsorb and/or absorb water vapor under the operating conditions.

5.5 Assessment of water uptake capability

We used thermo-gravimetric analysis (TGA) and Raman spectroscopy to validate this hypothesis. TGA traces for Ni and YSZ powder samples (Figure 5-19) showed little weight change as the gas was switched from dry to wet (3 v% water vapor) argon with 4 v% H_2, implying that Ni-YSZ anodes hardly interact with water vapor at these temperatures. In contrast, drastic weight gains were observed for BaO powder samples upon exposure to the wet gas, implying that BaO strongly takes up water from the gas phase.

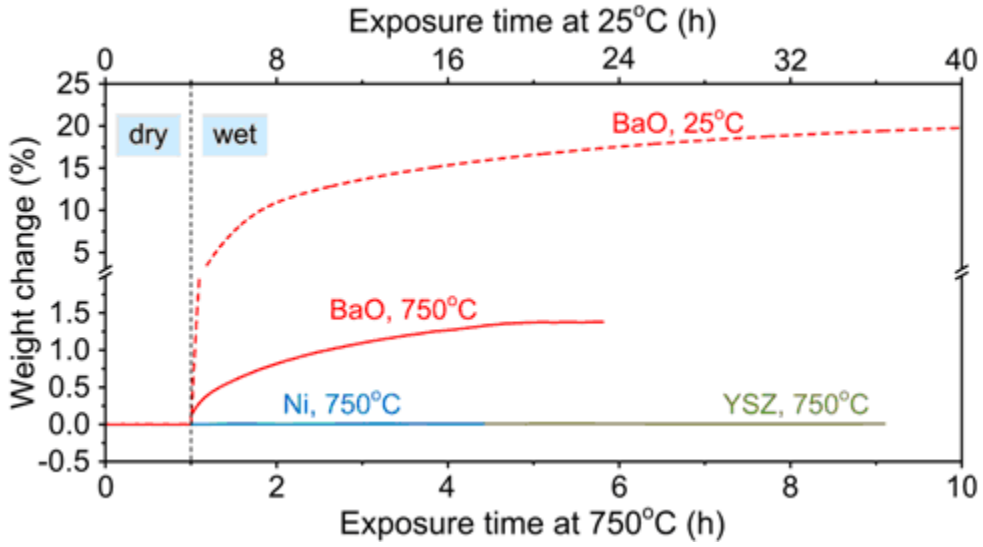

Figure 5-19 Typical TG traces for Ni, YSZ, and BaO powder samples in dry and wet argon with 4 v% H_2 at 25 and 750 ^{o}C.

This is consistent with our theoretical predictions that H_2O dissociatively adsorbs on BaO [74] (see Table 5-1, adsorption energy: –1.35 eV), but only weakly bound to Ni [75] and YSZ (see Table 5-1, adsorption energy: –0.32 eV and –0.54 eV, respectively).

Table 5-1 DFT calculations of H2O adsorption on different materials

Material	Surface	$E_{ads,H2O}$ (eV)	Adsorption Configuration	Adsorption Type
BaO	NaCl, five-layer (001)	–1.35 (1/4 ML)	atop-bound to an O ion through H	dissociative
Ni[a]	fcc, three-layer p(3 × 5) (111)	–0.32 (1/15 ML)	atop-bound through O	Molecularly
YSZ[b]	cubic, nine-layer (111)	–0.54 (1/4 ML)	atop-bound to a Zr ion through H	Molecularly

a. p(3 × 3) (111) (1/9 ML): –0.30 eV.

b. One oxygen vacancy was generated by replacing two Zr^{4+} with two Y^{3+}.

It is noted that the water uptake capacity of BaO decreased from ~20.0% at 25ºC to ~1.4% at 750ºC; however, the amount of water involved at 750ºC is still substantial. The water uptake behavior is also confirmed by Raman spectroscopy (Figures 5-20 and 5-21). A peak near 1600 cm-1, corresponding to the bending mode of water [76], is observed on the Raman spectra collected from a BaO/Ni sample, but absent on that from a pure Ni exposed to wet H2. Further, the broad mode between 3450 and 3700 cm-1 on the spectrum from the BaO/Ni sample exposed to wet H2 indicates the presence of water with weak hydrogen bonds that is likely on the surface of the sample [18].

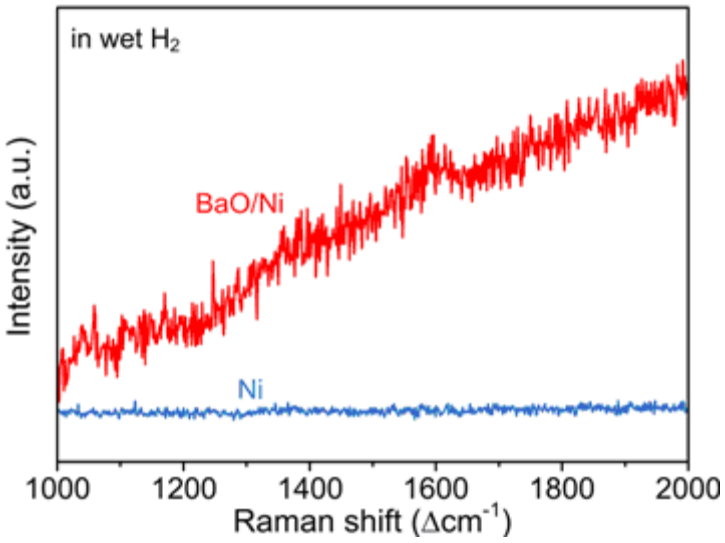

Figure 5-20 Raman spectra collected from BaO/Ni and pure Ni samples in wet H_2 (with ~3 v% H_2O) atmosphere at room temperature.

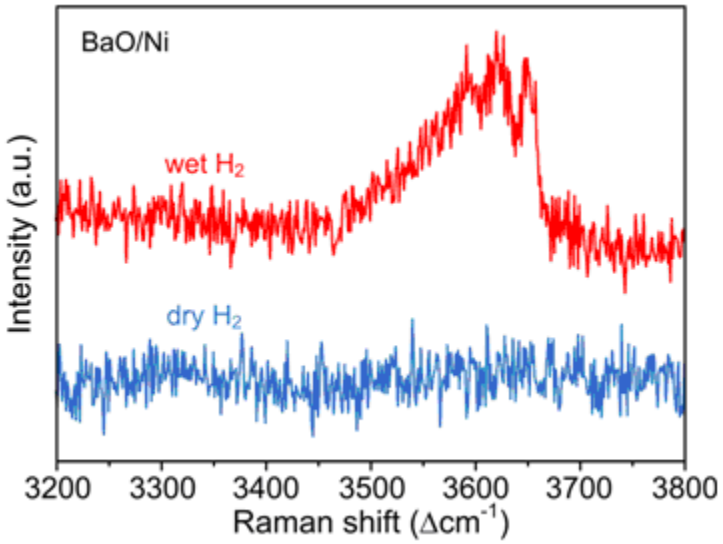

Figure 5-21 Raman spectra collected from BaO/Ni samples in dry and wet H_2 (with ~3 v% H_2O) atmospheres at room temperature.

Our DFT calculations with 1 ML of H_2O on a BaO/Ni surface support the Raman measurements that a H_2O bending mode is at 1594 cm^{-1}, while two stretching modes of adsorbed OH species on BaO are at 3368 and 3716 cm^{-1}, respectively (Figure 5-22). In

contrast, these spectral features disappeared when the same sample was exposed to dry H_2, further confirming the water uptake capability of the surface layers. From these analyses, it is clear that the water associated with the BaO/Ni interfaces play a vital role in enhancing the tolerance to coking and deactivation at intermediate temperatures.

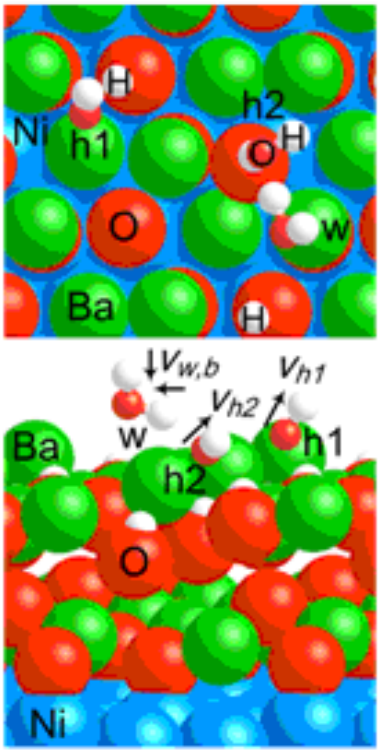

Figure 5-22 Top and side views for the interaction of H_2O on two-layer BaO deposited on p(3×3) Ni(111) containing 6 Ba and 6 O atoms. "w", "h1", and "h2" represent molecularly adsorbed H_2O and dissociated hydroxyl species, while $\nu_{w,b}$, ν_{h1}, and ν_{h2} are the vibration modes of a H_2O bending and two OH stretching (1594, 3716, and 3368 cm^{-1}), respectively. Large balls in Brandeis blue, green, and red are Ni, Ba, and O of BaO, respectively, while small balls in red and white are O from H_2O and H, respectively.

5.6 Reaction mechanism predicted by DFT calculations

In order to gain insight into the mechanism of coking tolerance of this new anode, we constructed models for DFT calculations using the Vienna *ab initio* simulation package (VASP) [77, 78]. Since the Ni{111} surface represents the energetically most stable facet of Ni, we constructed a BaO/Ni(111) surface containing a small BaO chain (3 Ba and 3 O atoms) over a three-layer p(3 × 5) Ni substrate [79] (Figure 5-23). Our DFT calculations using this BaO/Ni(111) model show that the adsorption of CO on BaO (adsorption energy: –0.78 eV; adsorption site: O atop) is much weaker than on Ni (adsorption energy: –2.60 eV; adsorption site: Ni hcp hollow). Given these energies, under the high temperature of the reaction, it is unlikely that the water-gas shift reaction would be effective on BaO. On the other hand, carbon formation (due to dehydrogenation of hydrocarbons or CO disproportionation reaction) occurs readily on Ni catalysts [80], resulting in chemically adsorbed carbon on Ni surfaces. Thus, we examined the mechanism for the removal of carbon near the BaO-like chains on Ni(111). As schematically shown in Figure 5-23, energetically the most plausible reaction pathway can be described as follows: H_2O strongly adsorb on the BaO site of BaO/Ni(111), which releases energy of –1.70 eV and leads to a barrierless O-H bond cleavage and hydrooxylated BaO. In contrast, H_2O weakly adsorbs on the Ni site and a reaction barrier of 1.05 eV has to be overcome to break the O-H bond. Similar to a previous study [79], our calculations show that H_2O dissociation is more favorable near the oxide-metal interface region than on the oxide and metal surfaces. The dissociated OH then reacts with an adsorbed C on the Ni surface via **TS1** (Transition State 1, reaction barrier: 0.36 eV) to form an intermediate COH, which is subsequently dissociated to CO and H via **TS2** (reaction barrier: 0.94 eV). Finally, CO and H diffuse to a triple-phase boundary (TPB), where they are electrochemically oxidized (combine with O^{2-}) to CO_2 and H_2O,

respectively. According to our calculations, the rate-limiting step during this process is the O-H bond cleavage of COH.

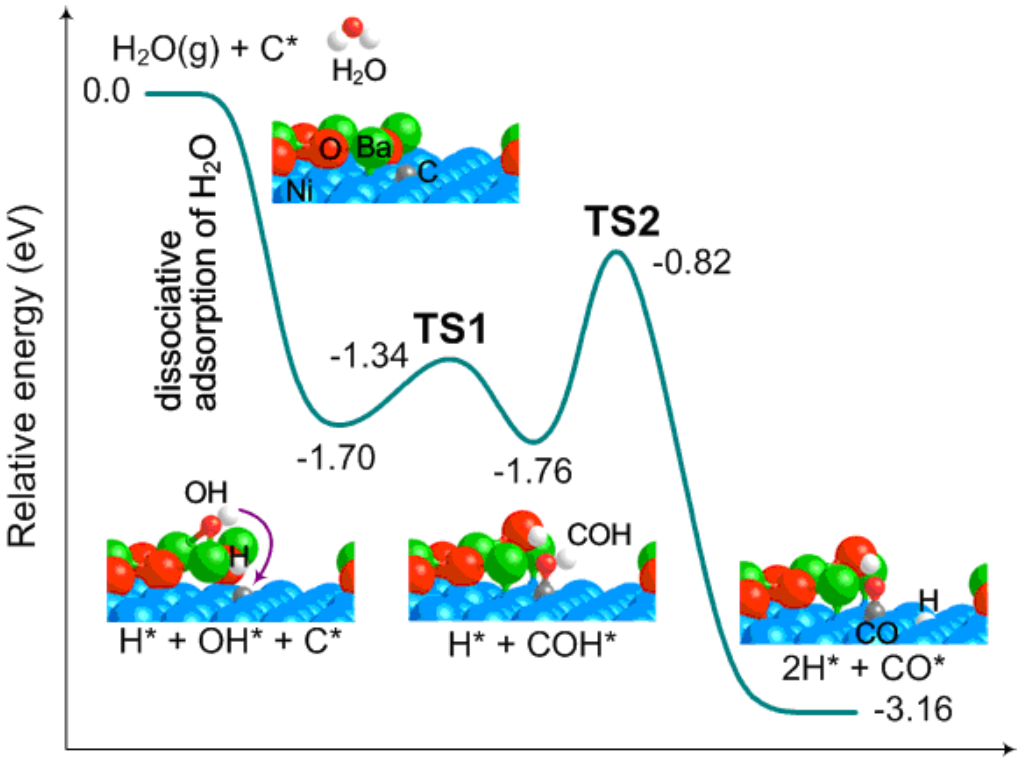

Figure 5-23 A predicted energy profile for the removal of chemisorbed carbon species on BaO/Ni(111), where "*" denotes an adsorbed species on the surface. The energies are relative to gas-phase H_2O and an adsorbed carbon species on BaO/Ni(111)

Thus, the use of new materials with BaO that accelerate the COH dissociation to CO and H may further enhance coking tolerance. Based on this analysis, the most probable elementary processes on the anode with nanostructured BaO/Ni interfaces are schematically illustrated in Figure 5-24 and summarized as follows.

$H_2O \rightarrow H_{ads,BaO} + OH_{ads,BaO}$ dissociative adsorption of H_2O on BaO

$C_{ads,Ni} + OH_{ads,BaO} \rightarrow COH_{ads,Ni}$ COH formation on Ni

$COH_{ads,Ni} \rightarrow CO_{ads,Ni} + H_{ads,Ni}$	CO and H formation on Ni
$CO_{ads,Ni} \rightarrow CO_{tpb}$; $H_{ads,Ni} \rightarrow H_{tpb}$	diffusion to the TPB
$CO_{tpb} + O^{2-} \rightarrow CO_2 + 2e^-$	CO oxidation at the TPB
$2H_{tpb} + O^{2-} \rightarrow H_2O + 2e^-$	H oxidation at the TPB

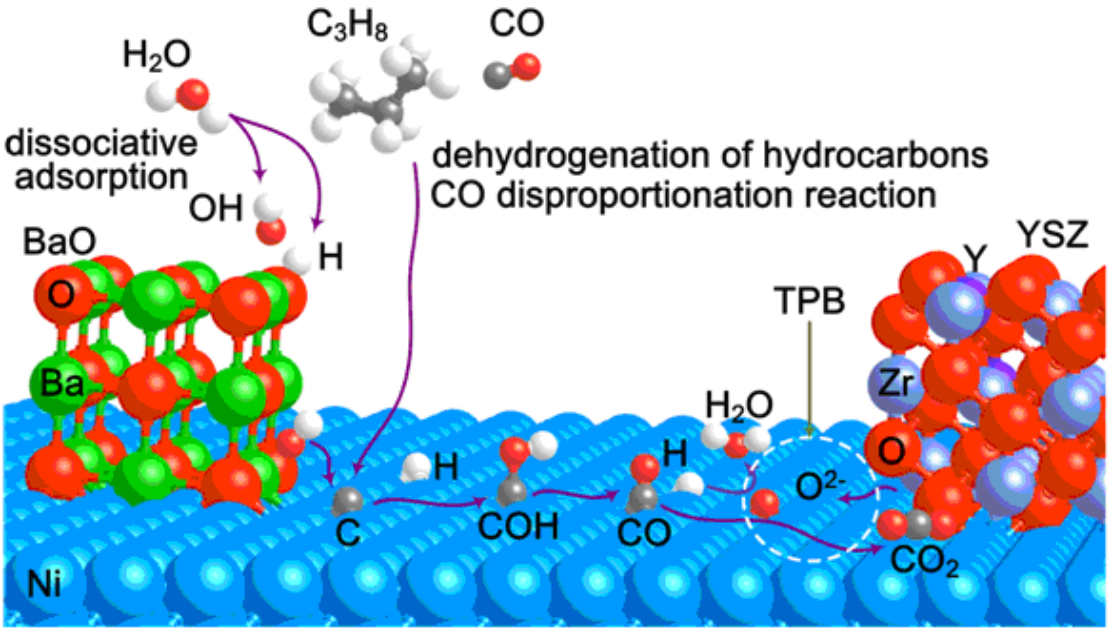

Figure 5-24 Schematic of a proposed reaction mechanism of carbon-tolerant BaO/Ni(111). Large balls in Brandeis blue, green, red, blue gray, and purple are Ni, Ba, O of BaO or YSZ, Zr, and Y, respectively, while small balls in red, white, and gray are O from H_2O and H, and C, respectively.

Overall, the water-mediated carbon removal reactions occur more favorably at the BaO/Ni interfaces. The catalyst works synergistically: the dissociation of water takes place on the BaO, the carbon formation occurs on the Ni sites of BaO/Ni, and all subsequent steps occur at or near the BaO/Ni interfaces. Our results imply that the high performance and coking tolerance of this new anode relies heavily on the direct participation of the BaO/Ni interfaces.

5.7 Summary

In conclusion, a new anode with nanostructured BaO/Ni interfaces were fabricated by vapor deposition and subsequent reduction, which do not impede the charge transfer on the anode while promoting a water-mediated carbon removal process and enhancing its resistance to carbon buildup and deactivation under fuel cell operating conditions. While the demonstrated higher performances and coking tolerance of this anode at lower temperatures represent a vital step toward a cost-effective fuel cell for direct conversion of hydrocarbons and gasified carbonaceous solid fuels to electricity, the impact of other contaminants on the performance of this anode is yet to be investigated. It is possible, however, that many contaminants may be effectively removed through proper cleaning, an approach feasible for stationary power generation and preferred for minimizing environmental impact.

CHAPTER 6

NEW INSIGHTS INTO SULFUR POISONING BEHAVIOR

6.1 Experimental

The diameter of the anode and electrolyte of the anode-supported cells (from Delphi) was 9 mm while the cathode was smaller, with an active area of 0.28 cm^2. The thicknesses of the Ni-YSZ anode, the YSZ electrolyte, and the LSCF cathode layers were ~500, ~10, and ~30 μm, respectively. To make electrical connection, two Pt lead wires were bonded to the current collector on both the anode and the cathode. To seal a button-cell on the test fixture, a Ceramabond® 552VFG sealant (Aremco, abbreviated as C552), which has been widely used in single cell testing, was applied to the edge of the cell. The composition of C552 glass, as determined using an Inductively Coupled Plasma–Optical Emission Spectrometer (ICP-OES), can be specified as SiO_2-Al_2O_3-MgO-CaO with mole ratio of 70:36:1:1. For direct comparison, a new sealant developed by Pacific Northwest National Laboratory in the US**,** G18 glass (BaO-CaO-Al_2O_3-SiO_2-B_2O_3 with mole ratio of 35:15:5:35:10 [31, 81]), was also used in this study. After cell assembling/sealing, all cells were dried in air at room temperature for ~24 h. They were subsequently inserted into a multi-cell testing furnace capable of simultaneously testing 12 button cells under various electrochemical (e.g., potentiostatic, galvanostatic, or potentiodynamic) conditions at a temperature up to 1050 ^oC. The gas distribution system can deliver gas mixtures from humidified inert gas, H_2, and H_2 with different concentrations of H_2S. It can supply up to four different fuel mixtures with H_2S concentration varying from 0.05 to 100 ppm by volume. For a typical 3,000 h long-term testing, all cells were first operated in 50%H_2-48.5%N_2-1.5%H_2O for ~300 h, before the fuel was switched to H_2S-contaminated H_2. The flow rate of H_2 was ~7.5 mL/min for each cell. The fuel utilization was ~11% at a current density of 400 mA/cm^2.

While anodic overpotential is often directly measured in an well-designed electrolyte-supported cell to characterize the sulfur poisoning effect[82], it is impossible to do the same in an anode-supported cell with electrolyte thickness of ~10 μm [83]. Any attempts to do 3-electrode measurements on such a cell could result in substantial errors in estimation of half-cell overpotential. Accordingly, the relative changes in cell voltage or current density were measured to examine indirectly the electrochemical behavior of the Ni-YSZ anode in H_2S-containing fuels [84-87]. The cell voltages and current densities were recorded continuously using an Arbin fuel cell testing system (12 channels). During the test, impedance spectra as well as I-V curves were also collected periodically for some cells. Impedances were measured in the frequency range from 0.01 Hz to 100 K Hz with an EG&G Potentialstat/Galvanostat (Model 273A) and lock-in amplifier (5210).

6.2 High-performance anode-supported SOFCs

Anode-supported structures are widely employed in the state-of-the-art SOFCs because of the high power output. Figure 6-1 shows the current-voltage characteristics and the corresponding power densities at 750 ^oC for a typical YSZ-based anode-supported fuel cell using G18 sealant. This cell produced a peak power density of 844 mW/cm^2 at 750^oC when humidified hydrogen (50% H_2, 1.5% H_2O, and 48.5% N_2) was used as the fuel and ambient air as the oxidant. The power outputs of this anode-supported cell (with ~10 μm thick YSZ electrolyte) is much higher than those of a typical electrolyte-supported cell (with ~300 μm thick YSZ electrolyte) due primarily to the dramatic reduction in electrolyte thickness and the superior anode-electrolyte interface resulted from co-firing of the Ni-YSZ anode and the YSZ electrolyte. Meanwhile, the OCV (1.06 V at 750 ^oC) of this anode supported cell is as high as that of an electrolyte-supported cell, indicating that the thin electrolyte is sufficiently dense. These anode-supported cells are extremely stable; they were operated in H_2 for up to ~3500 h with negligible degradation in performance.

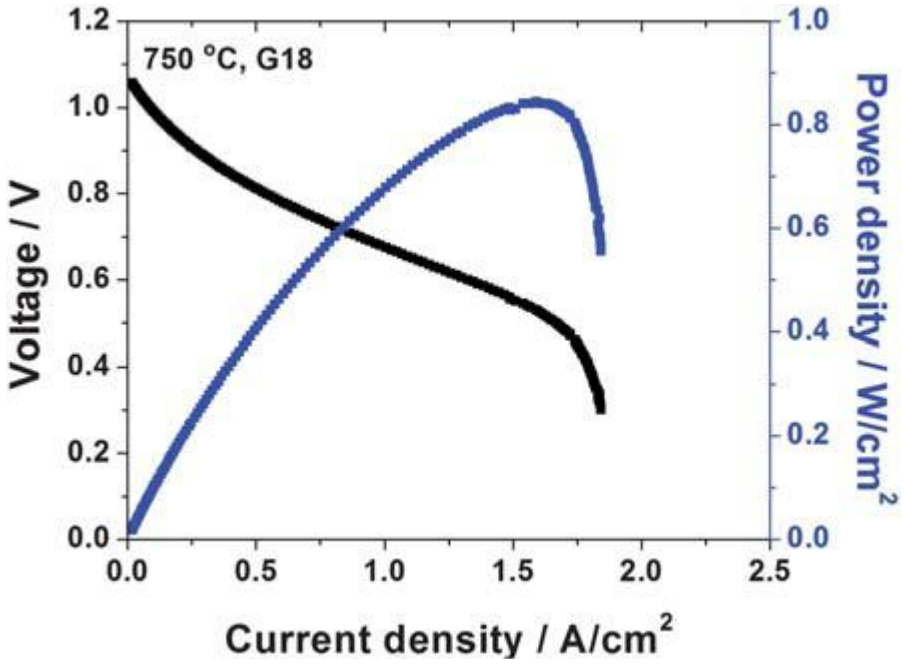

Figure 6-1 Typical cell voltages and power densities as a function of current density at 750 ^{o}C for the anode-supported fuel cells in this study using G18 sealants when humidified hydrogen (50% H_2, 1.5% H_2O, and 48.5% N_2) was used as fuel and ambient air as oxidant.

Figures 6-2 and 6-3 shows the terminal voltages for cells with G18 sealant before and after the fuel was switched from clean hydrogen to hydrogen containing 0.8 and 10 ppm H_2S. As expected, the cell terminal voltages experienced rapid drops upon initial exposure to H_2S in all cases. The cell voltages further decreased when the concentration of H_2S was changed from 0.8 ppm to 1.1 ppm, indicating that Ni-YSZ anode is very sensitive to miniscule concentration of H_2S. More importantly, unlike what was observed in previous studies[85, 86], there was no observable subsequent degradation in performance (i.e., the so-called second-stage poisoning) in these cells up to ~3,000 hours after the rapid drop in performance due to the initial exposure to H_2S.

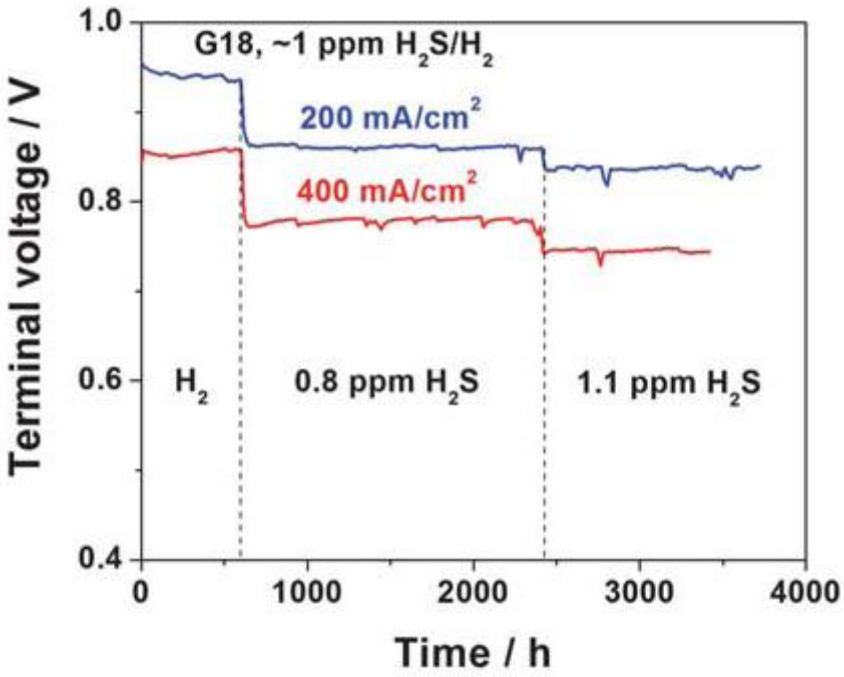

Figure 6-2 Performances of the test cells using G18 sealant operated at 750 ^{o}C at a constant current density of 200 and 400 mA/cm^2 in hydrogen for the first ~ 600 h and then in hydrogen with 0.8 ppm H_2S. The concentration of H_2S in the hydrogen was changed from 0.8 ppm to 1.1 ppm at ~ 2400 h (change of gas cylinder); the effect of H_2S concentration is clearly seen.

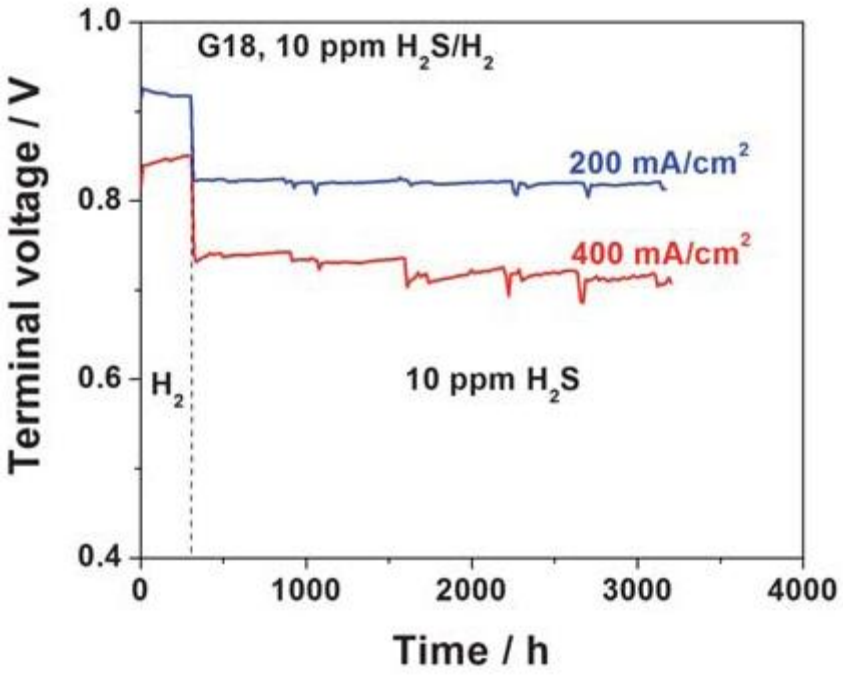

Figure 6-3 Performances of the test cells (with G18 sealant) operated at 750 ^{o}C at a constant current density of 200 and 400 mA/cm^2 in hydrogen for the first ~300 hours and then in hydrogen with 10 ppm H_2S.

6.3 The initial drop in performance due to sulfur poisoning

To examine how operating conditions influence the degree of initial degradation in performance due to sulfur poisoning, we recorded the cell voltage drops as a function of H_2S concentration and current density. Figure 6-4 shows some typical cell voltage drops of test cells upon initial exposure to fuels containing H_2S. While there were some small differences in performance between the cells using the C552 sealant and those using the G18 sealant (due probably to slight variations in cells and H_2S concentration), the general trends are similar for both anode-supported cells, indicating that an initial drop of significant magnitude in power output is unavoidable for a Ni-YSZ anode. In contrast, the magnitude of this initial performance drop appears much less dramatic in an electrolyte-supported cell (with large cell resistance) than an anode-supported cell (with

small cell resistance). For example, a terminal voltage drop of ~5.1% and ~7.2% were observed in electrolyte-supported cells under a constant current density of 241 mA/cm^2 as the fuel was switched from clean hydrogen to hydrogen containing ~1 and 10 ppm H_2S, respectively; but the voltage drops in an anode-supported cell were ~8% and ~11% under similar conditions, as seen in Figure 6-4. This is expected partially because the anode polarization resistance constitutes a smaller portion of the total resistance for an electrolyte-supported cell (with thicker electrolyte) than for an anode-supported cell (with much thinner electrolyte). The discrepancy in anode structures for electrolyte- and anode-supported cells may also contribute the different degrees of degradation in performances.

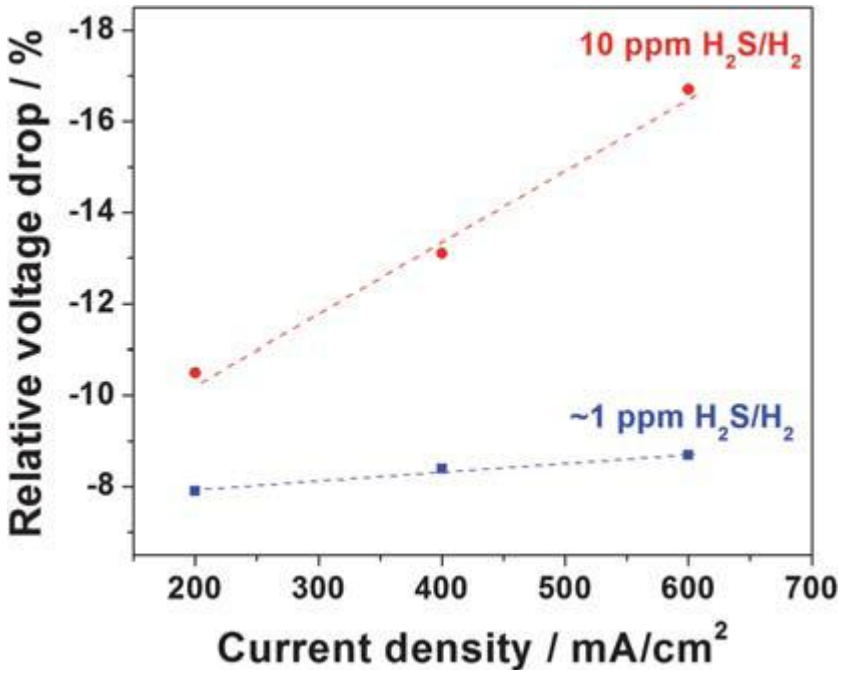

Figure 6-4 Typical drop in cell voltages for test cells using G18 sealant upon initial exposure to H_2 containing ~1 and 10 ppm H_2S at 750 ^oC

In general, the immediate drop in cell performance upon exposure to H_2S increases with the concentration of H_2S, regardless of the types of cells or electrochemical testing conditions.

However, the rates of poisoning (or degradation in performance) are much slower in anode-supported cells (with much thicker Ni-YSZ anodes) than in electrolyte-supported cells (with much thinner Ni-YSZ anodes). For instance, anode-supported cells usually took ~32 and ~15 h to reach relatively steady state in hydrogen containing ~1 and 10 ppm H_2S, respectively. In contrast, it took only a few minutes for electrolyte-supported cells to reach a steady state [84, 86]. This seems to be consistent with the mechanism of sulfur poisoning. Since the sulfur levels used in the present study will not lead to formation of bulk sulfides [56, 88], the sulfur poisoning is most likely caused by the strong adsorption of the elemental sulfur on Ni surface and the three-phase boundaries (TPB) between Ni, electrolyte, and the fuel. Sulfur would then block the active site for fuel oxidation in a Ni-YSZ anode and increase the polarization resistance [56, 89]. Thus, for an anode-supported cell with a thick anode (~500 μm), it takes longer for all Ni surfaces to be saturated with sulfur. The adsorption of sulfur on Ni may propagate from the outer layer to the inner active layer of anode. In contrast, for an electrolyte-supported cell with a thin anode (~30 μm), it takes less time for the Ni surfaces to be saturated with sulfur.

Similar to a previous study on electrolyte-supported cells [84], the relative increase in cell resistance for an anode-supported cell operated under galvanostatic (constant current) mode can be expressed as,

$$\Delta R_{cell\_r} = \frac{\Delta R_{cell}}{R_{cell\_0}} = \Delta P_r \frac{U_0}{E_0 - U_0}$$

where E_0 is the open circuit voltage, U_0 is the cell terminal voltage before exposure to H_2S, and ΔP_r is the relative drop in cell power output (or cell voltage). Thus, the relative increase in cell resistance for anode-supported cells can be calculated from the relative cell voltage drop, as shown in Figure 6-5. An anode-supported cell (with thin electrolyte) displayed a larger relative increase in cell resistances than an electrolyte-supported cell (with thick electrolyte) [84]. In addition, the relative increase in cell resistances is smaller

when the cell current is higher, indicating that the water produced at the active sites on anode surface from fuel oxidation may promote the oxidation and removal of adsorbed sulfur [90].

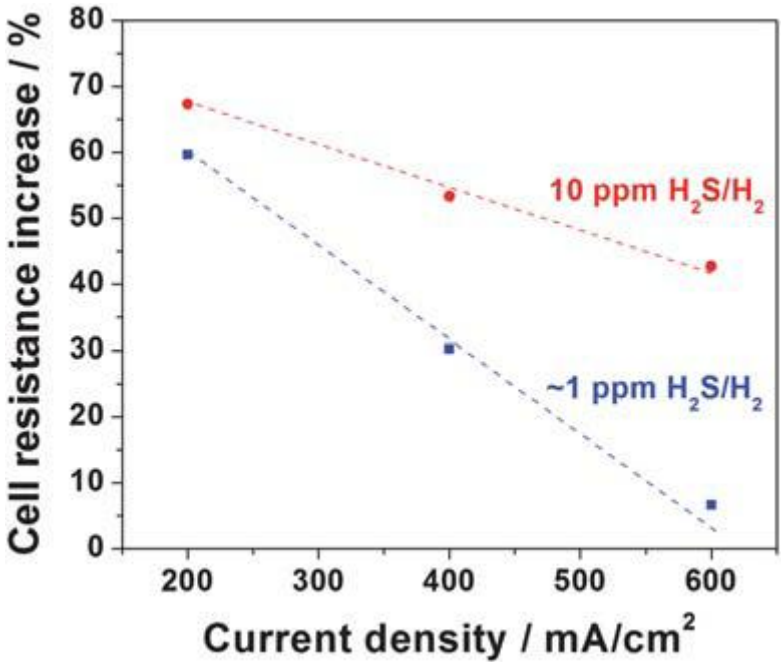

Figure 6-5 Calculated relative cell resistance increase as a function of cell current density upon exposure to hydrogen containing ~1 and 10 ppm H_2S at 750 ^oC under the galvanostatic conditions for the test cells (with G18 sealant).

Furthermore, it seems that the degree of sulfur poisoning (or the relative drop in voltage) was more sensitive to cell current density when the H_2S concentration was higher, as seen from the slopes of the relative voltage drop versus the cell current density shown in Figure 6-4. For example, the observed relative drop in cell voltage was less sensitive to cell operating current density when the concentration of H_2S was ~1 ppm: –7.9% at 200 mA/cm^2, –8.4% at 400 mA/cm^2, and –8.7% at 600 mA/cm^2. In contrast, the relative drop in cell voltage increased with operating current density when the concentration of H_2S was 10 ppm: –10.5% at 200 mA/cm^2, –13.1% at 400 mA/cm^2, and –16.7% at 600 mA/cm^2. Because cell resistance is inversely proportional to cell

performance, consequently, the relative cell resistance change due to sulfur poisoning would change more dramatically with cell current density when the H_2S concentration was ~1 ppm than 10 ppm, as seen from the slopes of the relative cell resistance change versus cell current density shown in Figure 6-5. This can be explained as follows: at lower H_2S concentration, less reaction sites in the Ni-YSZ anode are occupied by adsorbed sulfur. Under the same current density, the percentage of adsorbed sulfur atoms removed by oxidation is more significant in ~1 ppm H_2S than that in 10 ppm H_2S. In other words, the water-mediated oxidation and removal of adsorbed sulfur becomes less effective at higher concentration of H_2S, but still considerable at ~1 ppm of H_2S.

Figure 6-6 shows several typical impedance spectra for cells before and after initial exposure to ~1 ppm H_2S at different operating current densities. Clearly, the increase in cell polarization resistances after exposure to H_2S (or the degree of sulfur poisoning) diminished with the increase in current density. This is consistent with the trend of calculated relative increase in cell resistance shown in Figure 6-5 for the case with hydrogen containing ~1 ppm H_2S, indicating that the effect of sulfur removal by oxygen ion or water produced at the active sites is more pronounced when the concentration of H_2S is relatively low.

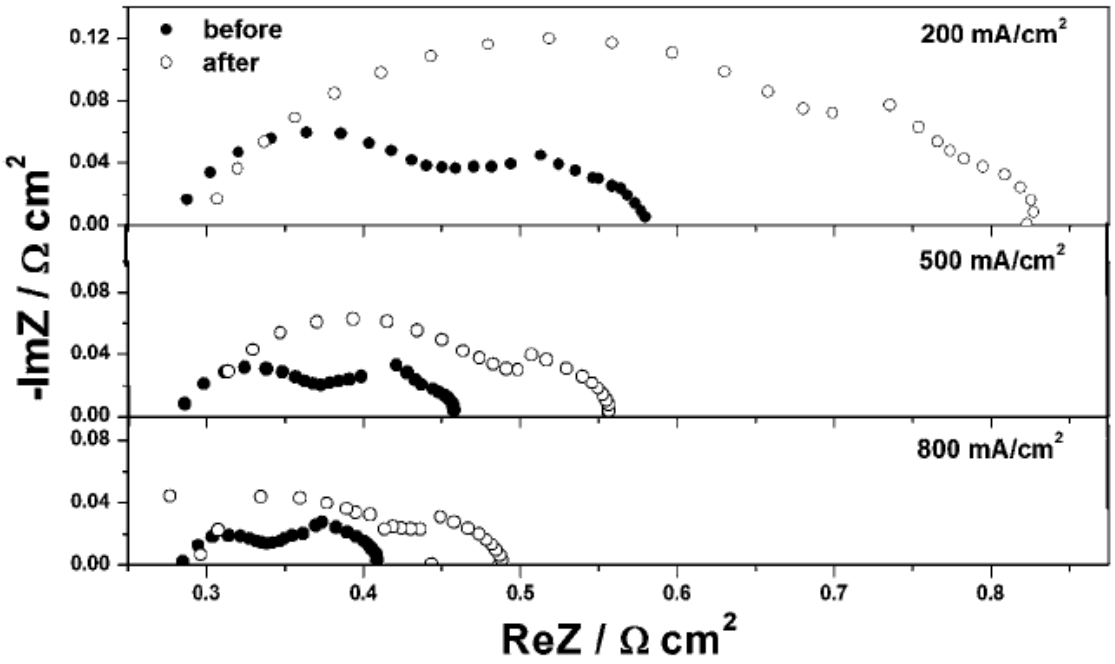

Figure 6-6 Impedance spectra of anode-supported cells (with C552 sealant) operated at a constant current density of 200, 500, and 800 mA/cm^2 before and after ~1 ppm H_2S was introduced into the fuel at 750 ^oC

6.4 The subsequent degradation after the initial exposure to H_2S

Exposure of cells to H_2S-contaminated fuels for an extended period of time (up to ~3000 h) was carried out to investigate the subsequent behavior of Ni-YSZ anodes after the initial drop in performance. Shown in Figures 6-7 and 6-8 are normalized changes in cell voltage (in percentage) after the large, initial drop in cell voltage due to exposure to hydrogen containing ~1 ppm H_2S for cells sealed with C552 and G18 sealants, respectively. Obviously, the subsequent degradation in performances for all the cells were relatively small when the concentration of H_2S was ~1 ppm, although there was indeed a gradual decline in terminal voltage for the cell with C552 sealant at a current density of 200 mA/cm^2. It is worthy of note that a voltage step at ~500 and ~1800 h occurred for cells with C552 and G18 sealants, respectively, which was caused by

replacement of H_2S gas cylinders with different concentrations of H_2S (0.8 ppm and 1.1 ppm). These slight voltage changes further suggest that Ni-YSZ anode is susceptible to sulfur poisoning even under miniscule concentration of H_2S.

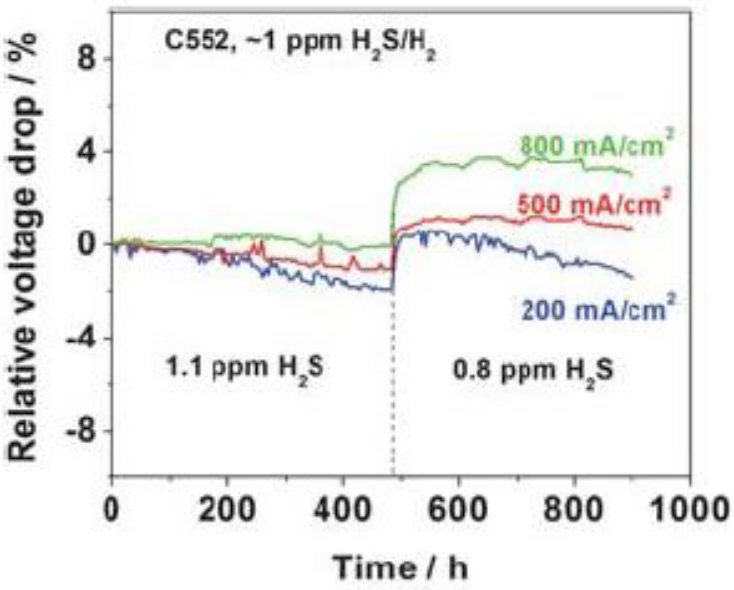

Figure 6-7 Normalized voltage changes (in percentage) after the large initial voltage drop due to switching from clean H_2 to H_2 containing ~1 ppm H_2S for cells with C552 sealant. These variations in cell voltage correspond to additional degradation under a steady operating condition. Note: H_2S gas cylinders were changed at ~500 h.

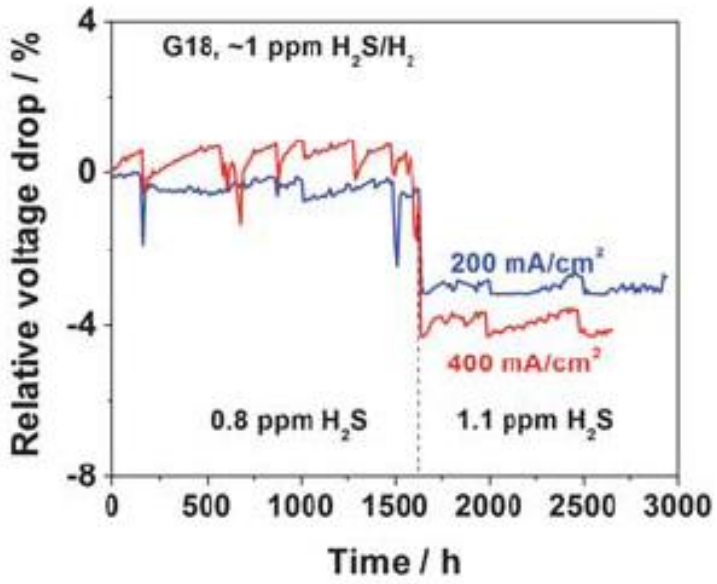

Figure 6-8 Normalized voltage changes (in percentage) after the large initial voltage drop due to switching from clean H_2 to H_2 containing ~1 ppm H_2S for cells with G18 sealant. These variations in cell voltage correspond to additional degradation under a steady operating condition. Note: H_2S gas cylinders were changed at ~1600 h.

When the concentration of H_2S was increased to 10 ppm, significant degradation in performance was observed for the cells with C552 sealant under constant current densities, as shown in Figure 6-9. After ~1000 h operation, the relative drops in cell voltage were –9.6%, –14.2% and –15.6% at 200, 500 and 800 mA/cm^2, respectively. The accumulated relative cell voltage drop over the period of testing was as much as the initial drop in performance upon initial exposure to H_2S. It is troublesome to note that this degradation continued even after 1000 h of exposure to H_2S, suggesting the severity of the degradation effect. This subsequent degradation was also observed by others [85-87] and attributed to continuous sulfur poisoning of anode. In contrast, when G18 sealant was used in the anode-supported cells, there was little observable degradation in performance under the steady testing conditions, as shown in Figure 6-10 (the fluctuations in cell

voltage are believed to be originated primarily from unstable flow of the H_2-H_2S-N_2 fuel mixtures). For cells run at 200 and 400 mA/cm^2, the degradations were only ~0.2% and ~2.2% after ~3000 h operation, respectively. Therefore, the continuous degradation in performance is most likely not inherent to Ni-YSZ and can be eliminated in properly designed experiments.

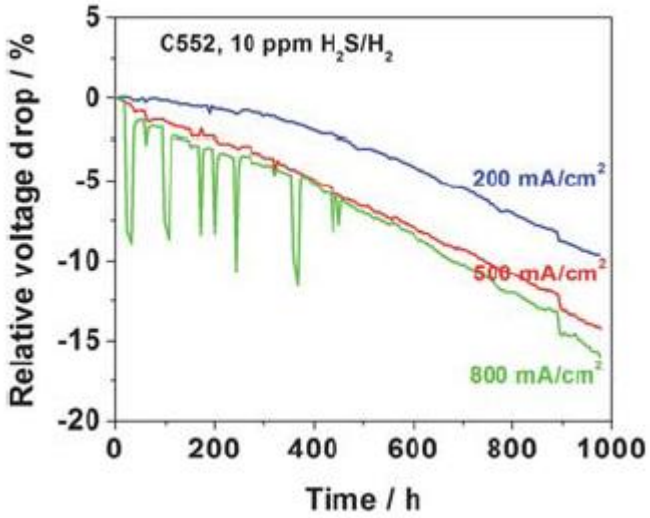

Figure 6-9 Normalized voltage changes (in percentage) after the large initial voltage drop due to switching from clean H_2 to H_2 containing 10 ppm H_2S for cells with C552 sealant. These voltage drops correspond to a continued degradation in performance.

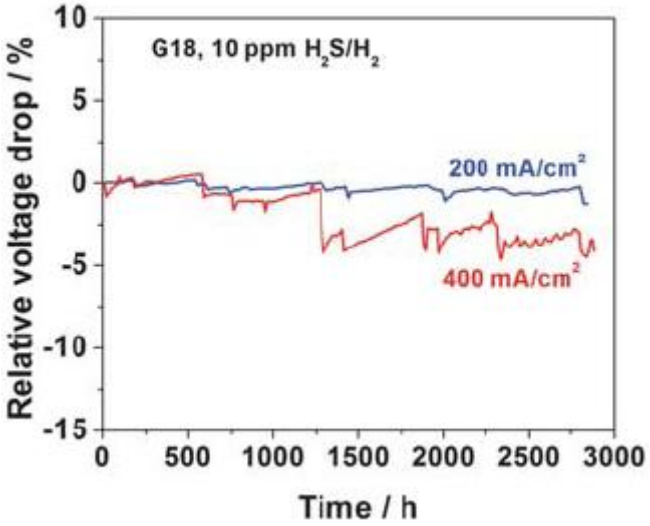

Figure 6-10 Normalized voltage changes (in percentage) after the large initial voltage drop due to switching from clean H_2 to H_2 containing 10 ppm H_2S for cells with G18 sealant. These voltage drops correspond to a continued degradation in performance.

There are two possibilities which might cause the continuous degradation in cells sealed by C552 sealant. First, segregation of impurities from glass sealant onto YSZ electrolyte is well known to take place [91]. It is possible that the diffusion of detrimental elements in C552 sealant could lead to continuous poisoning of the anode when the sealant interacts unfavorably with H_2S, while the G18 sealant might prevent such undesirable diffusion and/or interactions. Second, the leakage of H_2S in the anode through the C522 sealant might also cause the performance degradation of cathode. It has been reported that sulfur species could poison the cathode performance[92]. In comparison, the G18 sealant demonstrated excellent chemical and thermal compatibilities with other fuel cell components [81], thereby it might inhibit the performance drop by preventing the leakage of sulfur species through the sealant. Further experiments are required to clarify on this point.

6.5 Summary

In conclusion, some new insights have been revealed from long-term (~3,000 hours) testing of the-state-of-the-art, high-performance, anode-supported SOFCs. An inevitable drop in power output upon exposure to small amount of H_2S appears more dramatic in a high-performance anode-supported cell than in a low-performance electrolyte-supported cell, thus creating an illusion that a low-performance cell is more sulfur tolerant than a high performance cell. Also, the time it takes for the cell to reach a steady state upon exposure to H_2S is much longer for an anode-supported cell than for an electrolyte-supported cell, mostly because the Ni-YSZ anode in an anode-supported cell

is much thicker than that in an electrolyte supported cell. Impedance spectroscopy and equivalent circuit analysis suggest that the degree of sulfur poisoning (or the increase in cell resistance due to sulfur poisoning) can be alleviated by the water produced at the active sites from electro-oxidation of hydrogen; this effect is more pronounced at lower concentration of H_2S. Furthermore, the previously observed continuous degradation in performance after initial exposure to H_2S may be associated with other possible complications, including contamination of Ni-YSZ anode by the sealant or sulfur poisoning of cathode due to leaking through the sealant. With proper sealant (e.g., G18 glass), stable power output (without continuous degradation in performance) has been demonstrated by anode-supported cells fueled with hydrogen containing up to ~10 ppm H_2S for ~3,000 hours operation.

CHAPTER 7

NEW COMPOSITE CATHOD WITH $H^+/O^{2-}/e^-$ TRANSPORT

7.1 Experimental

7.1.1 Modified co-pressing of anode/electrolyte bilayers

Two different methods were used to prepare $Ba(Zr_{0.1}Ce_{0.7}Y_{0.2})O_{3-\delta}$ powders. In the solid state reaction (SSR) method, stoichiometric amounts of high-purity barium carbonate, zirconium oxide, cerium oxide, and yttrium oxide powders (all from Aldrich Chemicals) were mixed using ball-milling with stabilized zirconia media in ethanol for 48 h. The resultant mixture was dried at 60^{o}C for 24 h, followed by calcination at 1100 ^{o}C for 10 h. The ball milling and calcination under same conditions were repeated twice to obtain pure phase. In the glycine nitrate process (GNP), suitable amounts of $Ba(NO_3)_2$, $Ce(NO_3)_3$, $Y(NO_3)_3$, and $ZrO(NO_3)_2$ (all from Aldrich Chemicals) were dissolved in distilled water (0.1 M) and mixed with glycine (molar ratio of NO_3^- to glycine=1.5:1). Then the solution was heated on a hot plate to vaporize water, converted to gel, and finally ignited to flame. The resultant yellow ash was then fired at 900 ^{o}C for 2 h to obtain BZCY powders. In subsequent discussions, BZCY-SSR stands for BZCY powders prepared by a solid state reaction process whereas BZCY-GNP for those derived from a glycine nitrate process.

A co-pressing and co-firing process was then used to prepare anode-supported electrolyte bilayers. Mixed powders of NiO, BZCY-GNP, and rice starch (from Aldrich Chemicals) with a weight ratio of 65:35:10 was pre-pressed at 100 MPa in a stainless steel mold as the substrate. Subsequently the BZCY powders from SSR were added to the surface of green anode through a screen (500 meshes) to guide uniform distribution of BZCY powders on the anode. Without a screen, it is difficult to uniformly and fully cover the anode when the amount of BZCY electrolyte powders was relatively

small to make the electrolyte layer sufficiently thin. The anode-supported electrolyte bilayers were uniaxially co-pressed at 250 MPa, followed by sintering at 1350^{o}C for 6 h.

7.1.2 Composite cathodes

Composite cathode consisting of $Sm_{0.5}Sr_{0.5}CoO_{3-\delta}$ (SSC, derived from GNP as describe elsewhere [37]) and BZCY (weight ratio of 7:3) were prepared as follows. The mixture of SSC and BZCY was mixed with V006 and acetone (weight ratio of 1:1:1) to form a cathode slurry, which was brush-painted on the BZCY electrolyte. The composite cathode was then fired at 1000 ^{o}C for 3 h.

LSCF powders were synthesized using a citrate process. 1 M precursor solution with $La(NO_3)_3$, $Sr(NO_3)_2$, $Co(NO_3)_2{\cdot}6H_2O$ and Fe $(NO_3)_3{\cdot}9H_2O$ (from Alfa Aesar) in stoichiometric ratio was added drop by drop in a 3 M citric acid solution under vigorous stirring. The pH value of the solution was adjusted to about 8 by ammonia. The solvent in the solution was then evaporated at 50–80^{o}C for about 2 h to form a sol, followed by drying in an oven at 120–160 ◦C for 1 h to form a gel, which was finally fired at 800^{o}C for 2 h. BZCY and LSCF powders (weight ratio of 3:7), V006 thinner (from Haurreaus), and acetone were then mixed in weight ratio of 1:1:1 to form cathode slurry. The slurry was brush-painted on BZCY surface of a NiO-BZCY/BZCY bi-layer, followed by firing at 1000 ^{o}C for 3 h. The composite cathode is ~25 μm thick.

7.1.3 Cobalt-doped BZCY cathode

Powders of Co-doped BZCY were synthesized by a conventional solid-state reaction method. The intended compositions of the materials prepared were $BaZr_{0.1}Ce_{0.7}Y_{0.2-x}Co_xO_{3-\delta}$ (x=0, 0.02, 0.05, 0.075, 0.1, 0.2), which were abbreviated as

0Co, 2Co, 5Co, 7.5Co, 10Co, and 20Co, respectively. Stoichiometric amounts of high-purity barium carbonate, zirconium oxide, cerium oxide, cobalt oxide, and yttrium oxide powders (all from Aldrich Chemicals) were mixed using ball-milling with stabilized zirconia media in ethanol for 48 h. The resultant mixture was dried at 60^{o}C for 24 h, followed by calcination at 1100 ^{o}C for 10 h. The ball milling and calcination under same conditions were repeated twice to obtain pure phase. The calcined mixture was then iso-statically pressed into a disk at 274.6MPa. The disks were then sintered at 1550 ^{o}C for 10 h in air to obtain samples with relative density greater than 96%. The electrical conductivities of Co-doped BZCY samples were evaluated by four-probe impedance measurements. First, the sintered pellets were cut to rectangular bars with a typical dimensions of 2×1×10 mm. Second, platinum paste was applied to both end of the bar and fired at 900 oC for 30 min to form working and counter electrodes. Third, two platinum wires were then attached to the bar close to the working and counter electrodes, respectively, as reference electrodes.

7.1.4 Characterizations

The phase composition of the composite cathodes fired at 1000~1200 oC for 10 h was examined using X-ray diffraction (XRD) analysis (PW-1800 system, 2θ=20-80o). The morphologies of the electrodes before and after operation were examined using a scanning electron microscope (SEM, Hitachi S-800).

The button cells were mounted on an alumina supporting tube for fuel cell testing at 400-750^{o}C with humidified hydrogen (3 vol% H_2O) as fuel and stationary air as oxidant. The Ohmic and the interfacial resistances were separated by impedance spectroscopy using a Solartron 1286 electrochemical interface and a Solartron 1255 HF frequency response analyzer interfaced by a computer in the frequency range from 0.01 Hz to 10 MHz.

7.2 Optimization of anode/electrolyte bilayers

It is critical to obtain dense BZCY electrolyte membrane with right stoichiometry in the anode-supported structure that is required for low ohmic resistance and fast charge transfer between electrolyte and cathode. The fabrication of thin BZCY electrolyte on porous NiO-BZCY support is essentially difficult because of the poor sinterability and facile barium evaporation during high-temperature sintering. Thus, prior to discussion of the compatible cathode, it is necessary to develop a good anode/electrolyte bilayer with sufficient porosity in the support while maintaining high density and conductivity of the electrolyte.

Figure 7-1 shows typical X-ray diffraction patterns of the BZCY powders prepared by solid state reaction and glycine nitrate process, suggesting that single phase was obtained using both methods. This is required to ensure high conductivity and stability.

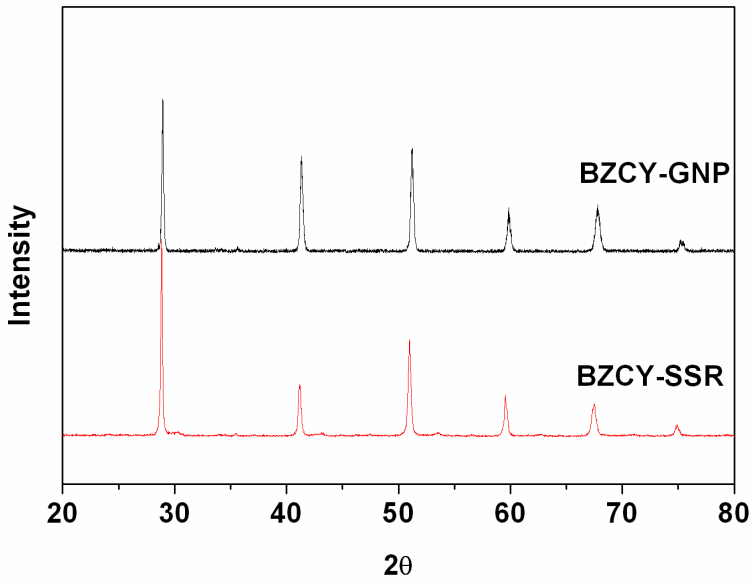

Figure 7-1 X-ray diffraction patterns of the BZCY powder synthesized by glycine nitrate process and solid state reaction.

Shown in Figure 7-2 are the typical morphologies of BZCY powders by the two methods. The BZCY powder prepared by the SSR process has relatively high filling density; each individual particle is relatively dense and dry pressing of the powder may result in high packing density of green body. In contrast, the BZCY powder derived from a GNP process are highly porous; the pore sizes ranged from tens of nanometers to sub-micrometers. The low filling density of the GNP powders would result in large amount of shrinkage during firing. When used in the anode support, the BZCY powder derived from a GNP process would lead to accelerated densification of the electrolyte during firing; it may help to increase triple phase boundary length of the anode as well.

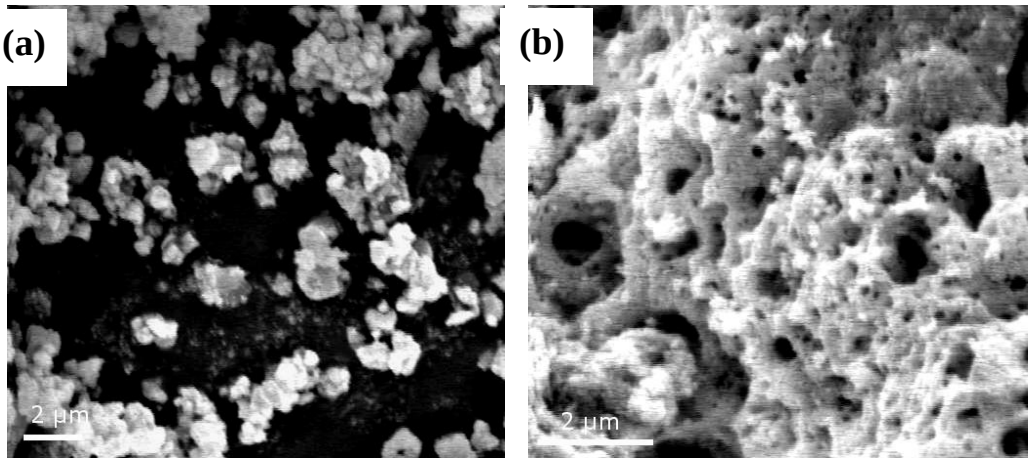

Figure 7-2. Morphologies of BZCY powders prepared by (a) a solid state reaction (b) a glycine nitrate process.

Other combinations of BZCY powders were also examined under identical co-pressing and co-firing conditions. Figure 7-3 (a) shows the cross-sectional morphology of a cell using BZCY-SSR powders in both anode and electrolyte. Obviously, some pinholes were observable in the BZCY electrolyte, due primarily to insufficient shrinkage (~12% in diameter) after sintering. Higher sintering temperature will yield denser electrolyte, but may cause deactivation of the anode. Figure 7-3 (b) shows the microstructures of an anode-supported electrolyte bilayers using only the BZCY powder derived from GNP. It

is seen that the electrolyte film was still porous and remained almost the same even after the sintering temperature was increased to 1400 ^{o}C. Although large surface areas of powders provide increased driving force for densifications, high packing density of green pellet is also essential to decreasing the porosity of sintered body. The foam structure of BZCY-GNP is probably difficult to eliminate closed pores. In contrast, when the BZCY powder derived from GNP was used for the Ni-BZCY anode while that from SSR for the BZCY electrolyte, the electrolyte film is very dense and well-adhered to the porous anode substrate. The use of foam BZCY powder derived from GNP in the anode greatly facilitated the sintering of the electrolyte layer, reaching a linear shrinkage of ~18%.

When powders derived form a GNP process is used for dry pressing of the electrolyte film, it is relatively easy to form a uniform electrolyte layer because of the relatively low filling density of GNP powders (or large volume of the powder). Since the filling density of the BZCY powder prepared by a SSR process is relatively high, however, the volume of the powder for a 20 μm thick electrolyte film is very small, making it very difficult to uniformly distribute the powder on the green anode substrate. As a result, variation in thickness of the BZCY layer is relatively large. In some areas, the electrolyte is so thin to result in short circuiting of the cell. To overcome this difficulty, we used a screen to carefully improve the uniformity of the SSR powder distribution onto the anode substrate. This modified co-pressing allows us to fabricate crack-free films with ~20 μm of thickness even from commercially available powders with relatively large particle size, as shown in figure 7-3 (c).

In addition to achieving uniform and dense BZCY electrolyte film, optimization of the anode microstructure is also important to enhancing fuel cell performance. For example, pore formers are often added in anode processing to create path of gas transport. Figure 7-3 (c) and (d) compare the morphologies of two cells using 10 and 20 wt % starch (pore former) in the NiO-BZCY anode. The anode with 20 wt% starch shows

slightly higher porosity. After reduction in H_2, however, cracks were formed near the interface in addition to numerous inhomogeneous pores, as shown in figure 7-3 (e). These are due probably to the large and non-uniform shrinkage of anode. In contrast, the sample with 10 wt% starch in the anode showed a more uniform microstructure, better connectivity, and stronger bonding between the anodes and the electrolyte bilayers (figure 7-3 (f)).

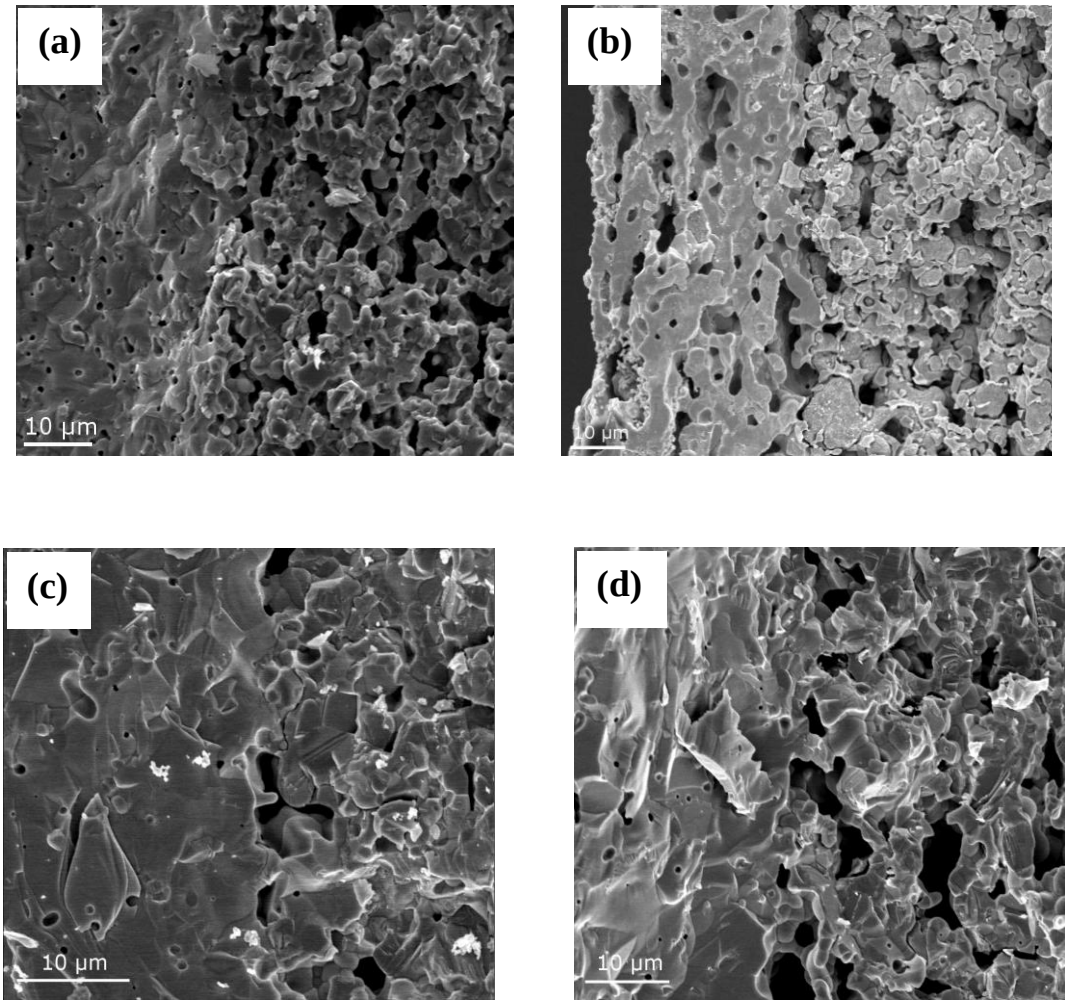

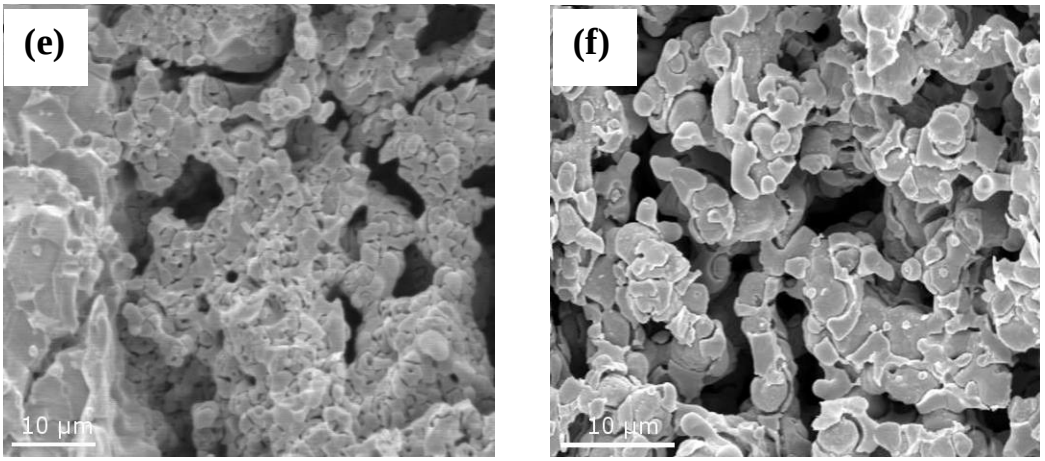

Figure 7-3 Cross-sectional views of anode/electrolyte bilayers. I. Before reduction (a) SSR/SSR (b) GNP/GNP (c) GNP/SSR with 10 wt% starch (d) GNP/SSR with 20 wt% starch. II. After reduction: (e) GNP/SSR with 20 wt% starch (f) GNP/SSR with 10 wt% starch. The left and right layers are electrolyte and anode, respectively.

Figure 7-4 shows the current-voltage characteristics and the corresponding power densities for 2 cells prepared by the co-pressing and co-firing process using BZCY electrolyte powders derived from two different processes: SSR/SSR and GNP/SSR cells with BZCY electrolyte film of ~20 µm thick. The open circuit voltages (OCV) of the two cells are similar (both above 1.0 V), an indication of sufficiently dense electrolytes. However, much higher peak power densities was observed for the GNP/SSR cell, reaching 780 and 490 mW/cm^2 at 700 and 600 ^{o}C, respectively. The SSR/SSR cell produced only ~379 and 160 mW/cm^2 under the same testing conditions. The relatively poor performance of the SSR/SSR cell is attributed to the large amount of closed pores in the electrolyte, which significantly reduced the conductivity of the electrolyte. The undesired microstructure also resulted in higher electrode polarization resistances because of the sluggish transfer of ions across the electrode/electrolyte interface.

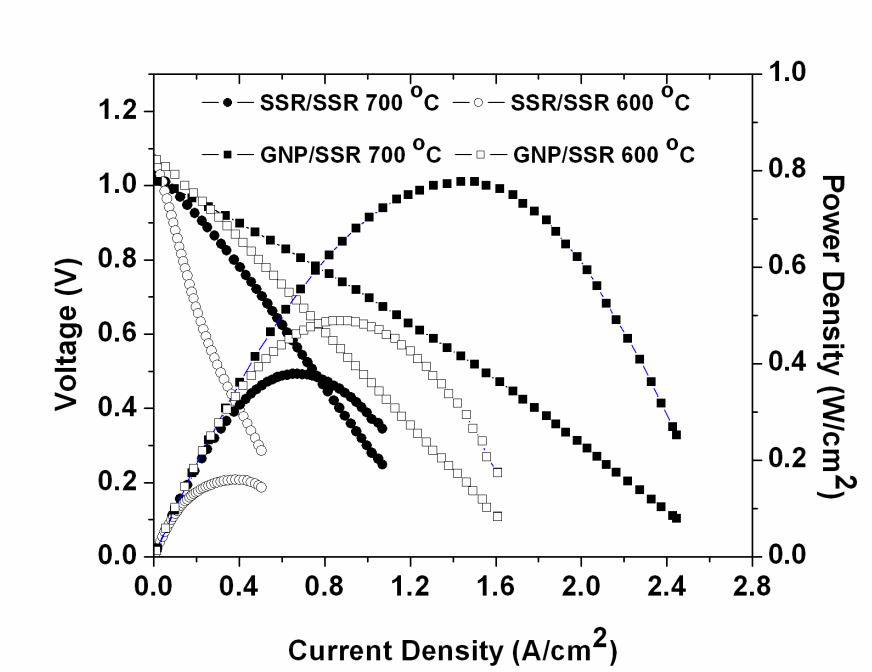

Figure 7-4 Terminal voltage and power density as a function of current density for GNP/SSR and SSR/SSR cells when ambient air was used as oxidant and hydrogen (with ~3 v% H_2O) as fuel. Cathode is BZCY-SSC composite.

Figure 7-5 shows the conductivities of BZCY pellets and anode-supported BZCY films measured in wet H_2 and under fuel cell operation conditions. The BZCY pellets were sintered at 1350 and 1550 ^oC for 10 h, whereas the BZCY electrolyte films in SSR/SSR and GNP/SSR cells were fired at 1350 ^oC for 6 h. Obviously, the BZCY electrolyte film in a GNP/SSR cell exhibited a conductivity of 0.025 S/cm at 700 ^oC, much greater than the conductivities of the BZCY electrolyte film in a SSR/SSR cell or the BZCY pellets fired at 1350 ^oC for 10 h. These large differences in conductivity are attributed to the high porosity of the electrolyte samples. The conductivity of the BZCY film in the SSR/GNP cell is comparable to those of the BZCY pellets fired at 1550 ^oC for 10 h, suggesting that the anode substrate containing foam BZCY powder derived from

GNP dramatically reduced the sintering temperature of BZCY electrolyte containing SSR powders.

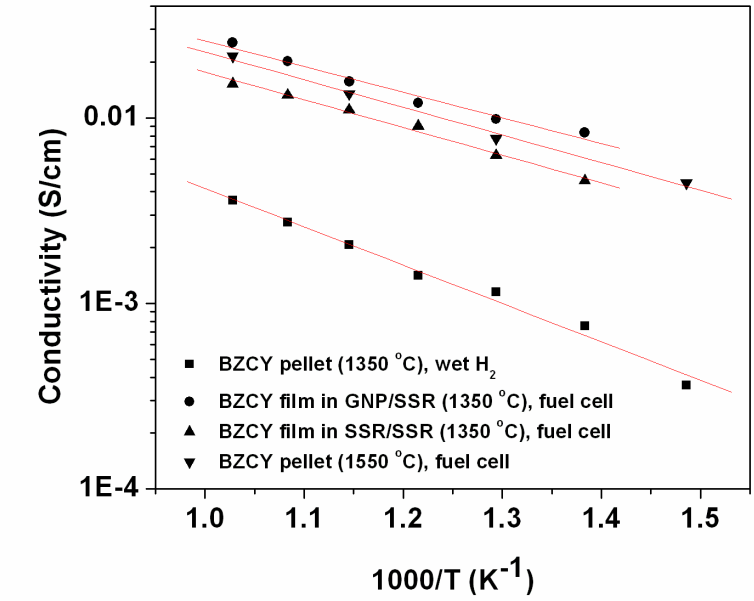

Figure 7-5 Conductivities of BZCY pellets sintered at 1550 and 1350 ^{o}C for 10 h and the BZCY electrolyte films in a SSR/SSR and a GNP/SSR cell fired at 1350 ^{o}C for 6 h.

The present study demonstrated that a dense and uniform BZCY electrolyte film (~20μm) was fabricated on a porous anode support at a relatively low temperature by a modified co-pressing, co-firing process using BZCY powders with different characteristics. The conductivities of the BZCY electrolyte film in an anode-supported cell (fired at 1350 ^{o}C for 6 h) are comparable to those of BZCY pellets (sintered at 1550 ^{o}C for 10 h). Single cells based on anode-supported BZCY electrolyte films demonstrated much-improved power output, achieving peak power densities of ~780 and ~490 mW/cm^2 at 700 and 600 ^{o}C, respectively.

7.3 Oxygen reduction reaction on composite cathode

The oxygen reduction reaction on a cathode of SOFCs based on oxygen ion conductors has been extensively studied [93-97]. It is well known that mixed ionic and electronic conducting (MIEC) cathode on an oxygen ion conducting electrolyte could expand the electrochemically active reaction sites from the triple phase boundary (TPB) to the cathode surface, as shown in Figure 7-6 (a). However, when applying an MIEC on a proton conducting electrolyte, the oxygen reduction can only take place at the interface where electrode, electrolyte, and the gas phase are in contact and where the access to oxygen, proton, and electrons are met for the reduction reaction as indicated in Figure 7-6 (b). The limited reaction sites may lead to large electrode polarization resistance. This could explain why pure SSC cathode exhibits poor electrochemical performance (an overpotential of 350 mV at a current density of 100 mA/cm^2 at 600 ^oC) on Y-doped barium cerate electrolyte[32]. In order to expand reaction zone beyond the interface, a potential cathode material must be able to conduct proton, oxygen ions and electrons. A mixed proton, oxide ion and electron conducting cathode extends the TPB from the interface to the entire cathode, thereby greatly accelerating the charge transfer reaction. From these points of view, a fuel cell based on proton conducting electrolyte using this mixed conducting cathode should reduce the resistance to oxygen reduction reactions. Unfortunately, a single-phase proton, oxygen ion and electron conductor with significant electronic conductivity is not yet to be developed [98]. Thus, a composite cathode consisting of a proton conductor and a mixed oxygen ion and electron conductor (MIEC) may facilitate simultaneous transport of proton, oxide ion, and electron for the oxygen reduction, as schematically shown in Figure 7-6 (c). The other advantage of this concept is that well-developed MIECs can be mixed with a proton conductor to tailor the properties. In this study, LSCF was mixed with BZCY to form a composite cathode that

transport proton, oxide ion, and electron, exhibiting very low polarization resistance and high power density.

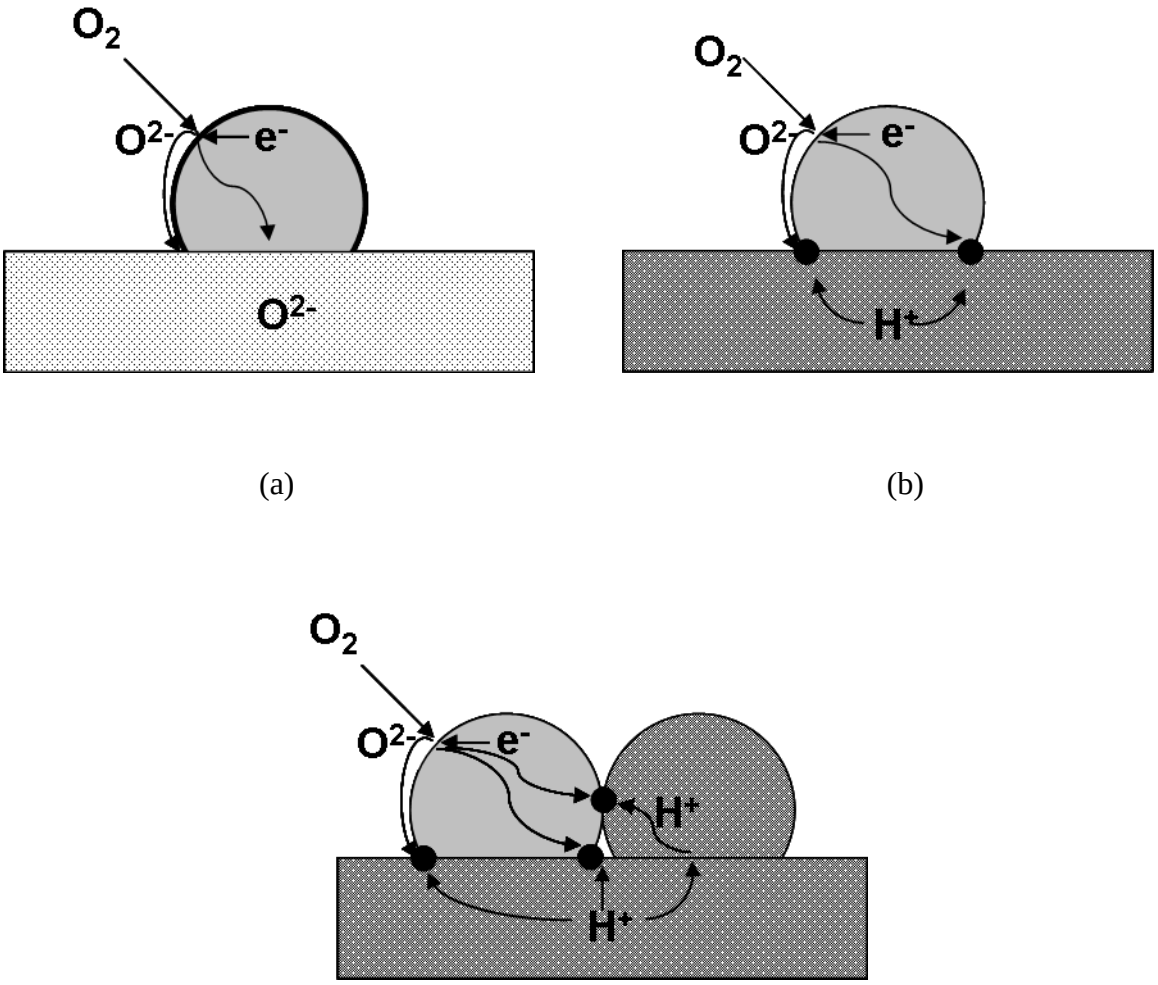

Figure 7-6 Schematic illustration of oxygen reduction reaction sites (a) a mixed oxygen ion-electron conducting cathode on oxygen ion conducting electrolyte, (b) a mixed oxygen ion-electron conducting cathode on a proton conducting electrolyte, and (c) a mixed proton-oxygen ion-electron conducting cathode on a proton conducting electrolyte. The circles denote electrochemically active reaction sites.

7.4 $Ba(Zr_{0.1}Ce_{0.7}Y_{0.2})O_{3-\delta}$ –$La_{0.6}Sr_{0.4}Co_{0.2}Fe_{0.8}O_{3-\delta}$ composite cathode

The pairing of proton conducting electrolytes with proper electrode materials is significant to achieving high performance SOFCs. Shown in Figure 7-7 are some typical X-ray diffraction patterns for BZCY, LSCF, and BZCY-LSCF powder mixtures taken before and after firing at 1000-1200^{o}C for 10 h. As can be seen, no obvious secondary phase appears in the BZCY-LSCF system when the firing temperature is 1100 ^{o}C. Further, the linear thermal expansion coefficient of BZCY (11.2×10^{-6} K^{-1}) is similar to that of LSCF (15.3×10^{-6} K^{-1}) [99, 100]. Thus, LSCF is a chemically and thermally compatible with BZCY electrolyte under the conditions studied.

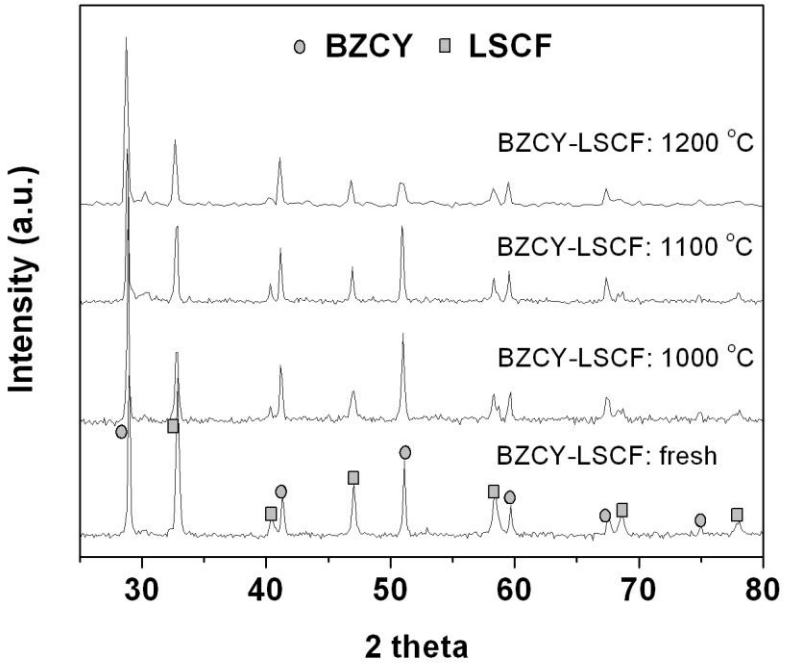

Figure 7-7 Typical XRD patterns of BZCY, LSCF, and BZCY-LSCF mixture before and after firing at 1000-1200 ^{o}C for 10 h.

Figure 7-8 shows the dependence of cell voltages and power densities on cell operating current densities at different temperatures for BZCY-based fuel cells using

BZCY-LSCF and LSCF cathodes. The open circle voltages (OCV) at 750, 650, and 550^{o}C are 1.01, 1.06, and 1.11V, respectively. This indicates that the BZCY electrolyte is sufficiently dense and exhibits negligibly small electronic conduction. More importantly, BZCY-LSCF composite cathode produced much higher power output than the LSCF cathode under the same operating conditions. The peak power densities were ~855, 522, and 215 mW/cm^2 at 750, 650, and 550^{o}C, respectively. These performances are surprisingly high for a cell based on a 55 μm thick electrolyte, even better than that based on an oxygen ion conductor (e.g., 26μm -thick GDC electrolyte and GDC-SSC cathode showed 330 and 205 mW/cm^2 at 650 and 550 ^{o}C, respectively) [101]. In contrast, the cell with the LSCF cathode displayed 435, 235, and 81 mW/cm^2 at 750, 650, and 550^{o}C, respectively.

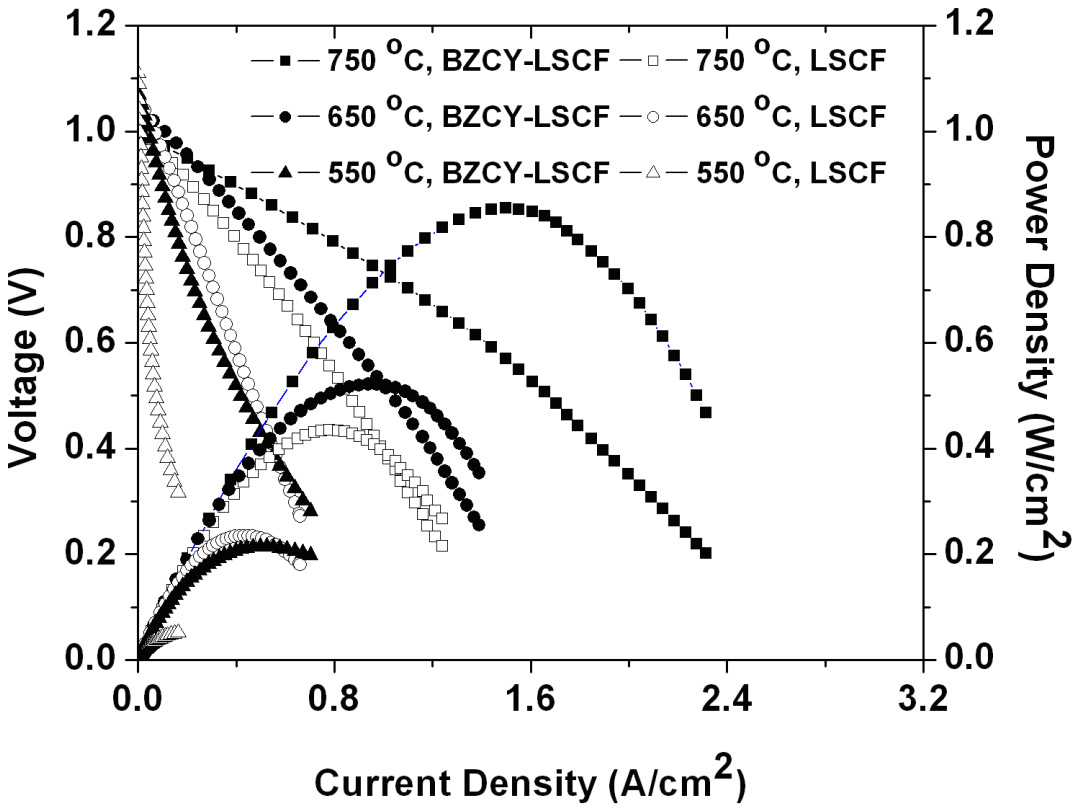

Figure 7-8 V-I characteristics for BZCY based anode-supported cells with BZCY-LSCF and LSCF cathodes as measured in humidified (3% H_2O) H_2 at 550 -750 ^{o}C

Figure 7-9 summarizes the polarization resistances of typical cells with BZCY-LSCF and LSCF cathodes measured at different temperatures. Obviously, BZCY-LSCF exhibits much lower cathodic polarization resistances than the LSCF cathode in all cases. The polarization resistances of cells with BZCY-LSCF are estimated to be only 0.19, 0.47, and 1.34 Ω cm^2 at 650, 600, and 550^{o}C, respectively, comparable to those of the GDC-LSCF composite cathode on GDC electrolyte (0.13, 0.33, and 1.24 Ω cm^2 at 650, 600, and 550 ^{o}C, respectively), as shown in figure 7-10 [102]. SEM examination of fresh BZCY-LSCF and LSCF cathodes reveals that their surface and cross-sectional morphologies are very similar, suggesting that the remarkable improvement in performance is due primarily to the superior catalytic activity of BZCY-LSCF cathode.

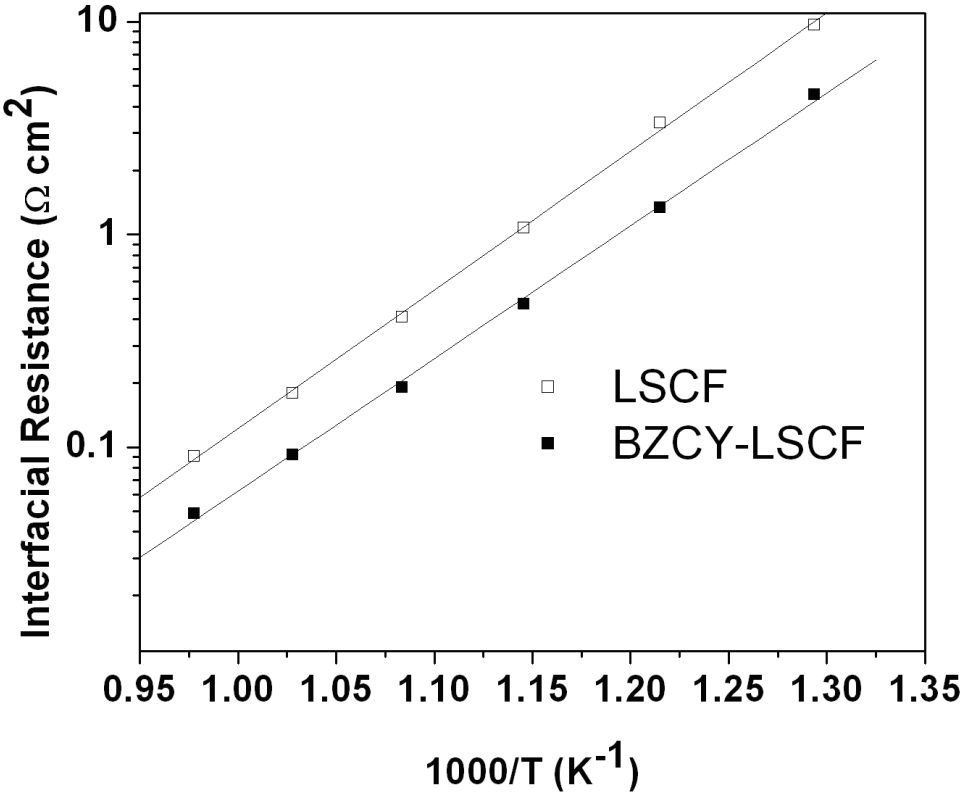

Figure 7-9 polarization resistances of the cells with LSCF and BZCY-LSCF cathode

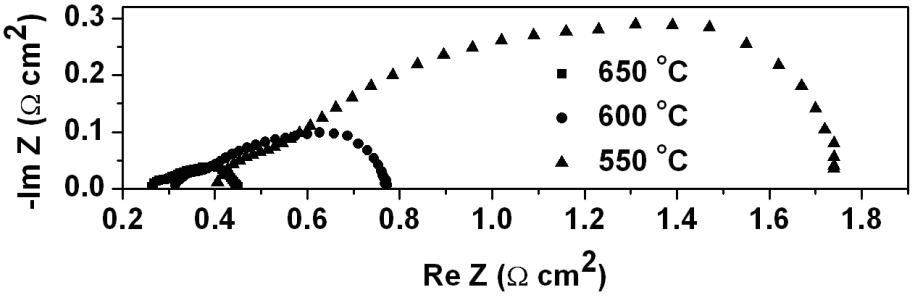

Figure 7-10 Impedance spectra of a single cell with BZCY-LSCF cathode measured under open circuit conditions at different temperatures.

It is critical to evaluate durability of the cells with BZCY electrolyte and BZCY-LSCF cathode. Any instability of BZCY at high water activities and deterioration of electrode may lead to degradation in fuel cell performance. Figure 7-11 shows the performance of cells operated at 600 mA/cm^2 & 750^{o}C and at 0.7 V & 600 ^{o}C. The cell voltage and current density were relatively stable and there was no obvious degradation in performance at both high and low temperatures, implying superior chemical stability of BZCY, steady electric characteristics of electrode, and strong bonding between electrolyte and electrode, as shown in figure 7-12.

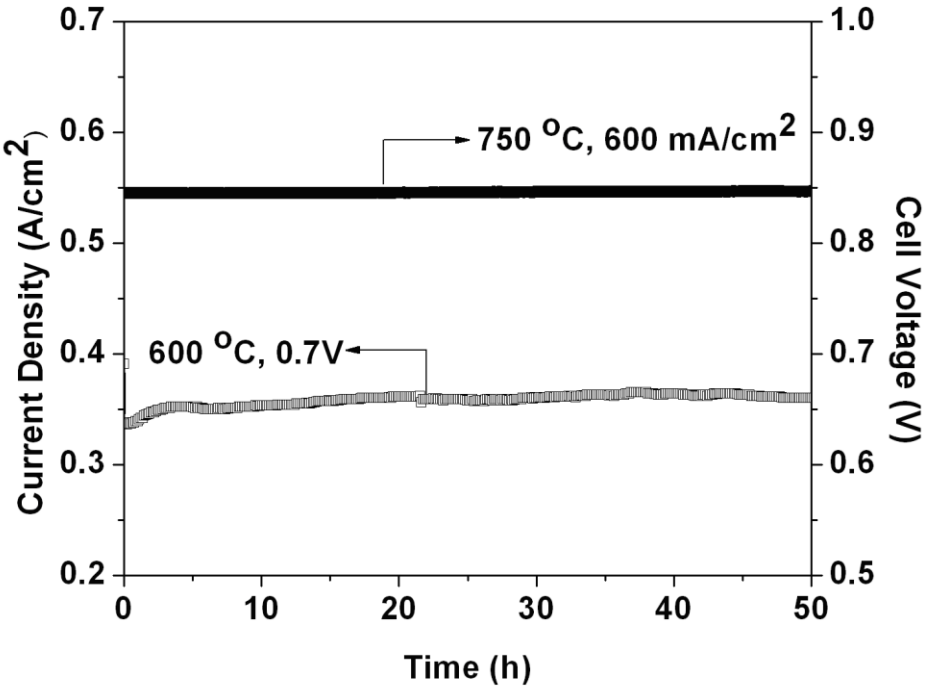

Figure 7-11 Performances of the cells with BZCY electrolyte and BZCY-LSCF cathode tested at a constant current density of 600 mA/cm^2 at 750^{o}C and at a constant cell voltage of 0.7 V at 600^{o}C

SOFCs based on oxide proton conductor BZCY electrolyte and BZCY-LSCF composite cathode have produced high and steady power densities at reduced temperatures. The mixed conducting composite cathode demonstrated much-improved catalytic activity toward oxygen reduction than LSCF cathode. It appears that the addition of BZCY considerably increases the number of electrochemical reaction sites and expands them from the electrode/electrolyte interface to the entire surface of cathode. Moreover, LSCF is chemically compatible with BZCY even when firing at 1100^{o}C for 10 h, leading to both phase stability and superior adhesion with electrolyte. The preliminary durability testing indicated the practical viability of this promising composite cathode.

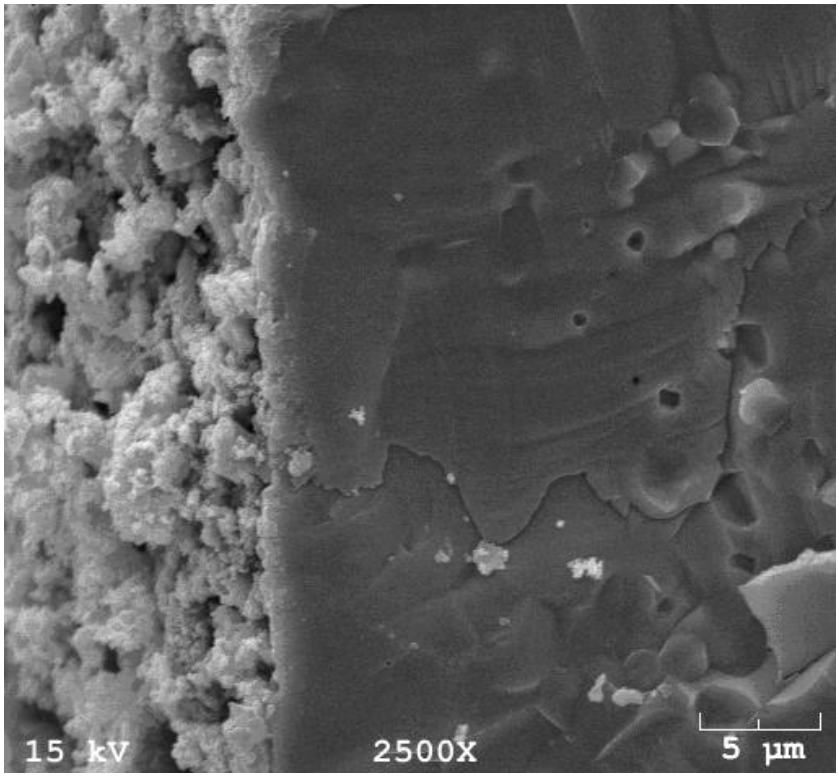

Figure 7-12 A cross sectional view of the porous BZCY-LSCF cathode after operation at 600 mA/cm^2 & 750^{o}C and 0.7 V & 600 ^{o}C for 100 h.

7.5 $Ba(Zr_{0.1}Ce_{0.7}Y_{0.2})O_{3-\delta}$ –$Sm_{0.5}Sr_{0.5}CoO_{3-\delta}$ composite cathode

The pairing of oxide proton conducting electrolytes with chemically compatible electrode materials is very important to the performance of SOFCs. To investigate the compatibility between BZCY and SSC, a mixture of BZCY and SSC powders (weight ratio of 2:3) was fired at different temperatures. Shown in Figure 7-13 are the X-ray diffraction (XRD) patterns of a BZCY-SSC mixture before and after calcination at 900, 1000, and 1100^{o}C. The XRD data suggests that there were no observable chemical reactions between SSC and BZCY when fired at 900^{o}C for 3 h. However, new phases other than BZCY and SSC were formed when the calcination temperature was increased to 1000 and 1100^{o}C. Additional phases such as $BaCoO_3$ and $Sm_2Zr_2O_7$ were identified in

the XRD patterns. The $BaCoO_3$ based phase is an excellent mixed conductor with high oxygen ion and electronic conductivity [103] whereas the $Sm_2Zr_2O_7$ phase is a proton conductor with relatively high proton conductivity.[18] This implies that firing of the BZCY-SSC composite cathode onto an BZCY electrolyte at proper temperatures could produce desirable phases for oxygen reduction in addition to forming strong bonding between the electrolyte and cathode. When the firing temperature was too high (at 1100^{o}C), however, large amounts of $Sm_2Zr_2O_7$ phase were formed, which has low electronic conductivity and could lead to high sheet resistance when used as a cathode. More importantly, it is evident that the peaks corresponding to BZCY were shifted to right, especially at high angles of diffraction after firing at 1000 and 1100^{o}C, suggesting that Co might have doped into the B-site of BZCY,[31] since Co^{3+} (R^{III}=0.53 Å) is smaller than Ce^{4+} (R^{IV}=0.87 Å) and Zr^{4+} (R^{IV}=0.72 Å). Further, conductivity measurements under various conditions indicate that the Co-doped BZCY is an excellent mixed proton-electronic conductor, transporting both proton (H^+) and electronic defects (e^- and/or $h^\bullet$), and thus is an active phase for oxygen reduction. [31]Thus, when properly fired, the entire surface of the BZCY-SSC cathode could become active for oxygen reduction since each of the major phases is in fact a mixed conductor, dramatically reducing the cathodic polarization resistance due to oxygen reduction.

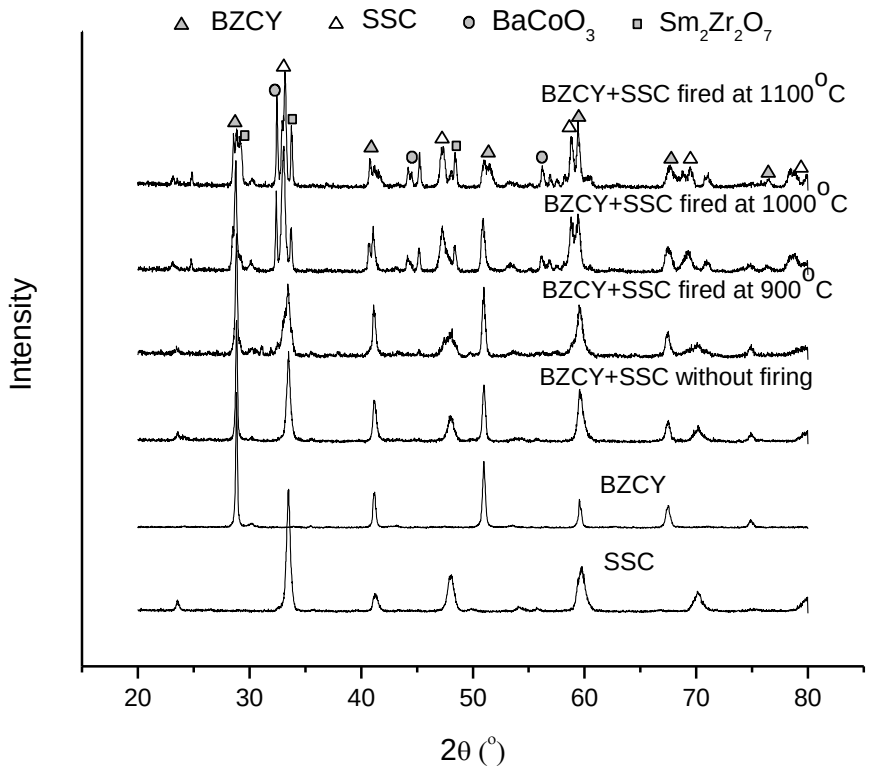

Figure 7-13 XRD patterns of BZCY, SSC, and BZCY-SSC mixtures before and after calcinations at 900, 1000, and 1100 ^{o}C for 3 h.

Figure 7-14 shows the morphologies of BZCY-SSC surfaces and the interfaces between electrolyte and cathode fired at 900, 1000, and 1100^{o}C. For the samples fired at 900^{o}C, the adhesion of the electrode to the electrolyte is relatively poor. The connectivity between particles within the cathode is insufficient for the transport of ions and electrons required for cathode reactions. For the BZCY-SSC cathode fired at 1000^{o}C, in contrast, the adhesion of the electrode to the electrolyte is significantly improved. The inter-particle connectivity is also much better, producing a uniform and porous structure. Further, because of the chemical interactions between BZCY and SSC at 1000^{o}C, the cathode was then composed of two major phases, Co-doped BZCY and SSC (each being a mixed ionic-electronic conductor), and some minor phases such as $BaCoO_3$ (mixed

conductor) and $Sm_2Zr_2O_7$ (proton conductor). However, when the firing temperature of BZCY-SSC was increased to 1100^{o}C, the cathode was over-densified, leading to a dramatic loss of porosity and an increase in concentration polarization of the cathode. Further, the formation of excessive amounts of less conductive phases (such as $Sm_2Zr_2O_7$) resulted in poor performance.

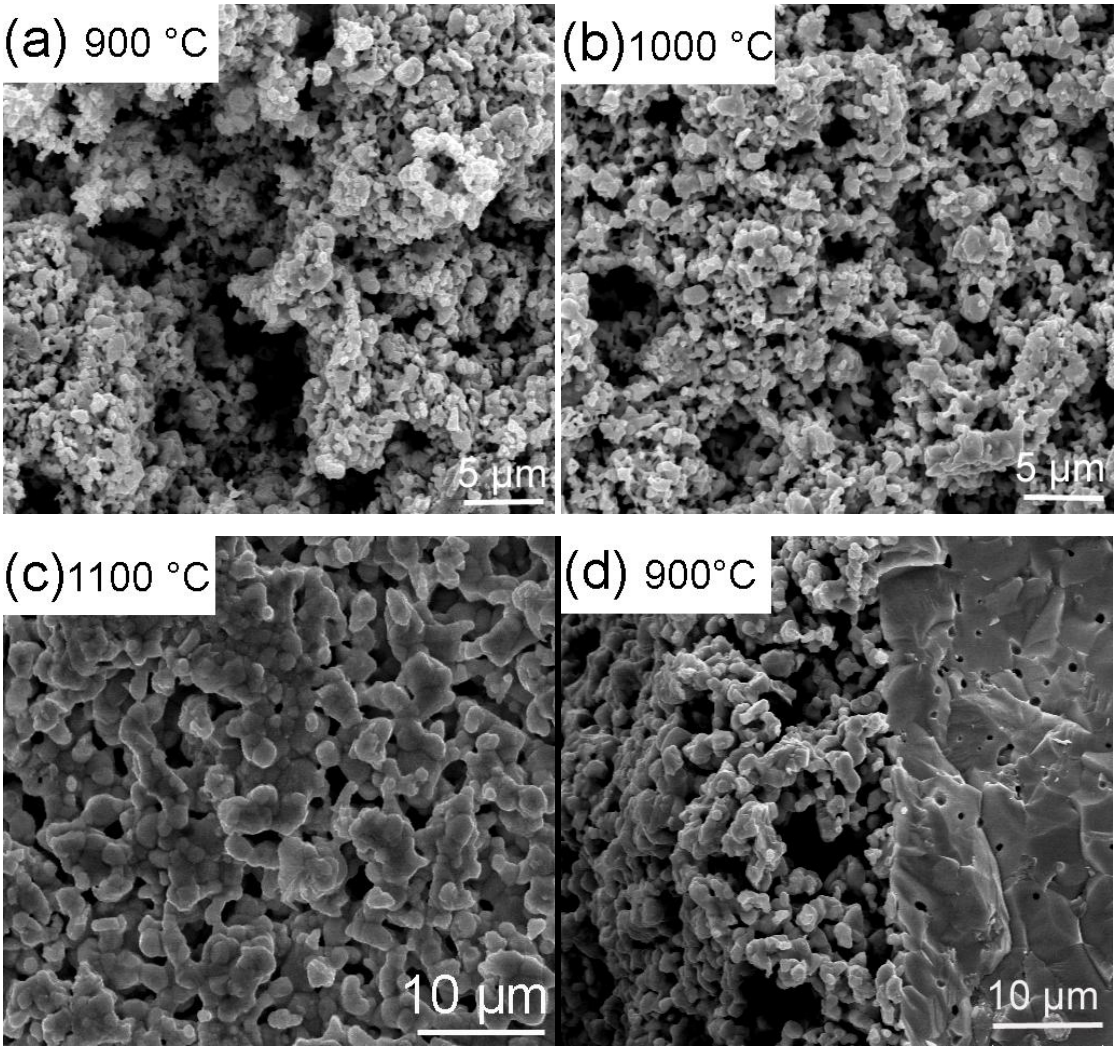

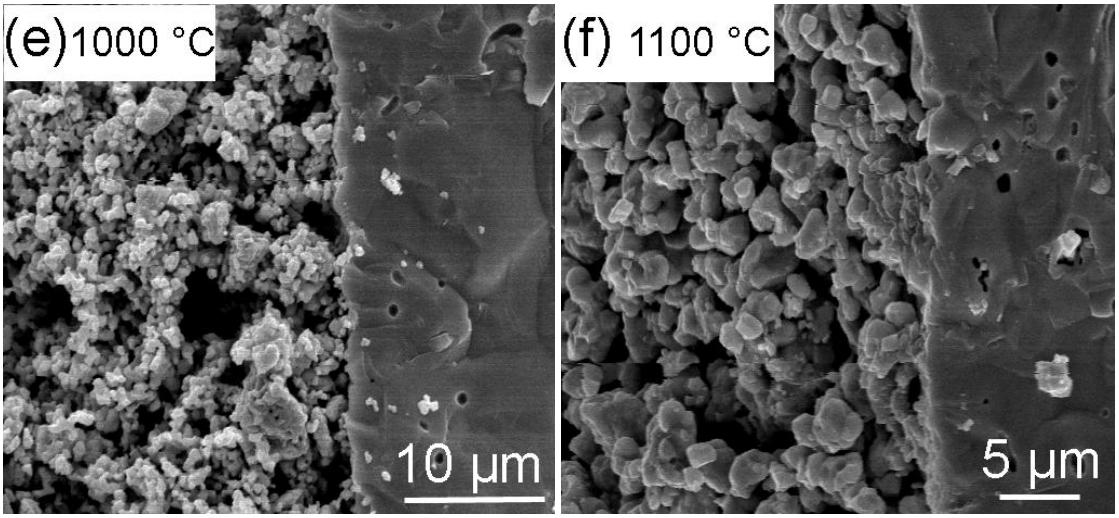

Figure 7-14 Surface and cross-sectional views (SEM images) of BZCY-SSC cathode and the interface between BZCY electrolyte and the composite cathode fired at (a, d) 900, (b, e) 1000 and (c, f) 1100 ^{o}C

The electrochemical performances of the cells based on a BZCY electrolyte and BZCY-SSC cathodes fired at 900, 1000, and 1100^{o}C were characterized under various fuel cell operating conditions. Shown in Figure 7-15 are the current-voltage characteristics and the corresponding power densities at different temperatures for a fuel cell based on a BZCY electrolyte membrane of 65 μm thick and BZCY-SSC composite cathode fired at 1000^{o}C. The open circuit voltages (OCV) at 700, 600 and 500^{o}C were 1.00, 1.05 and 1.08V, respectively, indicating that the BZCY electrolyte was sufficiently dense and exhibited negligible electronic conduction. The peak power densities are about 725, 598, 445, 272 mW cm^{-2} at 700, 650, 600 and 550^{o}C, respectively. The observed current and power densities represent the highest performance ever reported in the literature for SOFCs based on an oxide proton conductor, even higher than the conventional oxygen ion conducting cells based on 20 μm-thick GDC and GDC-SSC cathode.[104] The observed fuel cell performances are very encouraging, especially for operation at low temperatures to dramatically reduce the cost of SOFC systems.

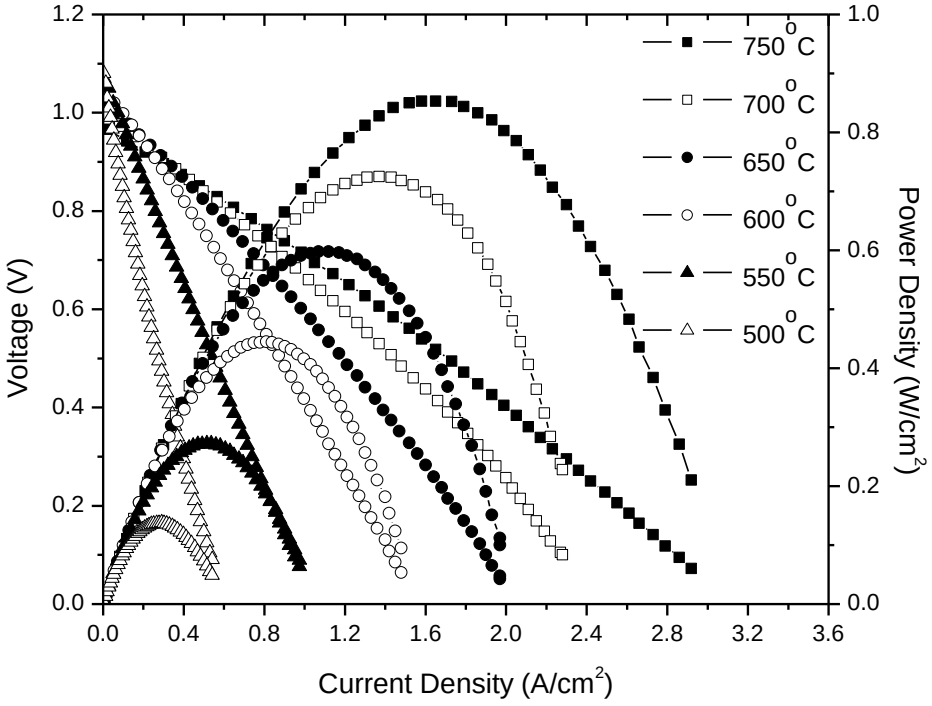

Figure 7-15 Cell voltages and power densities as a function of current density for fuel cells consisting of Ni-BZCY anode, 65 μm-thick BZCY electrolyte, and BZCY-SSC cathode fired at 1000^{o}C.

Shown in Figure 7-16 are the current densities measured at a cell voltage of 700 mV at different testing temperatures for cells with BZCY-SSC cathode fired at 900, 1000, and 1100^{o}C. The cathode fired at 1000^{o}C displayed the best performance. For the cell with BZCY-SSC cathode fired at 900^{o}C, the peak power density of the cell reduced to about 248, 151, 81, and 45 mW cm^{-2} at 700, 650, 600, and 550^{o}C, respectively. Similarly, when the cathode was fired at 1100^{o}C, the peak power density dropped to 423, 265, 153, and 66 mW cm^{-2} at 700, 650, 600, and 550^{o}C, respectively.

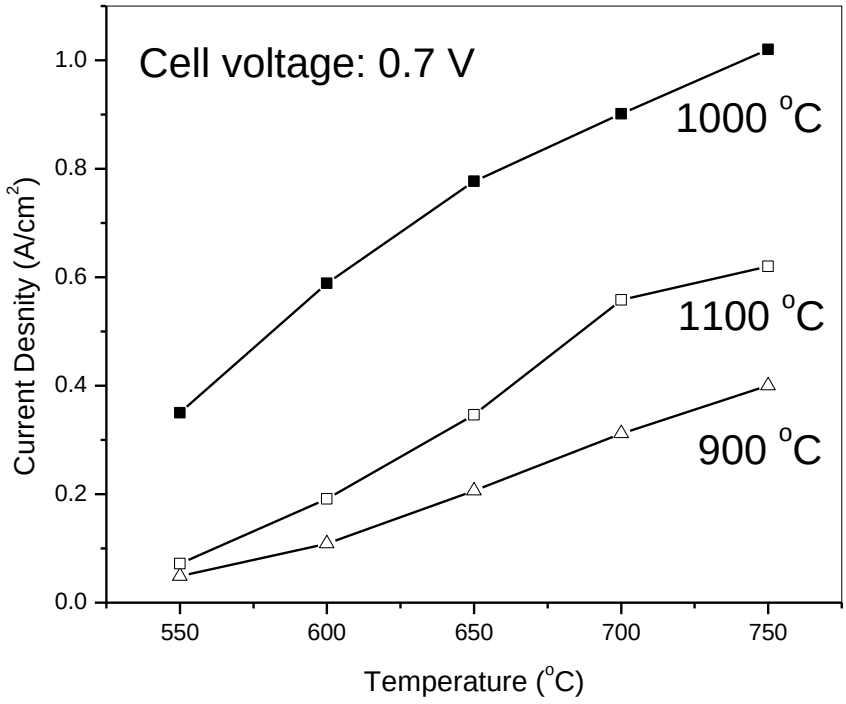

Figure 7-16 Current densities measured at a cell voltage of 0.7 V at different temperatures for the cells with BZCY-SSC cathode fired at 900, 1000, and 1100°C.

Shown in Figure 7-17 are the polarization resistances of Ni-BZCY/BZCY/BZCY-SSC cells with the BZCY-SSC cathodes fired at 900, 1000, and 1100°C, as compared with a similar cell using $BaCe_{0.4}Pr_{0.4}Y_{0.2}O_3$ (BCPY) as the cathode. These polarization resistances were determined from impedance spectroscopy under open circuit conditions. As expected, the cell with BZCY-SSC cathode fired at 1000°C showed the lowest interfacial resistances. At 600 and 550°C, the interfacial resistances are estimated to be about 0.168 and 0.501 Ω cm^2, respectively, comparable to the lowest cathodic interfacial resistance of the GDC-SSC composite cathode on an GDC electrolyte.[104]

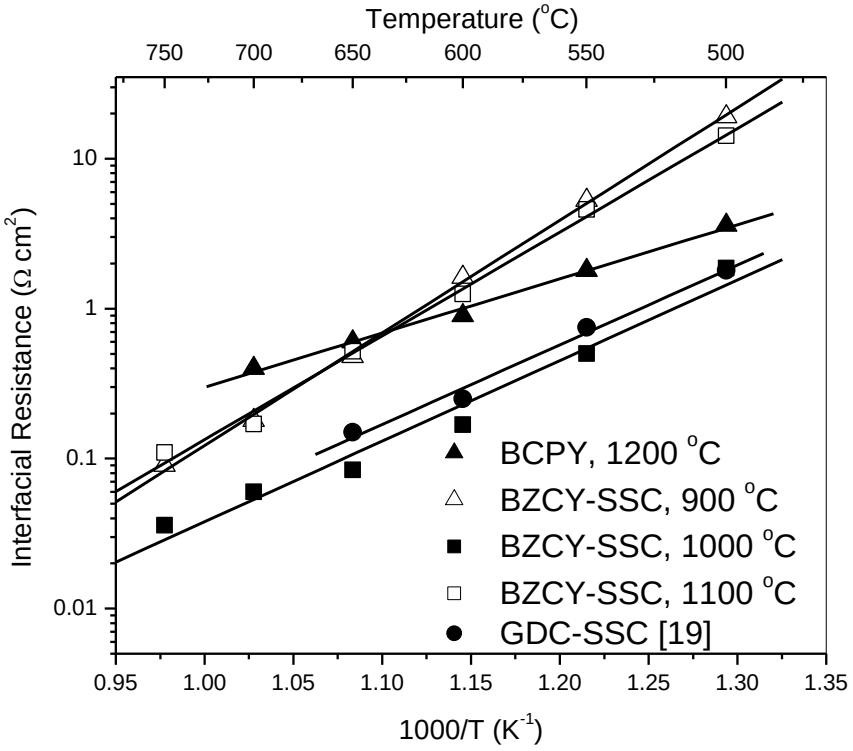

Figure 7-17 Polarization resistances between BZCY and different cathodes as determined from impedance spectroscopy under open circuit conditions: BZCY/BCPY, BZCY/BZCY-SSC (fired at 900 ^{o}C), BZCY/BZCY-SSC (fired at 1000 ^{o}C), and BZCY/BZCY-SSC (fired at 1100 ^{o}C). The cathodic interfacial resistance of GDC-SSC is from ref.[104].

7.6 Cobalt-doped $BaZr_{0.1}Ce_{0.7}Y_{0.2}O_{3-\delta}$ cathode

Shown in Figure 7-18 are X-ray diffraction patterns of $BaZr_{0.1}Ce_{0.7}Y_{0.2-x}Co_xO_{3-\delta}$ (x=0, 0.05, 0.075, 0.1 and 0.2) samples. It is easily seen that no obvious secondary phase was found in BZCY with up to 7.5mol% of Co content. In addition, the diffraction peaks associated with BZCY phase shifted towards higher angle. The shift is probably a result of smaller ionic radius of Co^{3+} (R^{III}=0.53 Å) than Ce^{4+} (R^{IV}=0.87 Å) and Zr^{4+} (R^{IV}=0.72

Å) [37]. With the increase of Co dopant to 10mol%, $BaCoO_3$-based phase was shown in the XRD pattern and appeared more when 20 mol% Co was doped in B-site. This trend indicates that cobalt formed solid solution in the range of less than 7.5mol%; further introduction of cobalt resulted in the dissolution of Co from BZCY.

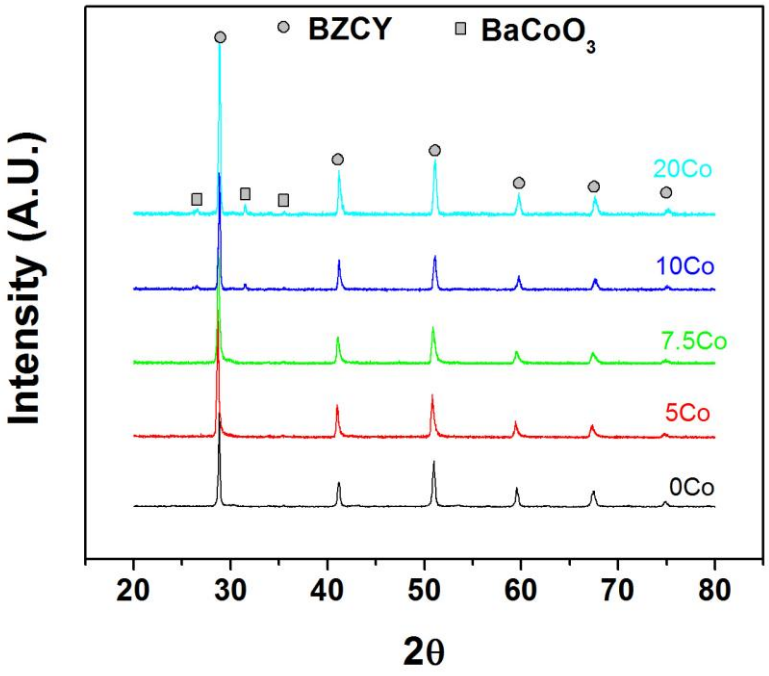

Figure 7-18 XRD patterns of various Co-doped BZCY powders

Since cathode is exposed in air or oxygen, it is necessary to investigate the conductivity of various Co-doped BZCY pellets under these conditions. In fact, electrical conductivities of cerate and zirconate are sensitive to partial pressure of oxygen, hydrogen, and water. $BaZr_xCe_{1-x}O_3$ compounds when doped, typically on the B-site by a lower-valent cation, become oxygen-deficient. The dopant dissolution mechanism leads to the creation of oxygen vacancies as per Equation 7-1 and 7-2 (written in Kroger-Vink notation).

$$2Ce_{Ce}^{X} + O_{O}^{X} + Y_2O_3 \Leftrightarrow 2Y_{Ce}^{/} + V_{O}^{\bullet\bullet} + 2CeO_2 \qquad (7\text{-}1)$$

$$2Zr_{Zr}^{X} + O_{O}^{X} + Y_2O_3 \Leftrightarrow 2Y_{Zr}^{/} + V_{O}^{\bullet\bullet} + 2ZrO_2 \quad (7\text{-}2)$$

Subsequent exposure to humid atmospheres is presumed to lead to the incorporation of protons into the lattice according to Equation 7-3.

$$H_2O(g) + V_{O}^{\bullet\bullet} + O_{O}^{X} \Leftrightarrow 2OH_{O}^{\bullet} \quad (7\text{-}3)$$

The defect reaction for oxygen incorporation into the lattice (absorption) in dry atmospheres can be written as

$$\frac{1}{2}O_{2(g)} + V_{O}^{\bullet\bullet} \Leftrightarrow O_{O}^{X} + 2h^{\bullet} \quad (7\text{-}4)$$

This promotes electronic (p-type) conduction, accompanied by consumption of oxygen vacancies at elevated temperatures. However, the electronic conductivity is insufficient for cathode reactions. Transition metal ions are essential to be doped in the B-site to further enhance the electronic conductivity. Figure 7-19 represents the conductivities plotted as a function of Co doping concentrations in dry oxygen at 500-700 ^{o}C. It was noted that the total conductivities were reduced with increasing Co content and then increased sharply with the further introduction of Co dopants throughout the testing temperatures. For example, the conductivity decreased from 0.023 S/cm for 0Co to 0.008 S/cm for 5Co and reached maxima of 2.48 S/cm for 20Co at 700 ^{o}C, a sample with complete replacement of Y by Co in B-site. The decrease in conductivity of BZCY after substitution of Y with small amount of cobalt agrees with the prediction of Kilner [105] and with the experimental results of Shimura for $BaCeO_3$ system [46]. This behavior was interpreted by the hole-trapping effect of the transition metal *3d* orbital. The marked increase of conductivity at high doping level was attributed primarily to formation of $BaCoO_3$-based phase that is an excellent conductor with high oxygen ion and electronic conductivity[106].

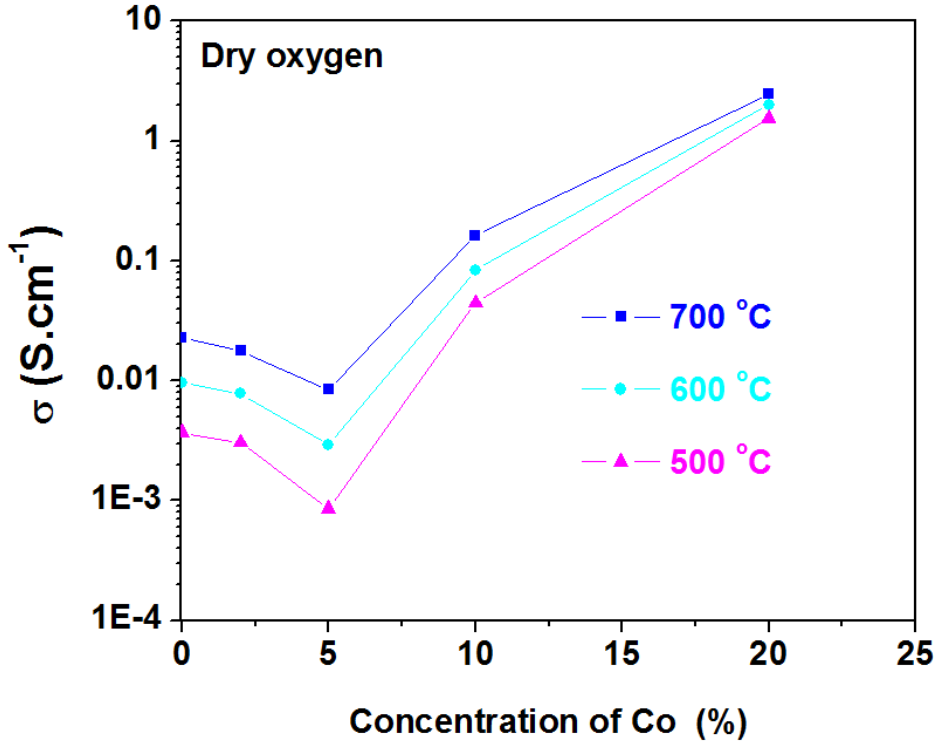

Figure 7-19 Total conductivities of various Co-doped BZCY as a function of the concentration of Co as measured in dry oxygen.

Figure 7-20 displays the apparent activation energies of various samples in dry oxygen, which increased slightly with the Co content initially and reached a maximum value for sample with 5% Co dopant. Then a pronounced decrease in activation energy was observed with addition of Co, suggesting a dramatic change in conduction mechanism. The activation energies for the conductivity of 0Co-5Co are in the range of 60-80 kJ.mol^{-1}, which are typical values for ionic transport. On the other hand, the 20Co sample has activation energy (22 kJ.mol^{-1}) similar to those for doped lanthanum manganite [107], lanthanum cobaltite[108], and $BaCoO_3$[109]. These energy barriers are for transport of electronic defects, suggesting that the conduction in the 20Co sample is dominated by electronic transport.

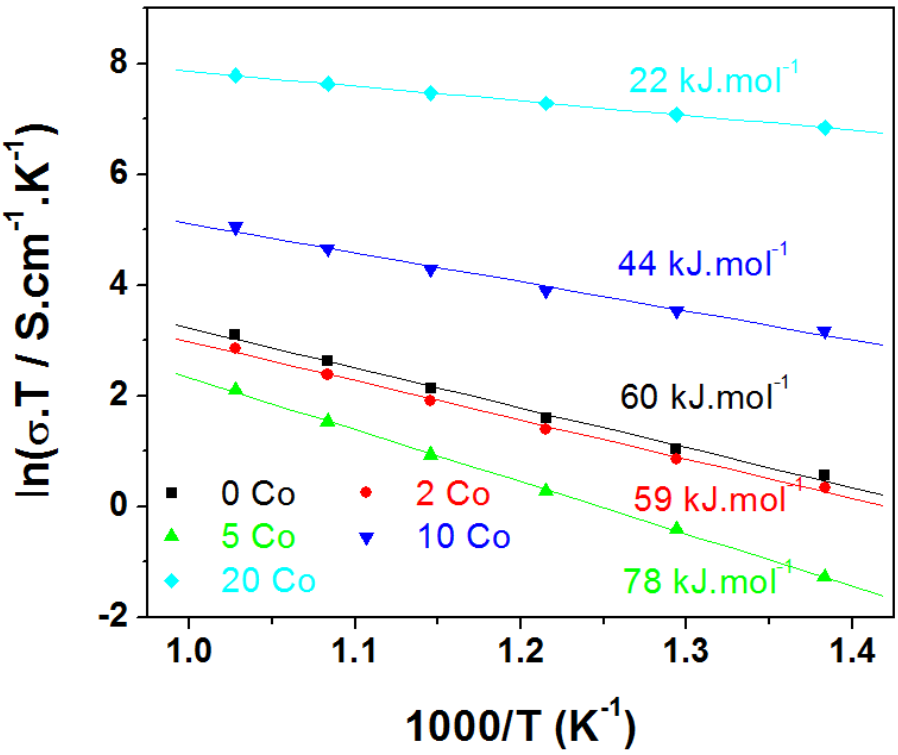

Figure 7-20 Total conductivities in dry oxygen of various Co-doped BZCY as a function of temperature

To evaluate the feasibility of Co-doped BZCY conductor as the cathode, anode-supported cells with thin BZCY electrolyte were fabricated. Figure 7-21 shows the cross-sectional images of as-received $BaZr_{0.1}Ce_{0.7}Co_{0.2}O_{3-\delta}$ (BZCC) cathode. The observed strong interface adhesion indicates that the cathode has the unique compatibility with the electrolyte, primarily because BZCC cathode was derived from the BZCY electrolyte. The excellent bonding would yield sufficient electrochemically active sites and sustained stability under the operating conditions. Furthermore, the inter-particle connectivity in the BZCC cathode was suitable; a porous structure was thus obtained, resulting in facile transport of oxygen gas as well as proton, oxygen ion, and electron required for cathode reactions.

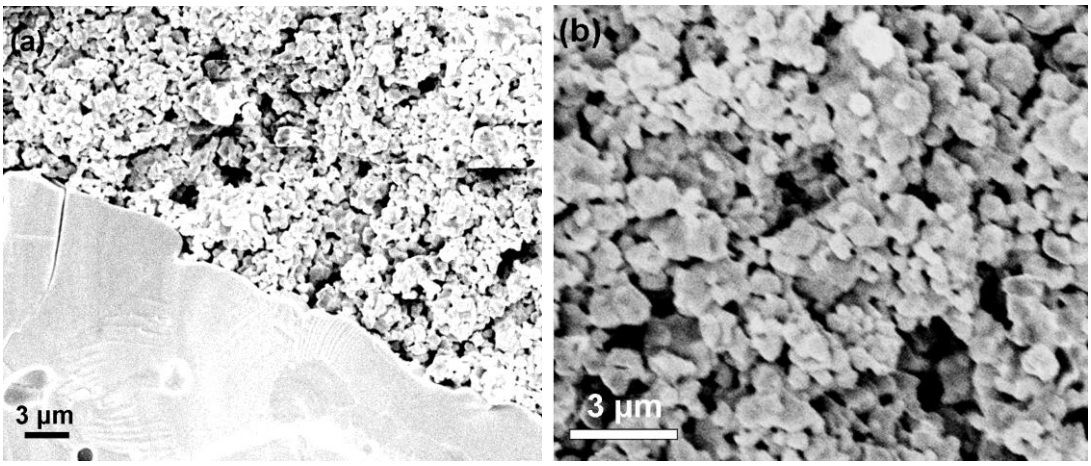

Figure 7-21 Cross-sectional images of BZCC cathode and BZCY electrolyte bilayers (a) interface (b) cathode

Figure 7-22 shows the current-voltage characteristics and the corresponding power densities for BZCY-based fuel cells with $BaZr_{0.1}Ce_{0.7}Co_{0.2}O_{3-\delta}$ (BZCC) and $BaCe_{0.4}Pr_{0.4}Y_{0.2}O_{3-\delta}$ (BCPY) cathodes measured at different temperatures. The open circuit voltages (OCV) at 750, 700, and 650 ^{o}C are 1.00, 1.04, and 1.07V, respectively, representing that the BZCY electrolyte is sufficiently dense and exhibits negligible electronic conduction. The single cell with $BaZr_{0.1}Ce_{0.7}Co_{0.2}O_{3-\delta}$ (BZCC) cathode yielded peak power densities of 0.52, 0.37 and 0.22 W/cm^2 at 750, 700 and 650 ^{o}C, respectively. These power outputs are higher than that of the same cell with $BaCe_{0.4}Pr_{0.4}Y_{0.2}O_{3-\delta}$ (BCPY) cathode, specifically, 0.35, 0.27 and 0.18 W/cm^2 at corresponding temperatures. However, with the Co-doped BZCY cathode in which cobalt content is within the solubility such as $BaZr_{0.1}Ce_{0.7}Y_{0.15}Co_{0.05}O_{3-\delta}$, the cell demonstrated dramatically reduced performance, reaching a peak power density of 0.27 W/cm^2 at 750 ^{o}C. This can be reasonably attributed to the low electronic conductivity of cathodes that inhibited the charge transfer reactions.

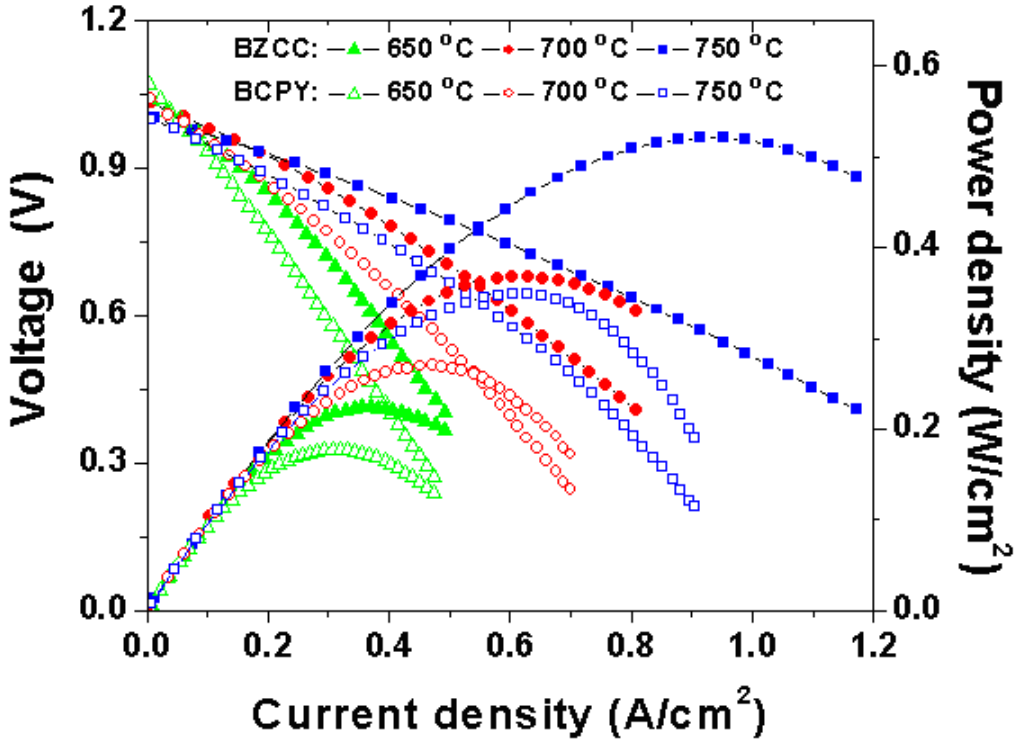

Figure 7-22 Power output characteristics of a typical cell with $BaZr_{0.1}Ce_{0.7}Co_{0.2}O_{3-\delta}$ (BZCC) and $Ba(Ce_{0.4}Pr_{0.4}Y_{0.2})\ O_{3-\delta}$ (BCPY) cathodes at various temperatures.

Moreover, impedance spectroscopy measurements revealed that the cell with $BaZr_{0.1}Ce_{0.7}Co_{0.2}O_{3-\delta}$ produced the interfacial resistances of 0.085, 0.16 and 0.35 $\Omega \cdot cm^2$ at 750, 700 and 650 ^oC, respectively, as shown in figure 7-23. In contrast, at these temperatures, the polarization resistances for the cell with $BaCe_{0.4}Pr_{0.4}Y_{0.2}\ O_{3-\delta}$ are 0.28, 0.41 and 0.61 $\Omega \cdot cm^2$. Therefore, the markedly increased electrocatalytic activity of $BaZr_{0.1}Ce_{0.7}Co_{0.2}O_{3-\delta}$ cathode is ascribed primarily to the enhanced electronic conductivity of this material.

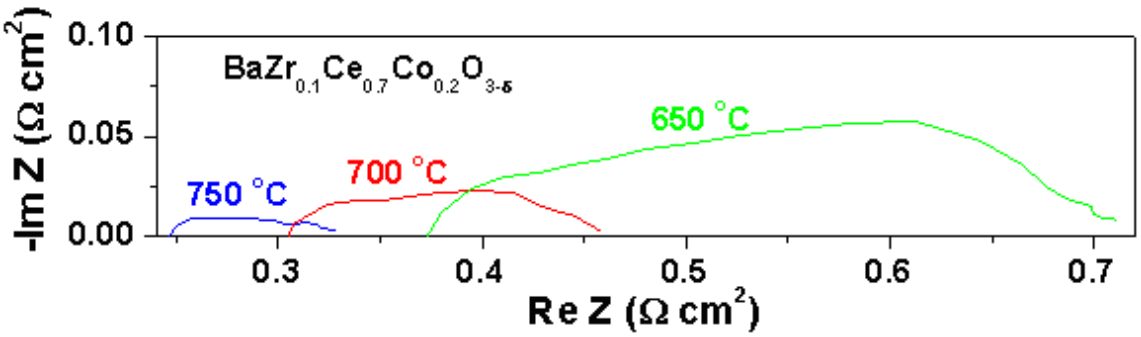

Figure 7-23 Impedance spectra of a single cell with BZCC cathode measured under open circuit conditions at different temperatures.

7.7 Summary

The present study in this chapter demonstrated that a composite cathode with simultaneous transport of proton, oxygen vacancy and electronic defects could effectively extend the electrochemically active sites for oxygen reduction reactions. The cathodic polarization resistance for the composite cathode is greatly reduced relative to that for the traditional oxygen ion-electron conducting cathode.

SOFCs based on oxide proton conductor BZCY electrolyte and BZCY-LSCF composite cathode have produced high and steady power densities at reduced temperatures. The BZCY-LSCF composite cathode demonstrated much-improved catalytic activity toward oxygen reduction than LSCF cathode. Moreover, LSCF is chemically compatible with BZCY even when firing at 1100^{o}C for 10 h, leading to both phase stability and superior adhesion with electrolyte. The preliminary durability testing indicated the practical viability of this promising composite cathode.

Further improvement in power density can be achieved in SOFCs based on oxide proton conductors using properly designed proton-oxygen ion-electron conducting cathode derived from BZCY and SSC. The composite fired at 1000ºC offers unique

transport properties and greatly increase the number of active sites, facilitating the electrochemical reactions involving H^+, O^{2-} and e' or $h^\bullet$ on the entire cathode surfaces.

Cobalt-doped BZCY could be a promising cathode for BZCY-based SOFCs due to the superior compatibility. Based on the XRD analysis and four-probe conductivity measurements, the dissolution of cobalt occurred in the range between 7.5-10 mol% in B-site. The secondary phase $BaCoO_3$ offered high electronic conductivity and effectively accelerated charge transfer reactions. $BaZr_{0.1}Ce_{0.7}Co_{0.2}O_{3-\delta}$ cathode yielded higher power output than other transition metals doped barium cerate. The cell performance can be further enhanced through decrease of the electrolyte thickness and optimization of cathode microstructures.

CHAPTER 8

CONCLUSIONS AND RECOMMENDATIONS

8.1 Conclusions

In this thesis, new electrolyte, anode and cathode materials have been developed, demonstrating much-improved power density of SOFCs at lower temperature as well as remarkable fuel flexibility and poisoning tolerance in sulfur- and carbon-containing fuels without excess of steam and CO_2. The discovery of the electrochemically active and stable electrolytes and electrodes has great potential to dramatically improve the economical competitiveness and commercial viability of intermediate-temperature SOFCs that are driven by cost-effective and renewable fuels.

Fundamental investigations of lattice dynamics, local atomic environment together with anodic and cathodic reactions on surface and interface unravel the mechanisms responsible for improved electrical conductivity, enhanced sulfur and coking tolerance and accelerated oxygen reduction reactions. The profound understanding, in turn, provides a guideline for further development of better electrolyte and electrode materials in terms of practical applications.

In conclusion, this report represents a critical step toward an economically feasible fuel cell for utilization of a wide variety of readily available fuels and demonstrates unique mechanistic investigations of structure-property relationship and surface- and interfaces-involved chemical and electrochemical reactions.

8.2 Recommendations

While encouraging works have been done in development of electrolyte and electrode materials, it may be necessary to conduct the following research activities in the near future with the goal of achieving rational design of fuel-flexible SOFCs operated at lower temperatures.

Direction 1: Defect chemistry: Dopant site selectivity and dopant-dopant-host oxide interaction

$BaZr_xCe_{1-x}O_3$ compounds when doped, typically on the B-site by a lower-valent cation, become oxygen-deficient. However, in the case of large dopant cations, dopant partitioning can occur such that a non-negligible concentration of tri-valent species resides on the B-site that reduces the concentration of oxygen vacancies[110]. This is accompanied by some barium oxide evaporation at high temperatures, resulting in the deviation of the A : B molar ratio in ABO_3 from 1 : 1, which dramatically impacts conductivity, sinterability and chemical stability with respect to reaction with CO2. Thus, it is necessary to investigate the effect of co-doping on dopant site selectivity and dopant-dopant-host oxide interaction. Understanding the defect chemistry could allow conceiving the criteria for dopant selection whether it modifies the local environment, the atomic and electronic structure of the host matrix.

Direction 2: Transference numbers of charge carriers and mixed conduction mechanism

Simultaneous transport of oxygen ions, protons, and free electrons/electron holes has been reported in cerate and zirconate with aliovalent dopants[111]. To have a better understanding on the conduction mechanism, it is essential to separate the contribution of various charge species.

Direction 3: Introduction of sufficient electron conductivity in $BaZr_xCe_{1-x}O_3$ to enhance the electrocatalytic activity

The $BaZr_xCe_{1-x}O_3$ conductor with high electronic conductivity has the potential to be used as the metal-free anodes which could advance the compatibility with the electrolyte and simplify the fuel cell structures. The rapid transport of both protons and oxygen ion vacancies together with the electronic defects may extend the active sites for anode reactions far beyond the traditional triple-phase boundaries, enhance the uptake

and release of water by the surfaces, and facilitate oxidation of H_2S to SO_2 as well as *in situ* reforming of hydrocarbons.

Direction 4: Fundamental understanding of the reactions on composite cathode

While much-improved performance has been demonstrated for composite cathode with porous structure, this design is not suitable to fundamentally understand the cathodic reactions. Geometrically well-defined microelectrodes are recommended in the basic studies. From the statistical averaging over a number of measurements, the rate-determining steps would be determined.

REFERENCES

1. Lewis, N.S. and Nocera, D.G., (2006), "Powering the planet: Chemical challenges in solar energy utilization." *Proceedings of the National Academy of Sciences of the United States of America*, Vol. 103, pp. 15729-15735.
2. Walter, M.G., Warren, E.L., McKone, J.R., Boettcher, S.W., Mi, Q.X., Santori, E.A. and Lewis, N.S., (2010), "Solar Water Splitting Cells." *Chemical Reviews*, Vol. 110, pp. 6446-6473.
3. Herbert, G.M.J., Iniyan, S., Sreevalsan, E. and Rajapandian, S., (2007), "A review of wind energy technologies." *Renewable & Sustainable Energy Reviews*, Vol. 11, pp. 1117-1145.
4. Singhal, S.C., (2000), "Advances in solid oxide fuel cell technology." *Solid State Ionics*, Vol. 135, pp. 305-313.
5. Atkinson, A., Barnett, S., Gorte, R.J., Irvine, J.T.S., McEvoy, A.J., Mogensen, M., Singhal, S.C. and Vohs, J., (2004), "Advanced anodes for high-temperature fuel cells." *Nature Materials*, Vol. 3, pp. 17-27.
6. Goodenough, J.B., (2003), "Oxide-ion electrolytes." *Annual Review of Materials Research*, Vol. 33, pp. 91-128.
7. Fleig, J., (2003), "Solid oxide fuel cell cathodes: Polarization mechanisms and modeling of the electrochemical performance." *Annual Review of Materials Research*, Vol. 33, pp. 361-382.
8. Hibino, T., Hashimoto, A., Inoue, T., Tokuno, J., Yoshida, S. and Sano, M., (2000), "A low-operating-temperature solid oxide fuel cell in hydrocarbon-air mixtures." *Science*, Vol. 288, pp. 2031-2033.
9. Iwahara, H., Esaka, T., Uchida, H. and Maeda, N., (1981), "Proton Conduction in Sintered Oxides and Its Application to Steam Electrolysis for Hydrogen-production." *Solid State Ionics*, Vol. 3-4, pp. 359-363.
10. Kreuer, K.D., (2003), "Proton-conducting oxides." *Annual Review of Materials Research*, Vol. 33, pp. 333-359.
11. Bonanos, N., Ellis, B., Knight, K.S. and Mahmood, M.N., (1989), "Ionic-conductivity of Gadolinium-doped Barium Cerate Perovskite." *Solid State Ionics*, Vol. 35, pp. 179-188.
12. Meulenberg, W.A., Serra, J.M. and Schober, T., (2006), "Preparation of proton conducting BaCe0.8Gd0.2O3 thin films." *Solid State Ionics*, Vol. 177, pp. 2851-2856.
13. Matsumoto, H., Kawasaki, Y., Ito, N., Enoki, M. and Ishihara, T., (2007), "Relation between electrical conductivity and chemical stability of BaCeO3-based proton conductors with different trivalent dopants." *Electrochemical and Solid State Letters*, Vol. 10, pp. B77-B80.
14. Kreuer, K.D., Adams, S., Munch, W., Fuchs, A., Klock, U. and Maier, J., (2001), "Proton conducting alkaline earth zirconates and titanates for high drain electrochemical applications." *Solid State Ionics*, Vol. 145, pp. 295-306.
15. Ryu, K.H. and Haile, S.M., (1999), "Chemical stability and proton conductivity of doped BaCeO3-BaZrO3 solid solutions." *Solid State Ionics*, Vol. 125, pp. 355-367.

16. Zuo, C.D., Zha, S.W., Liu, M.L., Hatano, M. and Uchiyama, M., (2006), "Ba(Zr0.1Ce0.7Y0.2)O3-delta as an electrolyte for low-temperature solid-oxide fuel cells." *Advanced Materials*, Vol. 18, pp. 3318-+.
17. Baertsch, C.D., Jensen, K.F., Hertz, J.L., Tuller, H.L., Vengallatore, S.T., Spearing, S.M. and Schmidt, M.A., (2004), "Fabrication and structural characterization of self-supporting electrolyte membranes for a micro solid-oxide fuel cell." *Journal of Materials Research*, Vol. 19, pp. 2604-2615.
18. Anedda, A., Carbonaro, C.M., Clemente, F., Corpino, R. and Ricci, P.C., (2003), "Raman investigation of surface OH-species in porous silica." *Journal of Physical Chemistry B*, Vol. 107, pp. 13661-13664.
19. Fabbri, E., D'Epifanio, A., Di Bartolomeo, E., Licoccia, S. and Traversa, E., (2008), "Tailoring the chemical stability of Ba(Ce0.8-xZrx)Y0.2O3-delta protonic conductors for Intermediate Temperature Solid Oxide Fuel Cells (IT-SOFCs)." *Solid State Ionics*, Vol. 179, pp. 558-564.
20. Flytzani-Stephanopoulos, M., Sakbodin, M. and Wang, Z., (2006), "Regenerative adsorption and removal of H2S from hot fuel gas streams by rare earth oxides." *Science*, Vol. 312, pp. 1508-1510.
21. Murray, E.P., Tsai, T. and Barnett, S.A., (1999), "A direct-methane fuel cell with a ceria-based anode." *Nature*, Vol. 400, pp. 649-651.
22. Park, S.D., Vohs, J.M. and Gorte, R.J., (2000), "Direct oxidation of hydrocarbons in a solid-oxide fuel cell." *Nature*, Vol. 404, pp. 265-267.
23. Tao, S.W. and Irvine, J.T.S., (2003), "A redox-stable efficient anode for solid-oxide fuel cells." *Nature Materials*, Vol. 2, pp. 320-323.
24. Zhan, Z.L. and Barnett, S.A., (2005), "An octane-fueled olid oxide fuel cell." *Science*, Vol. 308, pp. 844-847.
25. Ruiz-Morales, J.C., Canales-Vazquez, J., Savaniu, C., Marrero-Lopez, D., Zhou, W.Z. and Irvine, J.T.S., (2006), "Disruption of extended defects in solid oxide fuel cell anodes for methane oxidation." *Nature*, Vol. 439, pp. 568-571.
26. Huang, Y.H., Dass, R.I., Xing, Z.L. and Goodenough, J.B., (2006), "Double perovskites as anode materials for solid-oxide fuel cells." *Science*, Vol. 312, pp. 254-257.
27. Chen, F.Z., Zha, S.W., Dong, J. and Liu, M.L., (2004), "Pre-reforming of propane for low-temperature SOFCs." *Solid State Ionics*, Vol. 166, pp. 269-273.
28. Marina, O.A., Canfield, N.L. and Stevenson, J.W., (2002), "Thermal, electrical, and electrocatalytical properties of lanthanum-doped strontium titanate." *Solid State Ionics*, Vol. 149, pp. 21-28.
29. Pillai, M.R., Kim, I., Bierschenk, D.M. and Barnett, S.A., (2008), "Fuel-flexible operation of a solid oxide fuel cell with Sr0.8La0.2TiO3 support." *Journal Of Power Sources*, Vol. 185, pp. 1086-1093.
30. Agarwal, V. and Liu, M.L., (1997), "Electrochemical properties of BaCe0.8Gd0.2O3 electrolyte films deposited on Ni-BaCe0.8Gd0.2O3 substrates." *Journal of the Electrochemical Society*, Vol. 144, pp. 1035-1040.
31. http://availabletechnologies.pnl.gov/media/107_625200731333.pdf, pp.
32. Hibino, T., Hashimoto, A., Suzuki, M. and Sano, M., (2002), "A solid oxide fuel cell using Y-doped BaCeO3 with Pd-loaded FeO anode and Ba0.5Pr0.5CoO3

cathode at low temperatures." *Journal Of The Electrochemical Society*, Vol. 149, pp. A1503-A1508.
33. Xia, C.R., Rauch, W., Chen, F.L. and Liu, M.L., (2002), "Sm0.5Sr0.5CoO3 cathodes for low-temperature SOFCs." *Solid State Ionics*, Vol. 149, pp. 11-19.
34. Taskin, A.A., Lavrov, A.N. and Ando, Y., (2005), "Achieving fast oxygen diffusion in perovskites by cation ordering." *Applied Physics Letters*, Vol. 86, pp.
35. Kim, J.H. and Manthiram, A., (2008), "LnBaCo(2)O(5+delta) oxides as cathodes for intermediate-temperature solid oxide fuel cells." *Journal Of The Electrochemical Society*, Vol. 155, pp. B385-B390.
36. Lin, B., Dong, Y.C., Yan, R.Q., Zhang, S.Q., Hu, M.J., Zhou, Y. and Meng, G.Y., (2009), "In situ screen-printed BaZr0.1Ce0.7Y0.2O3-delta electrolyte-based protonic ceramic membrane fuel cells with layered SmBaCo2O5+chi cathode." *Journal Of Power Sources*, Vol. 186, pp. 446-449.
37. Yang, L., Zuo, C.D., Wang, S.Z., Cheng, Z. and Liu, M.L., (2008), "A novel composite cathode for low-temperature SOFCs based on oxide proton conductors." *Advanced Materials*, Vol. 20, pp. 3280-+.
38. Fabbri, E., Licoccia, S., Traversa, E. and Wachsman, E.D., (2009), "Composite Cathodes for Proton Conducting Electrolytes." *Fuel Cells*, Vol. 9, pp. 128-138.
39. Yang, L., Liu, Z., Wang, S.Z., Choi, Y.M., Zuo, C.D. and Liu, M.L., "A mixed proton, oxygen ion, and electron conducting cathode for SOFCs based on oxide proton conductors." *Journal of Power Sources*, Vol. 195, pp. 471-474.
40. Peng, R.R., Wu, T.Z., Liu, W., Liu, X.Q. and Meng, G.Y., (2010), "Cathode processes and materials for solid oxide fuel cells with proton conductors as electrolytes." *Journal of Materials Chemistry*, Vol. 20, pp. 6218-6225.
41. Vert, V.B., Solís, C. and Serra, J.M., (2010), "Electrochemical Properties of PSFC–BCYb Composites as Cathodes for Proton Conducting Solid Oxide Fuel Cells." *Fuel Cells*, pp. n/a-n/a.
42. Fabbri, E., Oh, T.K., Licoccia, S., Traversa, E. and Wachsman, E.D., (2009), "Mixed Protonic/Electronic Conductor Cathodes for Intermediate Temperature SOFCs Based on Proton Conducting Electrolytes." *Journal Of The Electrochemical Society*, Vol. 156, pp. B38-B45.
43. Tao, Z.T., Bi, L., Yan, L.T., Sun, W.P., Zhu, Z.W., Peng, R.R. and Liu, W., (2009), "A novel single phase cathode material for a proton-conducting SOFC." *Electrochemistry communications*, Vol. 11, pp. 688-690.
44. Mukundan, R., Davies, P.K. and Worrell, W.L., (2001), "Electrochemical characterization of mixed conducting Ba(Ce0.8-yPryGd0.2)O-2.9 cathodes." *Journal Of The Electrochemical Society*, Vol. 148, pp. A82-A86.
45. Matsumoto, H., Shimura, T., Higuchi, O., Tanaka, H., Katahira, K., Otake, T., Kudo, T., Yashiro, K., Kaimai, A., Kawada, T. and Mizusaki, J., (2005), "Protonic-electronic mixed conduction and hydrogen permeation in BaCe0.9-xY0.1RuxO3-alpha." *Journal of the Electrochemical Society*, Vol. 152, pp. A488-A492.
46. Shimura, T., Tanaka, H., Matsumoto, H. and Yogo, T. *Influence of the transition-metal doping on conductivity of a BaCeO3-based protonic conductor*. 2005.

47. Tolchard, J.R. and Grande, T., (2007), "Chemical compatibility of candidate oxide cathodes for BaZrO3 electrolytes." *Solid State Ionics*, Vol. 178, pp. 593-599.
48. Ryu, K.H. and Haile, S.M. *Chemical stability and proton conductivity of doped BaCeO3-BaZrO3 solid solutions*. 1999.
49. Yamazaki, Y., Babilo, P. and Haile, S.M., (2008), "Defect Chemistry of Yttrium-Doped Barium Zirconate: A Thermodynamic Analysis of Water Uptake." *Chemistry of Materials*, Vol. 20, pp. 6352-6357.
50. Katahira, K., Kohchi, Y., Shimura, T. and Iwahara, H., (2000), "Protonic conduction in Zr-substituted BaCeO3." *Solid State Ionics*, Vol. 138, pp. 91-98.
51. Tanner, C.W. and Virkar, A.V., (1996), "Instability of BaCeO3 in H2O-Containing atmospheres." *Journal Of The Electrochemical Society*, Vol. 143, pp. 1386-1389.
52. E Fabbri, D.P., E Traversa, (2010), "Materials challenges toward proton-conducting oxide fuel cells: a critical review." *Chemical Society Reviews*, pp.
53. Giannici, F., Longo, A., Kreuer, K.D., Balerna, A. and Martorana, A., (2010), "Dopants and defects: Local structure and dynamics in barium cerates and zirconates." *Solid State Ionics*, Vol. 181, pp. 122-125.
54. Cheng, Z. and Liu, M.L., (2007), "Characterization of sulfur poisoning of Ni-YSZ anodes for solid oxide fuel cells using in situ Raman micro spectroscopy." *Solid State Ionics*, Vol. 178, pp. 925-935.
55. Choi, Y.M., Compson, C., Lin, M.C. and Liu, M.L., (2006), "A mechanistic study of H2S decomposition on Ni- and Cu-based anode surfaces in a solid oxide fuel cell." *Chemical Physics Letters*, Vol. 421, pp. 179-183.
56. Wang, J.H. and Liu, M.L., (2007), "Computational study of sulfur-nickel interactions: A new S-Ni phase diagram." *Electrochemistry communications*, Vol. 9, pp. 2212-2217.
57. Wang, J.H. and Liu, M.L., (2008), "Surface regeneration of sulfur-poisoned Ni surfaces under SOFC operation conditions predicted by first-principles-based thermodynamic calculations." *Journal Of Power Sources*, Vol. 176, pp. 23-30.
58. Mogensen, M. and Kammer, K., (2003), "Conversion of hydrocarbons in solid oxide fuel cells." *Annual Review of Materials Research*, Vol. 33, pp. 321-331.
59. Crupi, V., Majolino, D., Migliardo, P. and Venuti, V., (2000), "Diffusive relaxations and vibrational properties of water and H-bonded systems in confined state by neutrons and light scattering: State of the art." *Journal of Physical Chemistry A*, Vol. 104, pp. 11000-11012.
60. Ratajska-Gadomska, B. and Gadomski, W., (2004), "Water structure in nanopores of agarose gel by Raman spectroscopy." *Journal of Chemical Physics*, Vol. 121, pp. 12583-12588.
61. Barison, S., Battagliarin, M., Cavallin, T., Daolio, S., Doubova, L., Fabrizio, M., Mortalo, C., Boldrini, S. and Gerbasi, R., (2008), "Barium Non-Stoichiometry Role on the Properties of Ba1+xCe0.65Zr0.20Y0.15O3-delta Proton Conductors for IT-SOFCs." *Fuel Cells*, Vol. 8, pp. 360-368.
62. Lander, J.J., (1951), "The Phase System BaO-NiO." *Journal of the American Chemical Society*, Vol. 73, pp. 2450-2452.

63. Wei, J.M. and Iglesia, E., (2004), "Isotopic and kinetic assessment of the mechanism of reactions of CH4 with CO2 or H2O to form synthesis gas and carbon on nickel catalysts." *Journal Of Catalysis*, Vol. 224, pp. 370-383.
64. York, A.P.E., Xiao, T.C., Green, M.L.H. and Claridge, J.B., (2007), "Methane oxyforming for synthesis gas production." *Catalysis Reviews-Science and Engineering*, Vol. 49, pp. 511-560.
65. Nikolla, E., Holewinski, A., Schwank, J. and Linic, S., (2006), "Controlling carbon surface chemistry by alloying: Carbon tolerant reforming catalyst." *Journal of the American Chemical Society*, Vol. 128, pp. 11354-11355.
66. Pomfret, M.B., Marda, J., Jackson, G.S., Eichhorn, B.W., Dean, A.M. and Walker, R.A., (2008), "Hydrocarbon fuels in solid oxide fuel cells: In situ Raman studies of graphite formation and oxidation." *Journal of Physical Chemistry C*, Vol. 112, pp. 5232-5240.
67. Nikolla, E., Schwank, J. and Linic, S., (2007), "Promotion of the long-term stability of reforming Ni catalysts by surface alloying." *Journal of Catalysis*, Vol. 250, pp. 85-93.
68. Bengaard, H.S., Alstrup, I., Chorkendorff, I., Ullmann, S., Rostrup-Nielsen, J.R. and Norskov, J.K., (1999), "Chemisorption of methane on Ni(100) and Ni(111) surfaces with preadsorbed potassium." *Journal of Catalysis*, Vol. 187, pp. 238-244.
69. Zhan, Z.L. and Barnett, S.A., (2005), "Use of a catalyst layer for propane partial oxidation in solid oxide fuel cells." *Solid State Ionics*, Vol. 176, pp. 871-879.
70. Gur, T.M., Homel, M. and Virkar, A.V., "High performance solid oxide fuel cell operating on dry gasified coal." *Journal Of Power Sources*, Vol. 195, pp. 1085-1090.
71. Ahmed, K. and Foger, K., (2000), "Kinetics of internal steam reforming of methane on Ni/YSZ-based anodes for solid oxide fuel cells." *Catalysis Today*, Vol. 63, pp. 479-487.
72. Jiang, Y. and Virkar, A.V., (2003), "Fuel composition and diluent effect on gas transport and performance of anode-supported SOFCs." *Journal Of The Electrochemical Society*, Vol. 150, pp. A942-A951.
73. Matsuzaki, Y. and Yasuda, I., (2000), "Electrochemical oxidation of H-2 and CO in a H-2-H2O-CO-CO2 system at the interface of a Ni-YSZ cermet electrode and YSZ electrolyte." *Journal Of The Electrochemical Society*, Vol. 147, pp. 1630-1635.
74. Mei, D., (2010), "Density Functional Theory Study of Surface Carbonate Formation on BaO(001)." *J. Phys. Chem. C*, Vol. 114, pp. 1867-1874.
75. Phatak, A.A., Delgass, W.N., Ribeiro, F.H. and Schneider, W.F., (2009), *J. Phys. Chem. C*, Vol. 113, pp. 7269-7276.
76. Lutz, H.D., (1988), "Bonding and structure of water-molecules in solid hydrates-correlation of spectroscopic and structural data." *Structure and Bonding*, Vol. 69, pp. 97-125.
77. Kresse, G. and Furthmüller, J., (1996), "Efficient iterative schemes for ab initio total-energy calculations using a plane-wave basis set." *Phys. Rev. B*, Vol. 54, pp. 11169-11186.

78. Kresse, G. and Hafner, J., (1993), "Ab initio molecular dynamics for liquid metals." *Phys. Rev. B*, Vol. 47, pp. 558-561.
79. Rodriguez, J.A., Ma, S., Liu, P., Hrbek, J., Evans, J. and Perez, M., (2007), "Activity of CeO_x and TiO_x Nanoparticles Grown on Au(111) in the Water-Gas Shift Reaction." *Science*, Vol. 318, pp. 1757-1760.
80. Shishkin, M. and Ziegler, T., (2009), "Oxidation of H_2, CH_4, and CO molecules at the interface between nickel and yttria-stablized zirconia: a theoretical study based on DFT." *J. Phys. Chem. C*, Vol. 113, pp. 21667-21678.
81. K.D. Meinhardt, J.D.V., T.R.Armstrong, L.R. Pederson, *Glass Ceramic Material and Method of Making*, U.S. Patent, Editor. 2002: U.S.
82. Matsuzaki, Y. and Yasuda, I., (2000), "The poisoning effect of sulfur-containing impurity gas on a SOFC anode: Part I. Dependence on temperature, time, and impurity concentration." *Solid State Ionics*, Vol. 132, pp. 261-269.
83. Winkler, J., Hendriksen, P.V., Bonanos, N. and Mogensen, M., (1998), "Geometric requirements of solid electrolyte cells with a reference electrode." *Journal of the Electrochemical Society*, Vol. 145, pp. 1184-1192.
84. Cheng, Z., Zha, S.W. and Liu, M.L., (2007), "Influence of cell voltage and current on sulfur poisoning behavior of solid oxide fuel cells." *Journal Of Power Sources*, Vol. 172, pp. 688-693.
85. Zha, S.W., Cheng, Z. and Liu, M.L., (2007), "Sulfur poisoning and regeneration of Ni-based anodes in solid oxide fuel cells." *Journal Of The Electrochemical Society*, Vol. 154, pp. B201-B206.
86. Lussier, A., Sofie, S., Dvorak, J. and Idzerda, Y.U. *Mechanism for SOFC anode degradation from hydrogen sulfide exposure*. 2008.
87. Sasaki, K., Susuki, K., Iyoshi, A., Uchimura, M., Imamura, N., Kusaba, H., Teraoka, Y., Fuchino, H., Tsujimoto, K., Uchida, Y. and Jingo, N., (2006), "H_2S poisoning of solid oxide fuel cells." *Journal of the Electrochemical Society*, Vol. 153, pp. A2023-A2029.
88. Lohsoontorn, P., Brett, D.J.L. and Brandon, N.P., (2008), "Thermodynamic predictions of the impact of fuel composition on the propensity of sulphur to interact with Ni and ceria-based anodes for solid oxide fuel cells." *Journal of Power Sources*, Vol. 175, pp. 60-67.
89. J. B. Hansen, J.R.-N., *Chapter 65, in Handbook of Fuel Cells - Fundamentals, Technology and Applications.* Advances in Electocatalysis, Materials, Diagnostics and Durability, ed. H.Y. Eds. W. Vielstich, H. A. Gasteiger. Vol. 6. 2009: John Wiley & Sons.
90. Yang, L., Wang, S.Z., Blinn, K., Liu, M.F., Liu, Z., Cheng, Z. and Liu, M.L., (2009), "Enhanced Sulfur and Coking Tolerance of a Mixed Ion Conductor for SOFCs: BaZr0.1Ce0.7Y0.2-xYbxO3-delta." *Science*, Vol. 326, pp. 126-129.
91. Mogensen, M., Jensen, K.V., Jorgensen, M.J. and Primdahl, S. *Progress in understanding SOFC electrodes*. 2002.
92. Xiong, Y.P., Yamaji, K., Horita, T., Yokokawa, H., Akikusa, J., Eto, H. and Inagaki, T., (2009), "Sulfur Poisoning of SOFC Cathodes." *Journal Of The Electrochemical Society*, Vol. 156, pp. B588-B592.
93. Merkle, R. and Maier, J., (2008), "How is oxygen incorporated into oxides? A comprehensive kinetic study of a simple solid-state reaction with SrTiO3 as a

model material." *Angewandte Chemie-International Edition*, Vol. 47, pp. 3874-3894.
94. Choi, Y.M., Mebane, D.S., Lin, M.C. and Liu, M.L., (2007), "Oxygen reduction on LaMnO3-based cathode materials in solid oxide fuel cells." *Chemistry of Materials*, Vol. 19, pp. 1690-1699.
95. Mitterdorfer, A. and Gauckler, L.J., (1998), "La2Zr2O7 formation and oxygen reduction kinetics of the La0.85Sr0.15MnyO3, O-2(g)vertical bar YSZ system." *Solid State Ionics*, Vol. 111, pp. 185-218.
96. Bevilacqua, M., Montini, T., Tavagnacco, C., Fonda, E., Fornasiero, P. and Graziani, M., (2007), "Preparation, characterization, and electrochemical properties of pure and composite LaNi0.6Fe0.4O3-Based cathodes for IT-SOFC." *Chemistry of Materials*, Vol. 19, pp. 5926-5936.
97. Choi, Y., Lin, M.C. and Liu, M.L., (2007), "Computational study on the catalytic mechanism of oxygen reduction on La0.5Sr0.5MnO3 in solid oxide fuel cells." *Angewandte Chemie-International Edition*, Vol. 46, pp. 7214-7219.
98. Phair, J.W. and Badwal, S.P.S., (2006), "Review of proton conductors for hydrogen separation." *Ionics*, Vol. 12, pp. 103-115.
99. Yamanaka, S., Fujikane, M., Hamaguchi, T., Muta, H., Oyama, T., Matsuda, T., Kobayashi, S.I. and Kurosaki, K., (2003), "Thermophysical properties of BaZrO3 and BaCeO3." *Journal of Alloys and Compounds*, Vol. 359, pp. 109-113.
100. Tai, L.W., Nasrallah, M.M., Anderson, H.U., Sparlin, D.M. and Sehlin, S.R., (1995), "Structure And Electrical-Properties Of La1-Xsrxco1-Yfeyo3 .2. The System La1-Xsrxco0.2fe0.8o3." *Solid State Ionics*, Vol. 76, pp. 273-283.
101. Xia, C.R. and Liu, M.L., (2001), "Low-temperature SOFCs based on Gd0.1Ce0.9O1.95 fabricated by dry pressing." *Solid State Ionics*, Vol. 144, pp. 249-255.
102. Murray, E.P., Sever, M.J. and Barnett, S.A., (2002), "Electrochemical performance of (La,Sr)(Co,Fe)O-3-(Ce,Gd)O-3 composite cathodes." *Solid State Ionics*, Vol. 148, pp. 27-34.
103. Baumann, F.S., Fleig, J., Habermeier, H.U. and Maier, J., (2006), "Impedance spectroscopic study on well-defined (La,Sr)(Co,Fe)O3-delta model electrodes." *Solid State Ionics*, Vol. 177, pp. 1071-1081.
104. A.S. Lipilin, I.I.B., L.H. Dubois, A. Sanjurjo, M.C. McKubre, and S. Crouch-Baker, M.D.H. 2006: U.S. .
105. Kilner, J.A. and Brook, R.J., (1982), "A STUDY OF OXYGEN ION CONDUCTIVITY IN DOPED NONSTOICHIOMETRIC OXIDES." *Solid State Ionics*, Vol. 6, pp. 237-252.
106. Shao, Z.P. and Haile, S.M., (2004), "A high-performance cathode for the next generation of solid-oxide fuel cells." *Nature*, Vol. 431, pp. 170-173.
107. Mizusaki, J., Yonemura, Y., Kamata, H., Ohyama, K., Mori, N., Takai, H., Tagawa, H., Dokiya, M., Naraya, K., Sasamoto, T., Inaba, H. and Hashimoto, T., (2000), "Electronic conductivity, Seebeck coefficient, defect and electronic structure of nonstoichiometric La1-xSrxMnO3." *Solid State Ionics*, Vol. 132, pp. 167-180.

108. Wang, S.R., Katsuki, M., Dokiya, M. and Hashimoto, T., (2003), "High temperature properties of La0.6Sr0.4Co0.8Fe0.2O3-delta phase structure and electrical conductivity." *Solid State Ionics*, Vol. 159, pp. 71-78.
109. Ishihara, T., Fukui, S., Nishiguchi, H. and Takita, Y., (2002), "La-doped BaCoO3 as a cathode for intermediate temperature solid oxide fuel cells using a LaGaO3 base electrolyte." *Journal Of The Electrochemical Society*, Vol. 149, pp. A823-A828.
110. Haile, S.M., Staneff, G. and Ryu, K.H., (2001), "Non-stoichiometry, grain boundary transport and chemical stability of proton conducting perovskites." *Journal of Materials Science*, Vol. 36, pp. 1149-1160.
111. Guan, J., Dorris, S.E., Balachandran, U. and Liu, M., (1997), "Transport properties of BaCe0.95Y0.05O3-alpha mixed conductors for hydrogen separation." *Solid State Ionics*, Vol. 100, pp. 45-52.

VITA

Major Awards

1. Gold Medal of MRS Graduate Student Award, Materials Research Society, 2010 Fall
2. Ross Coffin Purdy Award, the American Ceramic Society, 2010
3. National Award for Outstanding Self-Financed Students Abroad, Chinese Government, 2009

Publications

1. **Lei Yang**, et al. Enhanced Sulfur and Coking Tolerance of a Mixed Ion Conductor for SOFCs: $BaZr_{0.1}Ce_{0.7}Y_{0.1}Yb_{0.1}O_{3-\delta}$. **Science**, 2009, 326: 126-129
2. **Lei Yang,** et al. New Insights into Sulfur Poisoning Behavior of Ni-YSZ Anode from Long-Term Operation of Anode-Supported SOFCs. **Energy & Environmental Science**, 2010, 3: 1804
3. **Lei Yang**, et al. A Novel Composite Cathode for Low-temperature SOFCs Based on Oxide Proton Conductors. **Advanced Materials**, 2008, 20: 3280-3283.
4. Matt Lynch*, **Lei Yang*,** W Qin* et al**.** Enhancement of $La_{0.6}Sr_{0.4}Co_{0.2}Fe_{0.8}O_{3-\delta}$ Durability and Surface Electrocatalytic Activity by $La_{0.85}Sr_{0.15}MnO_{3\pm\delta}$ Investigated using a New Test Electrode Platform. **Energy & Environmental Science**, 2011: In press. (Equally contributed)
5. **Lei Yang**, et al. Electrical Conductivity and Electrochemical Performance of Cobalt-doped $BaZr_{0.1}Ce_{0.7}Y_{0.2}O_{3-\delta}$ Cathode. **International Journal of Hydrogen Energy**, 2011, 36: 2266
6. **Lei Yang**, et al. A Mixed Proton, Oxygen Ion and Electron Conducting Cathode for SOFCs Based on Oxide Proton Conductors. **Journal of Power Sources**, 2010, 195: 471-474.

7. **Lei Yang**, et al. High-performance Anode-supported SOFCs Based on $BaZr_{0.1}Ce_{0.7}Y_{0.2}O_{3-\delta}$(BZCY) Fabricated by a Modified Co-pressing Process. **Journal of Power Sources**, 2010, 195: 1845-1848.
8. **Lei Yang,** et al. Mixed Proton-Oxide Ion-Electron Conducting Cathode for SOFCs Based on Oxide Proton Conductors. **Advances in Solid Oxide Fuel Cells V**, Volume 30, Issue 4, 2009 (Editors: N.P. Bansal and P Singh).
9. Changcheng Cheng, Mingfei Liu, **Lei Yang**, et al. Anode-supported tubular SOFCs based on $BaZr_{0.1}Ce_{0.7}Y_{0.1}Yb_{0.1}O_{3-\delta}$ electrolyte fabricated by slip casting method. **Electrochemistry Communications**, 2011: In press.
10. Jae-Wung Lee, Ze Liu, **Lei Yang**, et al. Preparation of dense and uniform $La_{0.6}Sr_{0.4}Co_{0.2}Fe_{0.8}O_{3-\delta}$ (LSCF) films for fundamental studies of SOFC cathodes. **Journal of Power Sources**, 2009, 190: 307-310
11. Changcheng Cheng, Mingfei Liu, **Lei Yang, et al.** Anode-supported micro-tubular SOFCs fabricated by a phase-inversion and dip-coating process. **International Journal of Hydrogen Energy**, 2011: in press
12. Xiaoyuan Lou, Shizhong Wang, Ze Liu, **Lei Yang**, et al. Improving $La_{0.6}Sr_{0.4}Co_{0.2}Fe_{0.8}O_{3-\delta}$ cathode performance by infiltration of a $Sm_{0.5}Sr_{0.5}CoO_{3-\delta}$ coating. **Solid State Ionics**, 2009, 180: 1285-1289.

Patents

1. **Lei Yang**, Meilin Liu. "Sulfur and Coking Resistant Ni-YSZ Anode Modified by Materials with Excellent Water Uptake Ability," U.S. patent, Application filed in 2009, 61/218,584.
2. **Lei Yang**, Meilin Liu. "Dry hydrocarbon Fueled Ni-YSZ Anode with Simple Surface Modification." U.S. patent, Application filed in 2009, 12/609,179.

3. **Lei Yang**, Zhe Cheng, Ze Liu, Meilin Liu. “Novel Anode Materials for SOFCs with High Sulfur and Coking Resistance,” U.S. patent, Application filled in 2008, 61/109,522.